



UvA-DARE (Digital Academic Repository)

Resonant soft x-ray scattering studies of the magnetic nanostructure of stripe domains

Peters, J.F.

Publication date

2003

Document Version

Final published version

[Link to publication](#)

Citation for published version (APA):

Peters, J. F. (2003). *Resonant soft x-ray scattering studies of the magnetic nanostructure of stripe domains*. [, Universiteit van Amsterdam].

General rights

It is not permitted to download or to forward/distribute the text or part of it without the consent of the author(s) and/or copyright holder(s), other than for strictly personal, individual use, unless the work is under an open content license (like Creative Commons).

Disclaimer/Complaints regulations

If you believe that digital publication of certain material infringes any of your rights or (privacy) interests, please let the Library know, stating your reasons. In case of a legitimate complaint, the Library will make the material inaccessible and/or remove it from the website. Please Ask the Library: <https://uba.uva.nl/en/contact>, or a letter to: Library of the University of Amsterdam, Secretariat, Singel 425, 1012 WP Amsterdam, The Netherlands. You will be contacted as soon as possible.

**Resonant soft x-ray scattering
studies of
the magnetic nanostructure
of stripe domains**

Joost Frederik Peters

Resonant soft x-ray scattering studies of the magnetic
nanostructure of stripe domains

Promotiecommissie

Promotor Prof. dr. J.F. van der Veen
Co-promotor Dr. J.B. Goedkoop
Overige leden Dr. E. Brück
Prof. dr. K.H.J. Buschow
Prof. dr. M.S. Golden
Prof. dr. J.C. Lodder
Dr. J. Miltat

Omslag

voorkant: wanordelijke streepdomeinen in een 40 nm GdFe₅ laag zichtbaar gemaakt met magnetische kracht microscopie.

achterkant: magnetische speckle in de eerste orde diffractiepiek van een met coherent licht beschenen 1-dimensionaal streepdomein rooster.

ISBN 905776105X

The work described in this thesis was carried out partly at the European Synchrotron Radiation Facility (Grenoble, France) and at the Van der Waals-Zeeman Instituut of the University of Amsterdam, Valckenierstraat 65, 1018 XE Amsterdam. The work is part of the research program of the Stichting voor Fundamenteel Onderzoek der Materie (FOM) and was made possible by financial support from the Nederlandse Organisatie voor Wetenschappelijk Onderzoek (NWO).

Resonant soft x-ray scattering studies of the magnetic
nanostructure of stripe domains

ACADEMISCH PROEFSCHRIFT

TER VERKRIJGING VAN DE GRAAD VAN DOCTOR
AAN DE UNIVERSITEIT VAN AMSTERDAM
OP GEZAG VAN DE RECTOR MAGNIFICUS
PROF. MR. P.F. VAN DER HEIJDEN
TEN OVERSTAAN VAN EEN DOOR HET COLLEGE VOOR PROMOTIES INGESTELDE
COMMISSIE, IN HET OPENBAAR TE VERDEDIGEN IN DE AULA DER
UNIVERSITEIT
OP DONDERDAG 19 JUNI 2003 TE 10.00 UUR

DOOR

Joost Frederik Peters

geboren te Amsterdam

Promotor Prof. dr. J.F. van der Veen

Co-promotor Dr. J.B. Goedkoop

Faculteit der Natuurwetenschappen, Wiskunde en Informatica

Aan mijn ouders
Aan Marjan

CONTENTS

1	Introduction	7
1.1	Nanomagnetism	7
1.2	X-ray magneto-optics	8
1.3	This thesis	10
2	Stripe domains in magnetic thin films with perpendicular anisotropy	13
2.1	Energetics of a ferromagnet	14
2.2	Domains in $\text{Gd}_{1-x}\text{Fe}_x$ thin films	18
2.3	A continuous 1-dimensional model	21
2.4	Stripe nucleation	23
3	Resonant x-ray magneto-optics	27
3.1	Introduction	27
3.2	Magneto-optic theory	28
3.2.1	Light propagation in a magnetic medium	28
3.2.2	Refractive index: dispersion relations in a magnetic medium	31
3.3	Polarization dependent resonant magnetic scattering	32
3.3.1	Resonant electric dipole scattering	33
3.3.2	Refractive index and forward scattering amplitude	35
3.3.3	Single scattering	36
3.3.4	Polarization space	37
4	Determination of the resonant magneto-optical constants at the Gd $M_{4,5}$ and Fe $L_{2,3}$ edges	41
4.1	Experimental	42
4.2	Absorption and magnetic dichroism cross sections	44
4.3	Kramers-Kronig transformations	47
4.4	Optical constants versus scattered intensity	50

4.5	Conclusions	55
5	Magnetic resonant scattering in the small-angle limit	57
5.1	Introduction	57
5.2	Beamline and setup	58
5.3	Data integration and fitting	59
5.4	Phenomenology of stripe diffraction patterns	62
5.4.1	Linear polarization	62
5.4.2	Circular polarization	63
5.4.3	Non-normal incidence	63
5.5	Interpretation of the stripe diffraction patterns in the small-angle limit	63
5.5.1	The form factor of a single reverse domain	70
5.5.2	Structure factor	72
5.6	Conclusions	73
6	Evolution of stripe domains in in-plane magnetic fields	75
6.1	Macroscopic magnetization loops	75
6.2	Field dependent diffraction data	78
6.2.1	GdFe ₅ , overall behavior	78
6.2.2	GdFe ₅ : evolution of diffraction orders	81
6.2.3	GdFe ₉	84
6.3	Modelling the diffracted intensities	85
6.4	Domain nucleation	88
6.5	Evolution of the domain state	89
6.6	Quantification of domain wall width over the magnetization loop	90
6.7	Determination of the anisotropy and exchange constants from the nucleation field and period	93
6.8	Comparison of the microscopic diffraction data and the macroscopic magnetic properties	95
6.9	Overview of in-plane reversal loop	96
7	Concluding remarks and outlook	101
	List of symbols	105
	References	107

Summary	117
Samenvatting	119
Dankwoord	121

INTRODUCTION

1.1 Nanomagnetism

The introduction of the controlled thin film deposition and lithographic patterning methods originally developed for semiconductor technology has brought about a renaissance in magnetism research. The possibility to engineer multilayers of magnetic and non-magnetic metals on the atomic scale led to the discovery in the late eighties of inter-layer exchange coupling and giant magnetoresistance (GMR). Today, the study of the fascinating static and dynamic magnetic properties of systems with a reduced dimensionality, from two-dimensional multilayers via nanowires to zero-dimensional nanoclusters and molecular magnets, forms an active and exciting area of research in solid state physics.

Confining the dimensions of a magnetic structure to the scale of the magnetic exchange length or the domain wall width results in intriguing phenomena, foreign to bulk materials. For instance a small cluster of Rh, a metal otherwise non-magnetic, becomes magnetic when the cluster becomes smaller than ≈ 700 atoms [1]. Another example is the super-paramagnetic transition observed in small self-assembled Co nanoclusters evaporated on a Au surface [2].

Apart from their scientific interest, the technological potential of magneto-resistive devices and nano-structured materials is an important driving force for the study of magnetic thin films and nanostructures. GMR magnetic field sensors were introduced within 10 years of the discovery of GMR itself and are used for automotive applications and data storage. Tunnel magneto-resistant junctions

form the heart of non-volatile magnetic random access memories (MRAM), a promising technology that is being commercialized at this time.

In this respect it is captivating to see that in this field truly fundamental discoveries foster technological progress and vice versa. The heralded example here is the mesmerizing speed of development in hard-disk technology: after the introduction of thin film GMR sensors *and* granular media in the beginning of the nineties, an annual increase in bit density by 100% has been obtained, beating Moore's law, that describes semiconductor miniaturization by almost a factor two. Today, fundamental limits such as super-paramagnetism are approached, as the bit size goes down to only a few tens of nanometers. This calls for a better fundamental understanding of the static and dynamic properties of confined magnetic systems.

1.2 X-ray magneto-optics

Many methods are used to characterize the magnetism of thin films and confined magnetic structures. Among these, magneto-optical methods are a default tool. They have the advantage that they are not hampered by magnetic and electric fields. With the use of ultra-fast lasers they combine femto-second time resolution, important for studies of the dynamics of magnetization processes, with a spatial resolution in the submicron range. Although the latter is good enough to resolve mesoscopic magnetic structure, the spatial resolution could be improved by going to shorter wavelengths.

Fortunately, the development in synchrotron radiation techniques over the past 15 years has been as breathtaking as the rapid pace in magnetism research. The advent of undulator devices has resulted in high-intensity x-ray beams with complete control of the wavelength and the polarization. The latter development was strongly stimulated by the discovery of large polarization and spin dependent magneto-optical effects at the core level x-ray absorption edges of magnetic elements [3, 4, 5, 6]. It was soon realized that this offered new possibilities for the study of magnetism. Since then, polarization and spin dependent resonant x-ray spectroscopy and scattering have become an indispensable tool for modern magnetism research [7, 8, 9].

Scattering experiments are mostly performed using hard x rays ($\hbar\omega > 2$ keV),

which have the combined advantage of high spatial resolution and large penetration power [10, 11]. However, in the soft x-ray range the resonant magnetic scattering cross-sections are much larger and although the soft x-ray wavelengths are too large for the determination of the unit cell structure, they are perfectly suited to resolve the micromagnetic structure of domains and the artificially structured devices and objects encountered in the field of nanomagnetism.

Resonant soft x-ray microscopy may be the ultimate magneto-optical method for studying *static* nanomagnetic structure [12, 13]. However this tool is still limited in resolution to ≈ 20 to 50 nm due to the difficulty in making large Fresnel zone plate lenses. Soft x-ray scattering is relatively simple to implement and is the method chosen in our studies. A number of pioneering experiments concentrated on reflectivity measurements at the transition metal $L_{2,3}$ edges on single crystal surfaces [14] and magnetic multilayers [15, 16, 17].

The first domain studies were performed by Dürr *et al.*, who measured the in-plane diffracted intensity from periodic stripe domains in FePd thin films [18, 19] in a reflection geometry. Recently Kortright *et al.* applied the element specificity and energy dependence in a transmission small-angle scattering experiment, probing the charge- and the magnetic heterogeneity in granular Co/Pt and CoPtB thin films [20, 21, 22]. For this geometry the description of the magnetic scattering amplitude is simplified considerably. It has been used for soft magnetic speckle experiments [23, 24], and in the study of perpendicular exchange bias multilayers [25].

It is noteworthy to point out that scattering techniques have a great potential to be extended in the time domain. This could be achieved using magnetic pump- optical probe schemes using the time structure of the synchrotron beam [26], similar to dynamical Kerr effect methods using ultra-fast lasers. Another option is to perform dynamic light scattering type experiments [27, 28, 29, 30] to study critical behavior at surfaces or in small particles. Before these steps can be taken, a thorough understanding of the polarization and energy dependence of resonant magnetic scattering in the static regime is essential.

1.3 This thesis

In this thesis we demonstrate how polarization dependent resonant soft x-ray scattering can be used to study the magnetic nanostructure *inside* thin films and surfaces. In particular the nucleation and development of periodic stripe domains in amorphous $\text{Gd}_{1-x}\text{Fe}_x$ thin films are investigated. We find that the evolution of the stripe structure over the in-plane magnetization curve shows an unexpected and amazingly rich behavior: it involves a disorder-order transition at the nucleation field, a strong dependence of the period on field, the creation and growth of a Bloch wall structure and the appearance of closure domains.

In chapter 2 we introduce the theory and phenomenology of magnetic domain formation, emphasizing stripe domains in particular. Chapter 3 deals with the macroscopic theory of magneto-optics and gives the dispersion relations that connect the absorption and dichroism to the dispersion and birefringence of a magnetic medium. The macroscopic theory is followed by a microscopic description in terms of the resonant atomic scattering amplitude for an electric dipole transition.

In chapter 4 a quantitative determination of magneto-optic atomic scattering factors around the Gd $M_{4,5}$ and Fe $L_{2,3}$ edge resonances is presented. These are obtained from the polarization and spin dependent x-ray transmission of homogeneously magnetized thin $\text{Gd}_{1-x}\text{Fe}_x$ films. The obtained optical constants are shown to be in perfect agreement with the total scattering cross section from a stripe domain lattice in a GdFe_5 thin film.

The phenomenology of the polarization, energy and geometry dependence of resonant diffraction from this periodic stripe lattice is investigated in chapter 5. We demonstrate that at the Gd $M_{4,5}$ edge the energy- and polarization dependence of the resonant scattering cross section can be used to separate the scattering contributions from the bulk domains, domain walls and closure domains. By comparing the scattered intensity with that for a micromagnetic model we obtain the three-dimensional structure of the stripe lattice.

Finally chapter 6 gives a detailed description of the evolution of the stripe lattice over the in-plane magnetization curve in GdFe_5 and GdFe_9 thin films. Although

the general behavior of the stripe period and scattered intensity as a function of the applied field is very similar for the two samples there are also apparent differences. These can be explained perfectly in terms of their macroscopic magnetic properties, which we extract from the nucleation field and stripe period.

2

STRIPE DOMAINS IN MAGNETIC THIN FILMS WITH PERPENDICULAR ANISOTROPY

Magnetic materials and their properties have fascinated mankind ever since their first discovery, and remain a rich and complex field of physics. The household example of a needle being attracted by the tip of a pair of scissors has an origin in quantum mechanical exchange interactions, but its strength depends also on the elemental composition and the crystalline microstructure of the material, and finally on the macroscopic shape of the needle and scissors alike.

In this chapter we will outline these different factors in order to describe the magnetism displayed by the magnetic thin films that are the subject of most of the studies in this thesis. We will illustrate the influence of the anisotropy, thickness and magnetic history on the domain state for amorphous $\text{Gd}_{1-x}\text{Fe}_x$ thin films. We then introduce a continuous 1-dimensional model that describes the behavior of 'weak-stripe' domains in applied in-plane fields along the stripe direction. In the last section the problem of stripe nucleation is discussed. The phenomenology and theory of magnetic domains presented here is meant to provide a basis for the analysis of the magnetic diffraction data. For a recent and comprehensive source of information on the study of magnetic domains we refer to the book by Hubert and Schäfer [31], and the references therein.

2.1 Energetics of a ferromagnet

When atoms join up in a solid, the atomic orbitals overlap to form bonds. Exchange interactions between neighboring atoms tend to align the spins of their valence electrons either parallel or anti-parallel. If strong enough, this interaction can overcome thermal agitation, giving rise to (anti)-ferromagnetic order where all neighboring spins are (anti-)parallel [31, 32, 33]. The *exchange energy density* involved is written as $A(\mathbf{grad} \mathbf{m})^2$, where A is the exchange stiffness constant and \mathbf{m} is the local unit magnetization vector [34].

A second effect of the bonding process is that the spherical symmetry of the atom is broken. The orbital motion of the electrons around the atom adapts itself to this configuration, aligning the corresponding orbital magnetic moment to some lattice directions. The spin-orbit interaction then also orients the electron spins in certain, called *easy*, directions, that have a lower energy than other, *hard*, directions. For systems with uniaxial crystal symmetry, the corresponding *anisotropy energy density* involved in rotating the moment away from the easy z -axis can be written as $K_u(1 - m_z^2)$, where K_u is the uniaxial anisotropy constant.

The exchange and anisotropy energies alone would lead to a uniform magnetization throughout the object, with all atomic moments aligned along the easy direction. A finite object however would set up a large stray field in its surroundings originating from the magnetic free poles at its surfaces. The corresponding *magneto-static dipolar energy* or *shape anisotropy energy* can be obtained by integrating the magnetic energy inside the object, or $E_s = -\int_V dV \frac{1}{2} \mu_0 \mathbf{H}_d \cdot \mathbf{M}$, where \mathbf{H}_d is the demagnetizing field, \mathbf{M} the magnetization vector and μ_0 the vacuum magnetic permeability.

Finally, an applied field \mathbf{H} , acting on the magnetization, gives an energy density $-\mu_0 \mathbf{H} \cdot \mathbf{M}$. The total energy of an uniaxial ferromagnet now can be written as [31, 35]

$$E_{tot} = \int_V [A(\mathbf{grad} \mathbf{m})^2 + K_u(1 - m_z^2) - \mu_0 \mathbf{H} \cdot \mathbf{M} - \frac{1}{2} \mu_0 \mathbf{H}_d \cdot \mathbf{M}] dV. \quad (2.1)$$

Note that we have neglected the internal and external magneto-elastic energies that are negligible in the systems studied here.

The magnetic configuration in the object is given by the local magnetic energy minimum that the system can reach. For instance, the magnetization may break up in two or more domains of different (opposite) directions in order to reduce the stray field energy [35]. The formation of domains also creates domain walls where the magnetization rotates from one direction to the other at the expense of the exchange- and anisotropy energies. For the most general case, a 180° Bloch wall, it is easy to show that the specific surface energy of the wall is $\gamma = \sqrt{AK_u}$ and that it is characterized by a width $\delta_b = \pi\sqrt{A/K_u}$ [31, 36], which is of the order of a few nm for hard (high K_u) materials and up to 50 nm or more for soft magnetic materials.

The detailed microscopic magnetic structure can be found by solving $\mathbf{m}(\mathbf{r})$ from the complete set of micromagnetic equations that follow from (2.1) [31, 37]. These expressions cannot be solved analytically and require elaborate numerical methods. However, simplified quasi 2-dimensional models can be solved analytically, as will be discussed in section 2.3.

It should always be remembered that in any real material micro- to nanometric defects that disrupt the exchange interactions will tend to pin the magnetic domains and domain walls. This pinning leads to magnetic hysteresis: the domain distribution and hence the total magnetization depends on the magnetic history, such as direction of the applied magnetic field and its sweep rate. The analytical or computational micromagnetic methods therefore only work in sufficiently homogeneous static systems.

We will now focus on the simple geometries presented by thin films. A uniform magnetization perpendicular to the film plane would cost a shape anisotropy energy penalty proportional to the square of the magnetization $K_s = \frac{1}{2}\mu_0 M^2$. The necessity to avoid large free poles therefore tends to orient the magnetization in the film plane, as indicated in Fig. 2.1-A. However, thin film deposition techniques make it possible to grow films that have a perpendicular uniaxial anisotropy K_u where the easy axis is along the sample normal, favoring an out-of-plane magnetization as shown in Fig. 2.1-B.

Kittel [38] showed that the competition between these two anisotropies can lead to a configuration with alternating up- and down, or *stripe* domains, Fig. 2.1-C. Such an arrangement reduces the stray field of the film while most of the layer

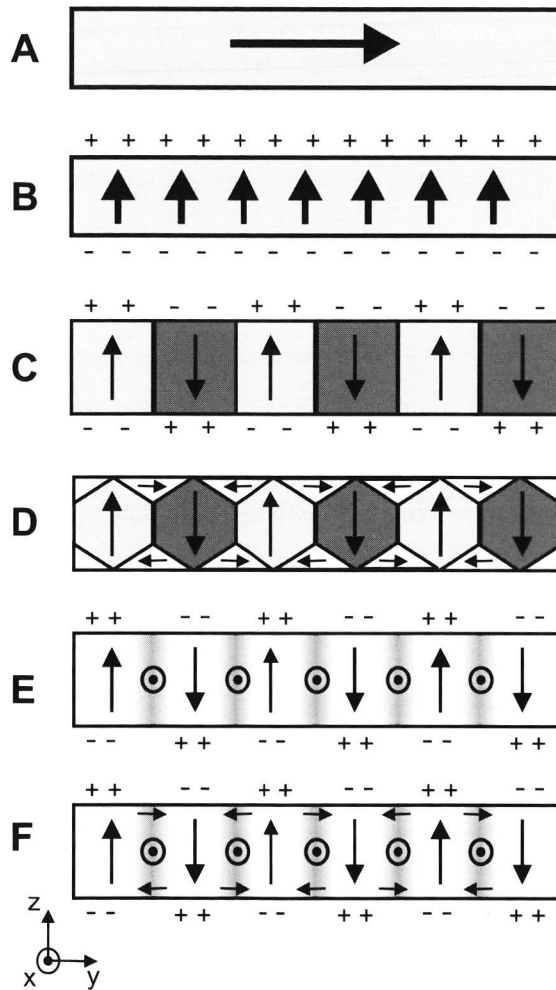


Figure 2.1: Domain states in a magnetic thin film, (A) uniform in-plane (B) uniform out-of-plane, (C) alternating up and down, (D) flux closed state with closure, the internal lines denote domain walls. (E) and (F) represent a continuously varying magnetization without (E) and with closure (F), grey indicates regions with in-plane magnetization.

is perpendicularly magnetized. Kittel realized that such an open structure still has free magnetic poles, which can be avoided by the creation of surface *closure domains*, as drawn in Fig. 2.1-D, but at the cost of anisotropy energy. Fig. 2.1-E and -F show slightly more realistic models that take into account the finite width of the domain walls.

The most important parameter determining the state of magnetic thin films is therefore the ratio between the magneto-crystalline anisotropy and the magneto-static energy or quality factor $Q = K_u/K_s$. For $Q < 1$ and in the absence of an external field, a uniform in-plane magnetization can exist only for films that are thinner than a critical thickness D_{cr} [31, 38]. As we discuss below, in all other cases an out-of-plane domain state is favored and regular stripe patterns may be formed when the dipolar energy becomes strong enough.

Stripes and bubbles have been studied in detail in the 60's and 70's in garnet and ferrite films because of their potential for data storage [39]. The default tool was Kerr microscopy, since it allows direct observation of stripes in high applied fields [40]. With the advent of magnetic force microscopy (MFM) domains in magnetic thin films can be studied routinely with 40 nm resolution [41, 42]. Even better resolution has recently been achieved by spin polarized scanning tunnel microscopy (SP-STM)[43, 44], scanning electron microscopy with polarization analysis (SEMPA) [45] and photo emission electron microscopy (PEEM)[46, 13], which allow the direct observation of domain walls. These techniques measure either the stray field of the domains (MFM) or the magnetization of the surface atoms. The magnetization profile of the film integrated over its thickness can be obtained from transmission electron Lorentz microscopy [47, 48] but none of these techniques can resolve the 3-D domain structures inside the film. Also the application of magnetic fields is difficult.

New x-ray techniques such as resonant scattering and microscopy are interesting for domain studies since they are, like Kerr microscopy, photon-in photon-out techniques, not influenced by the applied field. The resolution, in principle, is only limited by the wavelength of the light, 1 Å for hard x rays and 1 nm for soft x rays. In parallel with this thesis work, Fischer *et al.* have shown that soft x-ray transmission microscopy combined with resonant dichroism and birefringence effects can be used to image the bulk domain structure in thin films with a resolution of 25 nm [12, 13] in applied magnetics fields. x-ray scattering, in-

roduced recently, adds depth sensitivity in the reflection geometry [18] and the possibility to separate the three components of the magnetization, as will be discussed in Chapter 5.

2.2 Domains in $\text{Gd}_{1-x}\text{Fe}_x$ thin films

In amorphous $\text{Gd}_{1-x}\text{Fe}_x$ thin films the Fe and Gd magnetic sublattices align anti-parallel [49, 50], causing the net magnetic moment M to vary strongly with x . They show a growth-induced out-of-plane magneto-crystalline anisotropy K_u [50, 51, 52], the origin of which has been linked to the microstructure of the material [53], and to preferential ordering during deposition [54, 55], probably induced by a magnetic surface anisotropy. The resulting anisotropy depends on growth parameters such as the temperature, pressure and the deposition method.

The anisotropy and magnetization are the two parameters that determine the quality factor Q and it is their tunability that make these systems an excellent model system for domain studies. In fact, at a particular composition the Gd and Fe sublattice magnetization cancel each other. For our MBE-grown samples this compensation composition is $x_c = 0.76$ at room temperature. Here the demagnetizing energy vanishes and Q has a singularity. We have grown a large number of $\text{Gd}_{1-x}\text{Fe}_x$ samples with $0 < x < 1$ and different thicknesses ranging from 20 nm to 1 μm . The films were prepared by electron beam co-evaporation at room temperature and a pressure of $< 5 \times 10^{-9}$ mbar on Si and Si_3N_4 substrates. The Gd and Fe deposition rates were monitored by quartz balances and the composition and thickness were regularly checked for consistency by Rutherford Back Scattering (RBS). This showed the composition to be correct within 0.5% and the thickness within 5%. From x-ray diffraction we found that the samples were indeed amorphous. AFM measurements showed that the films were flat within 1 nm.

Fig. 2.2 shows examples of the magnetic domain structure as obtained by Magnetic Force Microscopy. The top panels show, from left to right, out-of-plane domains observed in 40 nm GdFe_3 , GdFe_4 and GdFe_5 thin films. The domain size is seen to change dramatically with composition from almost macroscopic on the left to a truly nanoscopic disordered stripe state on the right.

The explanation can be found in the changes in the reduced anisotropy Q as a function of the composition. The GdFe_3 composition ($x = 0.75$) is very close to the compensation composition $x_c = 0.76$ and therefore has a very small magnetization. The domain wall energy will be large compared to the magneto-static term in equation (2.1), hence large domains are favored. On increasing x beyond x_c , Q decreases and the domain size reduces accordingly, as is observed for the GdFe_4 and GdFe_5 samples.

In the absence of closure domains it can be shown that the magneto-static energy is proportional to the reduced domain width $w = W/D$, the ratio between the width of the domains W and the thickness of the film D . Smaller reduced widths w decrease the magnetostatic energy but increase the domain wall density and hence the total domain wall energy. Neglecting the interaction between the free-poles on both sides of the film, Kittel predicted that the optimum stripe width is proportional to the square root of the thickness $W \propto \sqrt{D}$ [38]. This is illustrated in Fig. 2.2, middle row, which shows the domain configuration in GdFe_2 thin films of 33 nm, 65 nm and 1 μm . The corresponding domain periods of 140 nm, 210 nm and 810 nm follow the prediction reasonably well.

On the bottom left, a typical labyrinth stripe pattern in a 40 nm GdFe_5 thin film is observed after out-of-plane demagnetization. In-plane demagnetization results in a parallel stripe lattice (middle) that is 'aligned' with the field direction. In this case the average width of the stripes is reduced by $\sim 20\%$. This larger stripe density indicates that the aligned system has a lower energy. Apparently, the disordered state has a local energy minimum and the lower energy ordered state could only be reached via a magnetization process.

To round off this phenomenology of typical domain morphologies, we show the bubble domain structure of a 40 nm $\text{Tb}_{2.5}\text{Gd}_{12.5}\text{Fe}_{85}$ thin film after in-plane demagnetization. The magnetization and thickness are similar to the GdFe_5 film, however the much larger anisotropy due to Tb causes a completely different domain pattern. Remarkably, the as-grown film has a domain structure similar to the disordered labyrinth pattern in the GdFe_5 film.

The abundant variety of domain morphologies at remanence raises the question how the domains evolve in applied fields. In-plane fields will tend to

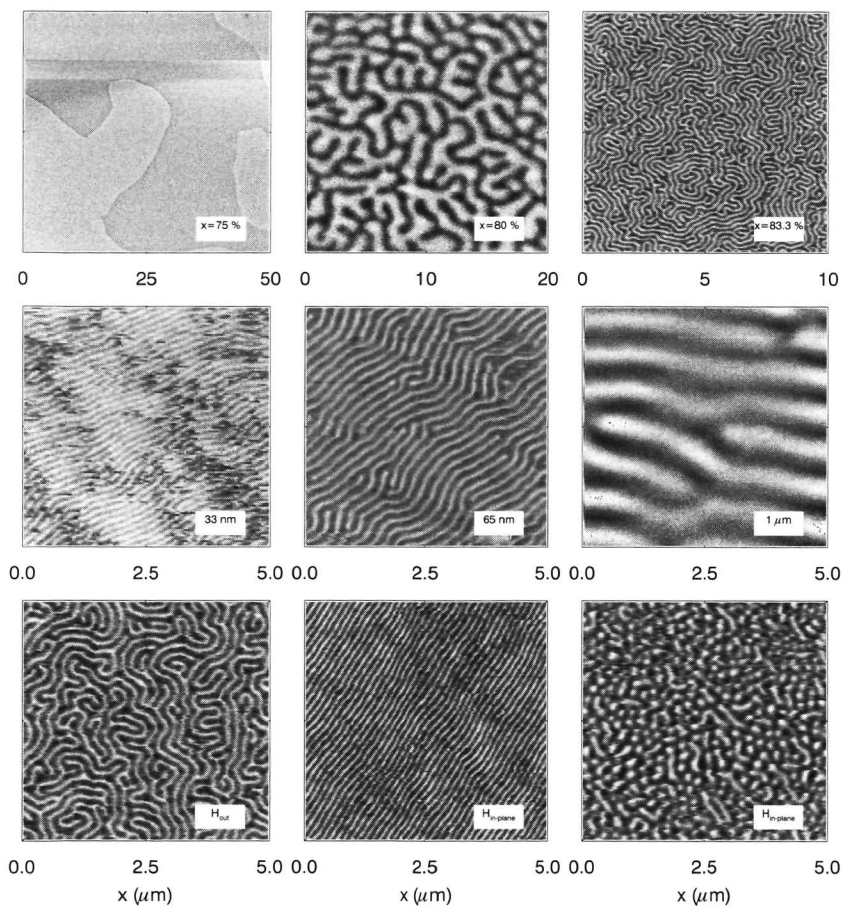


Figure 2.2: MFM images of magnetic domains in $\text{Gd}_{1-x}\text{Fe}_x$ thin films. Top panels: Composition dependence, for as-grown samples. Middle panels: Thickness dependence for GdFe_2 films. Bottom panels: stripes in an out-of-plane (left) and in-plane (middle) demagnetized GdFe_5 film of 40 nm , on the right magnetic bubble state in an in-plane demagnetized TbGdFe thin film.

align all moments in the film plane, and can be thought of as enhancing the shape anisotropy [31]. Perpendicular fields will favor the 'up' domains over the 'down' domains or *vice versa*. In both cases, the stripe structure will adapt itself by rearranging domain walls. Even perfect films will show hysteresis due to topological effects in the correlated lattices [56]. The macroscopic magnetic behavior of the films in applied fields was characterized with magneto-optical Kerr effect magnetometry (MOKE). Fig. 2.3 shows a typical example of the in-plane and out-of-plane magnetic hysteresis in a GdFe₅ thin film that has out-of-plane stripe domains at remanence, as shown in Fig. 2.2.

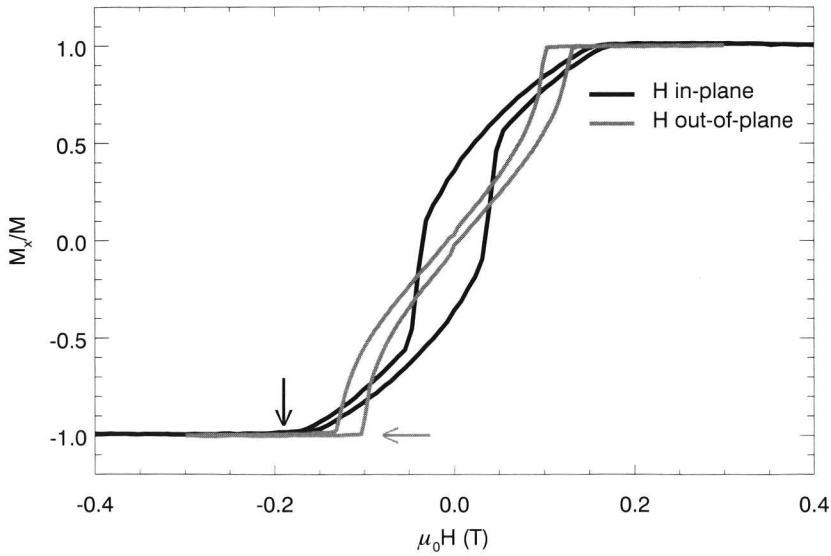


Figure 2.3: Room temperature MOKE magnetization curves for a 40 nm GdFe₅ thin film with fields applied in the film plane or normal to it. The arrows indicate the domain nucleation fields.

2.3 A continuous 1-dimensional model

The first systematic study of the evolution of stripe domains during an out-of-plane magnetization loop was performed by Kooy and Enz using Faraday

microscopy [40]. They developed a theory, which calculates the dipolar energy for the stripe structure in terms of a 1-D square magnetization profile [40]. Although this model assumes a zero domain wall width, it predicted the shape of the out-of-plane magnetization loop (Fig. 2.3) and the behavior of the stripe lattice remarkably well. Other authors extended the analysis to the case of bubble domains [57] or developed similar analytical models for in-plane applied fields [58]. A 2-D model including surface domains was presented by Hubert [59], applicable to out-of-plane as well as in-plane applied fields.

Marty *et al.* [60], combining ideas of Kaczer [61], Sukstanskii [62], and Druyvesteyn [58], developed a model for in-plane applied fields that includes finite domain wall widths, as schematically drawn in Fig. 2.1-E. As this model is relevant to the measurements discussed in Chapter 6, we discuss this model in some more detail. The stripes are assumed to be perfectly parallel to the applied field $\mathbf{H} // \hat{x}$ and the magnetization is assumed to stay in the xz -plane and vary only along the y -direction. The advantage of this model is that the demagnetizing energy can still be expressed analytically, but it clearly excludes the formation of closure regions towards the surface, as indicated in Fig. 2.1-F.

The $m_z(y)$ magnetization is assumed to be given by a trial function $s(y)$. Marty *et al.* use the Jacobi sine function [63], originally proposed by Kaczer [61, 62, 60]. This function is described by two independent parameters, the stripe width w and a shape parameter σ that determines the domain wall width and profile. Examples of the Jacobi sine function for different σ are given in Fig. 2.4. For $0.8 < \sigma < 1$ this function closely resembles a bulk Bloch wall profile [31], which is shown for comparison in Fig. 2.4.

Besides w and σ , the maximum amplitude of the out-of-plane magnetization is treated as a separate variable

$$m_z(y) = \sin(\theta_0)s(y), \quad (2.2)$$

where θ_0 is the maximum 'canting angle' of the magnetization with respect to the film plane. It is assumed that the magnetization is continuous and of constant amplitude for all y . Since $m_y = 0$ in this model it follows that $m_x(y)^2 = 1 - m_z(y)^2$. The optimum $\mathbf{m}(y)$ is found by minimizing the total energy as given in eq. (2.1) with respect to θ_0 , δ and w and for a given in-plane applied field, anisotropy and thickness of the film.

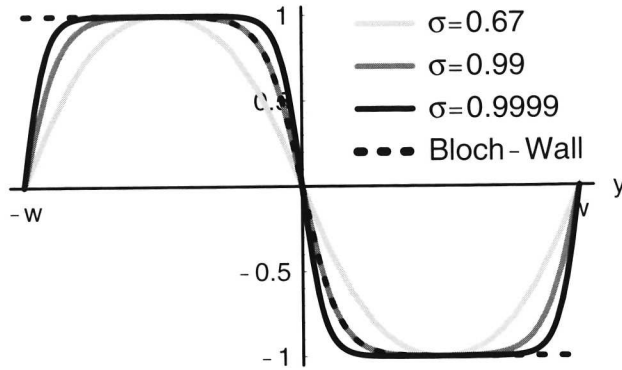


Figure 2.4: Examples of the Jacobi sine function (SN) for different values of the shape parameter σ . The width W and σ are defined here by $s(y) = \text{SN}(\frac{2K(\sigma)}{w}, \sigma)$, where K is the elliptic integral of the first kind. Dashed line: Bloch wall for a wall width $\delta/W = 0.2$.

Fig. 2.5 represents the phase diagram in the (Q, t) plane at zero field [60], where t is the dimensionless reduced thickness defined as $t = \frac{D}{\sqrt{(A/K_s)}}$, with D the film thickness and A the exchange stiffness constant. Lines of constant stripe width w and canting angle θ_0 are drawn. To the left of the *critical line* $\theta_0 = 0$ the film is single domain. Above the critical line domains exist with a canting angle that steeply increases with Q and t .

As mentioned above, the model does not take into account the development of a magnetic closure component towards the surface. Micromagnetic calculations [64] as well as soft x-ray magnetic scattering experiments [18] have shown that a closure component does exist. Qualitatively, the model can be extended to include closure by allowing the in-plane magnetic component of the domain wall to twist in the y -direction, as sketched in Fig. 2.1-F. The validity of this approach will be discussed in more detail later.

2.4 Stripe nucleation

Stripe nucleation, either close to the critical thickness or in the presence of applied fields, has been theoretically investigated by several authors [31, 40, 65]. In the case of out-of-plane applied fields [40], nucleation of reverse domains is a first order process, accompanied by a sharp break in the magnetization, as

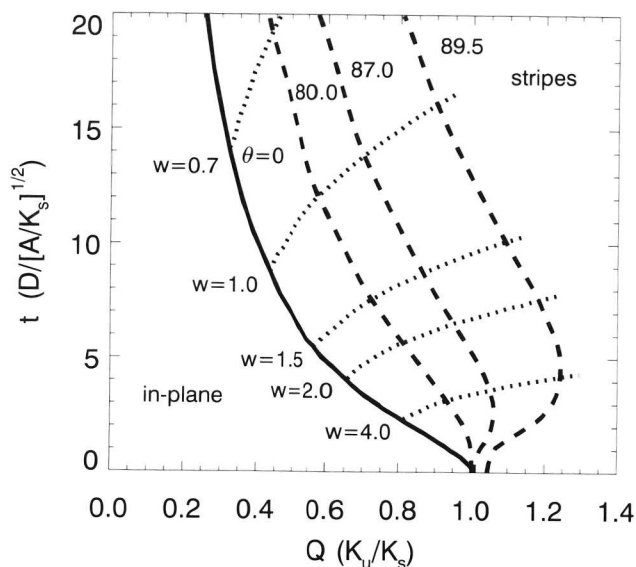


Figure 2.5: Phase diagram in the Q - t plane. Shown are lines of constant canting angle θ_0 and lines of constant reduced width w . The solid line marks the transition from stripes to uniform magnetization. Taken from ref. [60].

can be seen in Fig. 2.3. For in-plane fields the transition is second order like, involving a gradual increase of the canting angle and the nucleation point is hard to distinguish. In the latter case, the full micromagnetic equations can be linearized and a rigorous analytical solution exists [31, 65]. The complete mathematical treatment is discussed in [31], here we mention the salient points of the analysis.

Above saturation all moments are forced to align parallel to the field. At the nucleation field H_{cr} a small out-of-plane undulation of the magnetization appears but the in-plane component m_x along the stripe direction can still be taken as constant. From the calculations it is found that m_y and m_z follow a sinusoidal profile along y :

$$m_z = A(z) \cos(\mu y) \quad (2.3)$$

$$m_y = B(z) \sin(\mu y), \quad (2.4)$$

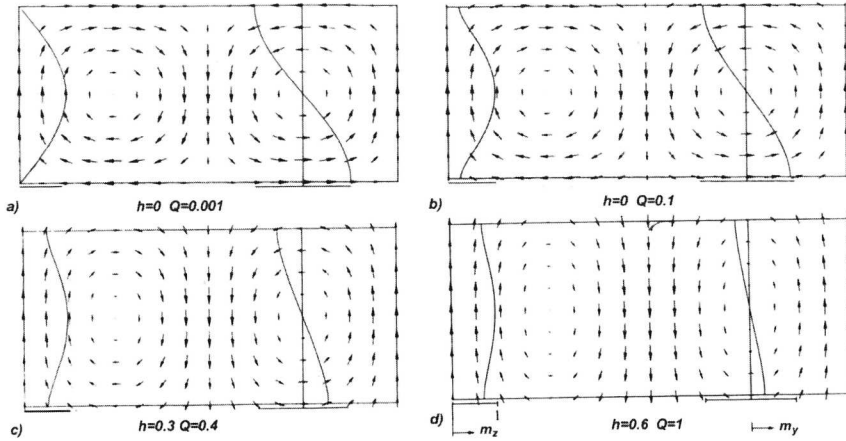


Figure 2.6: Calculated 2-D magnetization profiles at nucleation for different reduced applied fields h and Q . The solid curves indicate the amplitudes of m_y and m_z normalized to the maximum of the vertical component m_z . Taken from ref. [31].

where μ is the wave number. Examples of the internal magnetic structure for different values of Q and reduced applied field $h = \frac{\mu_0 H M_s}{K_u}$ at the corresponding critical thickness are given in Fig. 2.6. For low anisotropy ($Q \ll 1$) a fully flux closed structure is found. For intermediate anisotropy $Q \approx 1$ an open pattern is obtained that becomes almost 1-dimensional for $Q = 1$. The solid lines that are drawn from top to bottom in these figures indicate the amplitudes $A(z)$ and $B(z)$, normalized to the maximum of $A(z)$. These lines show that the out-of-plane component has maximum amplitude in the center of the film whilst the closure component is maximum at the surfaces.

In Chapter 6 we present measurements of the *critical* values of field H_{cr} , period P_{cr} and thickness D_{cr} at stripe nucleation for different samples. The rigorous nucleation theory [31] relates these parameters to the anisotropy factor Q and exchange stiffness A . For later reference we show in Fig. 2.7 the reduced critical thickness $d_{cr} = \frac{D_{cr}}{2\pi\sqrt{A/K_u}}$ and the reduced inverse width $1/w_{cr}$ as a function of the anisotropy Q for different in-plane reduced fields h . For comparison we have also drawn the critical line for $h = 0$ as found by Marty, and shown in Fig. 2.5. It resembles the rigorous result reasonably well for values of $Q > 0.7$. In combination with the magnetization profiles in Fig. 2.6 this suggests that for

values of $Q \approx 1$, as valid for the samples studied in this thesis, a 1-D continuous description of the stripe domains is appropriate.

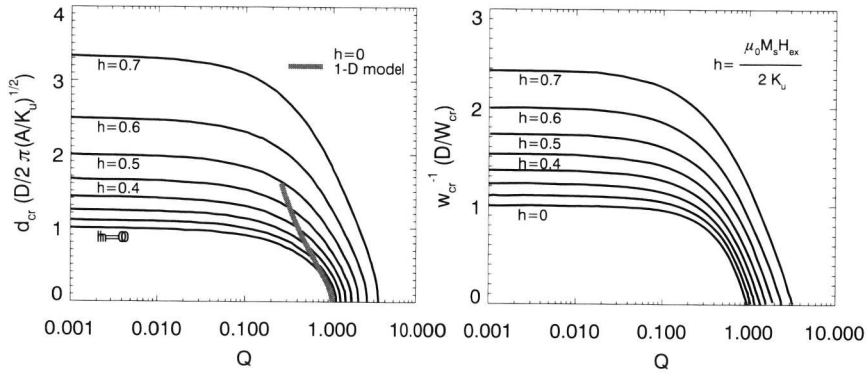


Figure 2.7: The critical thickness d_{cr} for stripe formation (left) and the corresponding inverse critical stripe width w_{cr}^{-1} (right) as a function of Q for different applied in-plane fields h along the stripe direction. Bold line: critical line at zero field for the continuous 1-D model of Marty. Adapted from ref. [31]

RESONANT X-RAY MAGNETO-OPTICS

3.1 Introduction

Light propagating through a medium scatters when the refractive index of that medium is modulated on a length scale comparable with the wavelength of the light. In this thesis we describe resonant x-ray magnetic scattering experiments, where the atomic susceptibility and hence the refractive index depends strongly on the direction of the magnetization. We first review the classical, macroscopic, description of light propagation in a magnetized medium, obtained from the solutions of Maxwell's equations. We discuss solutions in terms of the refractive index for propagation parallel and perpendicular to the magnetic field. The connection between the macroscopic refractive index and the microscopic atomic scattering amplitude follows from the optical theorem. The resonant contribution to the atomic scattering amplitude is worked out for electric dipole transitions and we give a description of the far-field scattered intensity in terms of the single scattering approximation.

3.2 Magneto-optic theory

3.2.1 Light propagation in a magnetic medium

In this section we will derive the wave equation of light in a uniform magnetized medium. We base ourselves on Jackson [66], Landau and Lifshitz [67] and in particular D.Y. Smith [68, 69, 70], where more details can be found. The magnetization of the medium implies an anisotropy in the electron spins and orbits. As a result the linear response of the medium to an incident electromagnetic wave is anisotropic. In the dipolar approximation the constitutive relations that describe this response are

$$\mathbf{D} = \epsilon_0 \mathbf{E} + \mathbf{P} \quad (3.1)$$

$$\mathbf{B} = \mu_0 (\mathbf{H} + \mathbf{M}), \quad (3.2)$$

with \mathbf{E} and \mathbf{D} the electric- field and displacement and \mathbf{H} and \mathbf{B} the magnetic field and induction. ϵ_0 and μ_0 are the electric permittivity and magnetic permeability in vacuum. \mathbf{P} is the polarization of the medium due to the incident field \mathbf{E} . For the response to the varying magnetic field of the propagating wave we will assume that at optical or higher frequencies the magnetic permeability $\mu(\omega) = \mu_0$, but we do not exclude a static magnetization \mathbf{M} of the medium, hence $\partial \mathbf{B} / \partial t = \mu_0 \partial \mathbf{H} / \partial t$.

For rapidly varying fields, the polarization vector $\mathbf{P}(t)$ at time t not only depends on $\mathbf{E}(t)$ but on \mathbf{E} at all earlier times

$$\mathbf{P}(t) = \int_0^\infty \epsilon_0 \mathbf{h}(\tau) \mathbf{E}(t - \tau) d\tau, \quad (3.3)$$

where $\mathbf{h}(\tau)$ is the response function. Expanding $\mathbf{P}(t)$ as a Fourier integral and applying the convolution theorem to the Fourier transforms $\chi(\omega)$ of $\mathbf{h}(t)$ and $\mathbf{E}(\omega)$ of $\mathbf{E}(t)$ we obtain

$$\mathbf{P}(t) = \int_{-\infty}^\infty \mathbf{P}(\omega) e^{-i\omega t} d\omega = \int_{-\infty}^\infty \epsilon_0 \chi(\omega) \mathbf{E}(\omega) e^{-i\omega t} d\omega, \quad (3.4)$$

where χ is the susceptibility tensor describing the material properties. Similarly

$$\mathbf{D}(t) = \int_{-\infty}^\infty \mathbf{D}(\omega) e^{-i\omega t} d\omega = \int_{-\infty}^\infty \epsilon_0 [1 + \chi(\omega)] \mathbf{E}(\omega) e^{-i\omega t} d\omega \quad (3.5)$$

and we find a linear relation for the Fourier transforms $\mathbf{E}(\omega)$ and $\mathbf{D}(\omega)$

$$\mathbf{D}(\omega) = \epsilon_0 (1 + \chi) \cdot \mathbf{E}(\omega). \quad (3.6)$$

For a plane electromagnetic wave of energy $\hbar\omega$ in an absorbing medium the spatial and temporal dependence are given by the propagation factor $e^{i(\omega t + \mathbf{k}\cdot\mathbf{r})}$, where the complex wavevector $\mathbf{k} = \mathbf{k}_1 + i\mathbf{k}_2$. The real part \mathbf{k}_1 is a vector parallel to the propagation direction of the wave, describing its phase, whereas the imaginary part \mathbf{k}_2 is a vector normal to the planes of equal intensity describing the absorption of the propagating wave. For a *homogeneous* wave $\hat{\mathbf{k}}_1 = \hat{\mathbf{k}}_2$, otherwise $\hat{\mathbf{k}}_1 \neq \hat{\mathbf{k}}_2$, a situation encountered when the wave is obliquely incident on a surface.

Substituting equation (3.6) into the Maxwell equations,

$$\nabla \times \mathbf{E} = -\frac{\partial \mathbf{B}}{\partial t} \quad (3.7)$$

$$\nabla \times \mathbf{H} = \frac{\partial \mathbf{D}}{\partial t} \quad (3.8)$$

and taking derivatives with respect to time and space coordinates for the propagation factor given above we find

$$\omega\mu_0\mathbf{H}(\omega) = \mathbf{k} \times \mathbf{E}(\omega) \quad (3.9)$$

$$\omega\epsilon_0\boldsymbol{\kappa}(\omega)\mathbf{E}(\omega) = -\mathbf{k} \times \mathbf{H}(\omega), \quad (3.10)$$

where we have used Fourier expansions for $\mathbf{H}(\mathbf{t})$, $\mathbf{D}(\mathbf{t})$, $\mathbf{E}(\mathbf{t})$ and introduced the relative dielectric tensor $\boldsymbol{\kappa} = \mathbf{1} + \boldsymbol{\chi}$. Rearranging and combining (3.9) and (3.10) the wave equation is obtained:

$$\omega^2/c^2\boldsymbol{\kappa}\mathbf{E}(\omega) = \mathbf{k} \times (\mathbf{E}(\omega) \times \mathbf{k}) = k^2\mathbf{E}(\omega) - [\mathbf{k} \cdot \mathbf{E}(\omega)]\mathbf{k}, \quad (3.11)$$

with c the speed of light in vacuum $c \equiv 1/\sqrt{\mu_0\epsilon_0}$. Defining a vector

$$\mathbf{n} = \mathbf{k}/(\omega/c) \quad (3.12)$$

we rewrite (3.11) as a set of three linear homogeneous equations for the three components of \mathbf{E}

$$\{n^2\delta_{ik} - n_in_k - \kappa_{ik}\}E_k(\omega) = 0. \quad (3.13)$$

Following Einstein's convention we implicitly assume the summation over equal indices. The compatibility condition for this set of equations is that the determinant of coefficients vanishes:

$$\det|n^2\delta_{ik} - n_in_k - \kappa_{ik}| = 0. \quad (3.14)$$

For a system with cubic symmetry or higher and with uniform magnetization along the direction $\mathbf{m}/\hat{\mathbf{z}}$ the relative dielectric tensor is of the form [67, 71]

$$\boldsymbol{\kappa} = \begin{pmatrix} \kappa_{xx} & \kappa_{xy} & 0 \\ -\kappa_{xy} & \kappa_{xx} & 0 \\ 0 & 0 & \kappa_{zz} \end{pmatrix}. \quad (3.15)$$

An intuitive interpretation of this expression follows from the classical response of a free electron in a static magnetic field along $\hat{\mathbf{z}}$ to an applied electric field. For $\mathbf{E}(\omega)$ along $\hat{\mathbf{x}}$ or $\hat{\mathbf{y}}$ the electron starts to oscillate along $\hat{\mathbf{x}}$ or $\hat{\mathbf{y}}$. The corresponding Lorentz force that is exerted on the moving electron is then proportional either to $\hat{\mathbf{x}} \times \hat{\mathbf{z}} = -\hat{\mathbf{y}}$ or $\hat{\mathbf{y}} \times \hat{\mathbf{z}} = \hat{\mathbf{x}}$, explaining the anti-symmetric off-diagonal tensor elements.

For this $\boldsymbol{\kappa}$, (3.14) has two eigenvalues n_1^2 and n_2^2 for each propagation direction \mathbf{k} . The eigenvectors found from (3.13) then correspond to two orthogonal polarization vectors $\hat{\mathbf{e}}_m$, with $m = 1, 2$, usually describing elliptical polarized modes. In analogy with the refractive index n in an isotropic medium defined by $n^2 = \kappa = 1 + \chi$ the refractive indices n_m for these *proper* modes are defined as

$$n_m^2 = \hat{\mathbf{e}}_{m,i}^* \hat{\mathbf{e}}_{m,j} \kappa_{ij} = 1 + \hat{\mathbf{e}}_{m,i}^* \hat{\mathbf{e}}_{m,j} \chi_{ij}. \quad (3.16)$$

We explicitly give the solutions of (3.13) and (3.15) for the high symmetry situations where \mathbf{k} is either parallel or perpendicular to \mathbf{m} , which are important in the determination of the resonant optical constants described in the next chapter.

For \mathbf{k}/\mathbf{m} we obtain from (3.14)

$$n_{\pm}^2 = \kappa_{xx} \pm i\kappa_{xy} = 1 + \chi_{xx} \pm i\chi_{xy}. \quad (3.17)$$

Substitution of this result into equation (3.13) gives for the electric field $E_x/E_y = \pm i$ and the corresponding proper modes are left and right circularly polarized plane waves

$$\mathbf{E}_{\pm}(\mathbf{r}, t) = \frac{1}{\sqrt{2}} E_0(\omega) e^{i(n_{\pm} k_0 z - \omega t)} \begin{pmatrix} 1 \\ \pm i \\ 0 \end{pmatrix} = E_0(\omega) e^{i(n_{\pm} k_0 z - \omega t)} \hat{\mathbf{e}}_{\pm}, \quad (3.18)$$

where $k_0 = \omega/c$.

Similarly for $\mathbf{k} \perp \mathbf{m}$ we find

$$n_{\perp}^2 = \frac{\kappa_{xx}^2 + \kappa_{xy}^2}{\kappa_{xx}} \quad (3.19)$$

and

$$n_{//}^2 = \kappa_{zz}, \quad (3.20)$$

where \perp ($//$) labels linear polarization perpendicular (parallel) to \mathbf{m} . Taking for the propagation direction $\hat{\mathbf{k}} = \hat{\mathbf{y}}$, the proper modes are

$$\mathbf{E}_{//} = E_0(\omega) e^{i(n_{//}k_0y - \omega t)} \begin{pmatrix} 0 \\ 0 \\ 1 \end{pmatrix} \quad (3.21)$$

$$\mathbf{E}_{\perp} = E_0(\omega) e^{i(n_{\perp}k_0y - \omega t)} \begin{pmatrix} 1 \\ \frac{\kappa_{xy}}{\kappa_{xx}} \\ 0 \end{pmatrix}. \quad (3.22)$$

3.2.2 Refractive index: dispersion relations in a magnetic medium

Since for x rays the complex refractive index is close to 1, for a non-magnetic medium it is written as

$$n \equiv 1 - \delta(\omega) + i\beta(\omega). \quad (3.23)$$

$1 - \delta$ and β are related to the frequency dependent dispersion and absorption in the medium. Based on causality arguments it can be shown that, for an isotropic medium, the real and imaginary parts of the refractive index are related by the Kramers-Kronig relations [72, 73]:

$$\delta(\omega) = -\frac{2}{\pi} P \int_0^{\infty} d\omega' \omega' \frac{\beta(\omega')}{\omega'^2 - \omega^2} \quad (3.24)$$

$$\beta(\omega) = \frac{2\omega}{\pi} P \int_0^{\infty} d\omega' \frac{\delta(\omega')}{\omega'^2 - \omega^2} \quad (3.25)$$

where the P stands for the Cauchy principal part of the integral.

In the presence of a magnetic field, time reversal symmetry is broken: both the directions of time and the magnetic field need to be reversed for particles to

retrace their trajectories. As pointed out by D.Y. Smith [68, 70] the Kramers-Kronig relations do no longer hold for the circular polarization modes n_{\pm} in the form of (3.24), but a very similar set of equations can be derived relating the absorption to the dispersion for propagation parallel to the magnetization direction [68, 70] and

$$\delta_+(\omega) + \delta_-(\omega) = -\frac{2}{\pi}P \int_0^{\infty} d\omega' \omega' \frac{\beta_+(\omega') + \beta_-(\omega')}{\omega'^2 - \omega^2} \quad (3.26)$$

$$\delta_+(\omega) - \delta_-(\omega) = -\frac{2\omega}{\pi}P \int_0^{\infty} d\omega' \frac{\beta_+(\omega') - \beta_-(\omega')}{\omega'^2 - \omega^2}. \quad (3.27)$$

Notice that in (3.27) ω and ω' change role with respect to (3.24) and (3.26). For the linear modes the Kramers-Kronig relations hold and we find equations similar to (3.24) and (3.26)

$$\delta_{\parallel}(\omega) + \delta_{\perp}(\omega) = -\frac{2}{\pi}P \int_0^{\infty} d\omega' \omega' \frac{\beta_{\parallel}(\omega') + \beta_{\perp}(\omega')}{\omega'^2 - \omega^2} \quad (3.28)$$

$$\delta_{\parallel}(\omega) - \delta_{\perp}(\omega) = -\frac{2}{\pi}P \int_0^{\infty} d\omega' \omega' \frac{\beta_{\parallel}(\omega') - \beta_{\perp}(\omega')}{\omega'^2 - \omega^2} \quad (3.29)$$

3.3 Polarization dependent resonant magnetic scattering

In the microscopic description of x-ray scattering the atomic scattering tensor \mathbf{f} gives the differential cross section for an atom to scatter a wave with wavevector \mathbf{k} and polarization $\hat{\mathbf{e}}$ into a wave with wavevector \mathbf{k}' and polarization $\hat{\mathbf{e}}'$ [71]

$$\frac{d\sigma}{d\Omega}(\mathbf{k}, \mathbf{k}', \hat{\mathbf{e}}, \hat{\mathbf{e}}') = |r_0 \hat{\mathbf{e}}'^* \cdot \mathbf{f} \cdot \hat{\mathbf{e}}|^2, \quad (3.30)$$

where $-r_0$ is the free electron scattering length.

For high energy photons, the electrons in the atom can be considered free and the scattering amplitude is proportional to the atomic number Z . At lower energies one has to take into account that the electrons are bound by the nucleus. Classically, the response of such bound electrons to a harmonic driving field is that of a damped harmonic oscillator, with a resonance frequency ω_s and a damping constant Γ . The elements of the scattering tensor can be written as

$$f_{ij}(\omega) = \delta_{ij}f^0 + f'_{ij} + if''_{ij}, \quad (3.31)$$

where f^0 is the isotropic free electron term proportional to the atomic number Z . Summed over all the 'oscillators', f' is the dispersion correction and f'' accounts for the corresponding energy dependent dissipation of energy.

In a quantum-mechanics description the resonance frequency is associated with the energy difference $E_\eta - E_\alpha$ between the ground state of the system $|\alpha\rangle$ and an excited state $|\eta\rangle$. This is drawn schematically for the Gd $M_{4,5}$ ($3d \rightarrow 4f$) and Fe $L_{2,3}$ ($2p \rightarrow 3d$) dipole transitions in Fig. 3.1. On the left an atomic multiplet description as applicable to the Gd $M_{4,5}$ edge is shown. The resonance is between the atomic ground state $|JM\rangle$ of the $4f^7$ configuration and the dipole allowed multiplet states $|J'M'\rangle$ of the core-level excited $3d^9 4f^8$ configuration, with J and M the total angular and magnetic quantum numbers. In the elastic scattering event the initial and final states are exactly the same. Quasi-elastic transitions are indicated by the dashed arrow, which contribute $\approx 5\%$ to the resonant cross section [74] but are ignored in this thesis. The polarization state of the photons, indicated by $q = 0$ for linear polarization and $q = \pm 1$ for circular polarization, is transferred to the excited state. Only transitions for which $\Delta M = q$ are allowed, hence the transition probability depends on the direction of the quantization axis.

On the right the single-particle description applicable to the Fe $L_{2,3}$ transition is illustrated. Here an electron from the $2p$ shell resonates with the $3d$ valence band. In this picture, the angular momentum of the incident photon $q = 0, \pm 1$ can be transferred to the photo-excited $2p$ core electron through the spin-orbit coupling, provided it originates from a spin-orbit split level [75]. For circularly polarized light photoelectrons of opposite spins are created for the two helicities since these transfer opposite angular momentum. The spin-split valence band now acts as a 'detector' for the direction of the photoelectron spin and the resonant cross section depends on the relative orientation of the photon angular momentum with respect to the magnetization axis of the polarized $3d$ -band.

3.3.1 Resonant electric dipole scattering

The important x-ray resonances in this thesis are the Gd $M_{4,5}$ and Fe $L_{2,3}$ electric dipole transitions ($E1$). In this case the resonant scattering amplitude is given

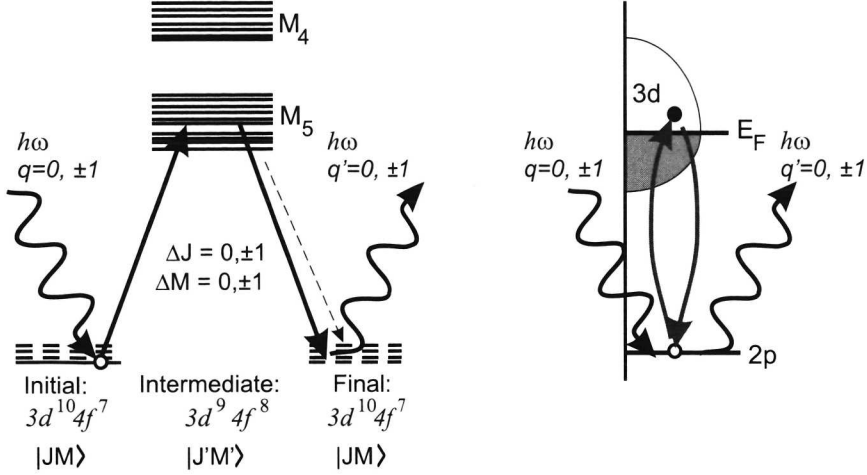


Figure 3.1: Resonant x-ray scattering in the atomic multiplet (left) and single-particle (right) descriptions as applicable to the Gd $M_{4,5}$ and Fe $L_{2,3}$ edges.

by [11]

$$f_{E1}(\mathbf{k}, \mathbf{k}', \omega) = \frac{4\pi}{r_0 k} \sum_{M=-1}^1 [\hat{\mathbf{e}}'^* \cdot \mathbf{Y}_{1M}^{(e)}(\hat{\mathbf{k}}') \mathbf{Y}_{1M}^{(e)*}(\hat{\mathbf{k}}) \cdot \hat{\mathbf{e}}] F_{1M}^{(e)}(\omega) \quad (3.32)$$

where $\mathbf{Y}_{LM}^{(e)}$ are vector spherical harmonics and the $\hat{\mathbf{e}}$, $\hat{\mathbf{e}}'$, $\hat{\mathbf{k}}$ and $\hat{\mathbf{k}}'$ are the unit vectors corresponding to polarization modes and wavevectors of the incident and scattered waves. The transition matrix element $F_{1M}^{(e)}(\omega)$ is the energy dependent amplitude of the resonance and is determined by the radial distribution functions of the initial and final states

$$F_{1M}^{(e)}(\omega) = \sum_{\alpha, \eta} \left(\frac{p_{\alpha} p_{\alpha}(\eta) \Gamma_x(\alpha M \eta) / \Gamma(\eta)}{x(\alpha, \eta) - i} \right). \quad (3.33)$$

Here, p_{α} is the probability to find the ion existing in the initial state $|\alpha\rangle$. $|\eta\rangle$ is the excited state with $p_{\alpha}(\eta)$ the probability that it is vacant for transition from $|\alpha\rangle$. Γ_x gives the partial line width for dipole radiative decay from $|\eta\rangle$ to $|\alpha\rangle$, $\Gamma(\eta)$ is the total width for $|\eta\rangle$ determined by all radiative and non radiative decay processes for $|\eta\rangle$. In the resonant denominator, $x(\alpha, \eta) = (E_{\eta} - E_{\alpha} - \hbar\omega) / (\Gamma(\eta)/2)$ is the deviation from resonance in units of $\Gamma/2$. For photon energy $\hbar\omega = E_{\eta} - E_{\alpha}$, the divergence of this term causes a strong enhancement of the scattering amplitude.

The factor $\hat{\mathbf{e}}'^* \cdot \mathbf{Y}_{1M}^{(e)}(\hat{\mathbf{k}}') \mathbf{Y}_{1M}^{(e)*}(\hat{\mathbf{k}}) \cdot \hat{\mathbf{e}}$ gives the angular dependence and equation (3.32) can be reduced to [11]

$$f_{E1} = (\hat{\mathbf{e}}'^* \cdot \hat{\mathbf{e}})F^{(0)} - i(\hat{\mathbf{e}}'^* \times \hat{\mathbf{e}}) \cdot \mathbf{m}F^{(1)} + (\hat{\mathbf{e}}'^* \cdot \mathbf{m})(\hat{\mathbf{e}} \cdot \mathbf{m})F^{(2)}, \quad (3.34)$$

where \mathbf{m} is the direction of the quantization axis defined here as the direction of the local magnetic moment of the ion and

$$\begin{aligned} F^{(0)} &= \frac{3}{4r_0k} [F_{11} + F_{1-1}] \\ F^{(1)} &= \frac{3}{4r_0k} [F_{11} - F_{1-1}] \\ F^{(2)} &= \frac{3}{4r_0k} [2F_{10} - F_{11} - F_{1-1}] \end{aligned} \quad (3.35)$$

are linear combinations of the atomic oscillator strengths (3.33) for dipole scattering.

For comparison of the microscopic scattering amplitude with the macroscopic dielectric tensor it is convenient to reformulate (3.34) in tensor notation:

$$f(\hat{\mathbf{e}}', \hat{\mathbf{e}}) = \hat{e}'_i \hat{e}_j f_{ij} = \hat{\mathbf{e}}'^* \cdot \mathbf{f} \cdot \hat{\mathbf{e}}, \quad (3.36)$$

where for (3.34) the elements f_{ij} of the rank 2 tensor \mathbf{f} are given by

$$f_{ij} = (f^0 + F^{(0)})\delta_{ij} - i\epsilon_{ijk}m_k F^{(1)} + m_i m_j F^{(2)} \quad (3.37)$$

with ϵ_{ijk} the Levi-Civita symbol and where we have added the free electron factor f^0 to the resonant terms f_{E1} .

3.3.2 Refractive index and forward scattering amplitude

For the specific case of an atom quantized along $\hat{\mathbf{z}}$, $\mathbf{m} = (0, 0, 1)$ we find

$$\mathbf{f} = \begin{pmatrix} f^0 + F^{(0)} & -iF^{(1)} & 0 \\ iF^{(1)} & f^0 + F^{(0)} & 0 \\ 0 & 0 & f^0 + F^{(0)} + F^{(2)} \end{pmatrix}, \quad (3.38)$$

which is an anti-symmetric tensor of the form of the dielectric tensor (3.15) found on basis of symmetry arguments for a macroscopic medium magnetized along $\hat{\mathbf{z}}$ in the dipole approximation. Indeed it can be shown that in general [66, 67]

$$\chi_{ij}(\omega) = \frac{-4r_0\pi\rho}{k^2} f_{ij}(\omega), \quad (3.39)$$

Table 3.1: Scattering cross sections for the proper polarization modes for propagation parallel and perpendicular to \mathbf{m} .

$\mathbf{m} // \mathbf{k}$	$\mathbf{m} \perp \mathbf{k}$
$\hat{\mathbf{e}}_{\pm} = \frac{1}{\sqrt{2}}\sqrt{2}(1, \pm i, 0)$	$\hat{\mathbf{e}}_{//} = (0, 0, 1)$ $\hat{\mathbf{e}}_{\perp} = (0, 1, 0)$
$f_{+}(\omega) = f^0 + F^{(0)}(\omega) - F^{(1)}(\omega)$	$f_{//}(\omega) = f^0 + F^{(0)}(\omega) + F^{(2)}(\omega)$
$f_{-}(\omega) = f^0 + F^{(0)}(\omega) + F^{(1)}(\omega)$	$f_{\perp}(\omega) = f^0 + F^{(0)}(\omega)$

where ρ the number density of scatterers.

Equation (3.39) connects the microscopic properties to the macroscopic properties of the medium and we can now express the refractive index n_m for the proper propagation modes m in terms of the forward atomic scattering amplitudes f_m , for $\mathbf{k}' = \mathbf{k}$. In that case $\hat{\mathbf{e}} = \hat{\mathbf{e}}' = \hat{\mathbf{e}}_m$, and f_m is defined as

$$f_m = f^0 + f'_m + i f''_m = \hat{\mathbf{e}}_m^i \hat{\mathbf{e}}_m^j f_{ij}(\omega). \quad (3.40)$$

The f_m for the linear and circular polarized proper modes of section 3.2.1 are listed in Table 3.1.

Combination of (3.39) and (3.40) with (3.16) gives

$$n_m(\omega)^2 = 1 - \frac{4\pi r_0 \rho}{k^2} f_m \quad (3.41)$$

Since δ and β are small n^2 can be approximated by $n^2 = 1 - 2\delta + 2i\beta$, so that

$$\beta_m = \frac{-2\pi r_0 \rho}{k^2} f''_m \quad (3.42)$$

$$\delta_m = \frac{2\pi r_0 \rho}{k^2} (f^0 + f'_m). \quad (3.43)$$

It then follows that $f^0 + f'_m$ and f''_m can be determined from the phase, respectively the amplitude of a propagating plane wave in a uniformly magnetized medium. Furthermore, since the real and imaginary parts of the refractive index are related via the dispersion relations as given in section 3.2.2 it is sufficient to measure either β_m or δ_m directly.

3.3.3 Single scattering

So far we have discussed the propagation of light in a *uniformly* magnetized medium. In a system where the magnetization is inhomogeneous a propagating

plane wave will be modulated in phase and amplitude. Here a description of the resulting far field diffracted intensity is given in the framework of the single scattering theory.

Within the first order Born approximation we take for the amplitude and phase of the incident wave at position \mathbf{r} that of the vacuum plane wave $E_0 e^{i\mathbf{k}\cdot\mathbf{r}}$. The scattered field $E_s(\mathbf{R})$ at a position \mathbf{R} due an atom at position \mathbf{r} with magnetization $\mathbf{m}(\mathbf{r})$, as indicated in Fig. 3.2, is then given by [67, 76]

$$\mathbf{E}_s(\mathbf{R}) = \frac{-r_0}{|\mathbf{R} - \mathbf{r}|} \mathbf{f}(\mathbf{m}(\mathbf{r})) E_0 e^{-i(\mathbf{k}' - \mathbf{k})\cdot\mathbf{r}} e^{ik'R}. \quad (3.44)$$

The factor $e^{-i(\mathbf{k}' - \mathbf{k})\cdot\mathbf{r}}$ describes the phase of the wave scattered at \mathbf{r} with respect to the wave scattered at the origin \mathbf{O} .

Integrating over the scattering volume and with $\rho_a(\mathbf{r})$ the density of scatterers we get in the far field limit, $R \gg r_m$,

$$\mathbf{E}_s(\mathbf{R}) = \frac{-r_0 e^{ik'R}}{R} \int_V d\mathbf{r} \rho_a(\mathbf{r}) \mathbf{f}(\mathbf{m}(\mathbf{r})) E_0 e^{-i\mathbf{q}\cdot\mathbf{r}} \quad (3.45)$$

where we have introduced the momentum transfer $\mathbf{q} = \mathbf{k}' - \mathbf{k}$ and it is implicitly assumed that a wave scattered at \mathbf{r} propagates undisturbed. For the thin films discussed in this thesis ρ_a is constant on the length scale probed in the scattering experiment and only the \mathbf{r} dependent magnetization direction $\mathbf{m}(\mathbf{r})$ needs to be taken into account. Equation (3.45) expresses the familiar result that the scattered field (3.45) is the Fourier transform of the scattering density $\rho_a \mathbf{f}(\mathbf{m}(\mathbf{r}))$.

3.3.4 Polarization space

Since the polarization vector is normal to \mathbf{k} for the incident wave and to \mathbf{k}' for the scattered wave, the tensor \mathbf{f} can be expressed in terms of the 2-dimensional space of the polarization planes. A common choice for the basis vectors that span these planes are the linear polarization vectors parallel and perpendicular to the scattering plane spanned by \mathbf{k} and \mathbf{k}' : $\lambda = \{\hat{\sigma}, \hat{\pi}\}$ and $\lambda' = \{\hat{\sigma}', \hat{\pi}'\}$ as illustrated in Fig. 3.3. This was worked out by Hill and McMorro [77]. They wrote the scattering tensor as a 2×2 matrix. The matrix elements bring out the polarization dependence and directly give the amplitudes for scattering $\hat{\sigma} \rightarrow \hat{\sigma}'$,

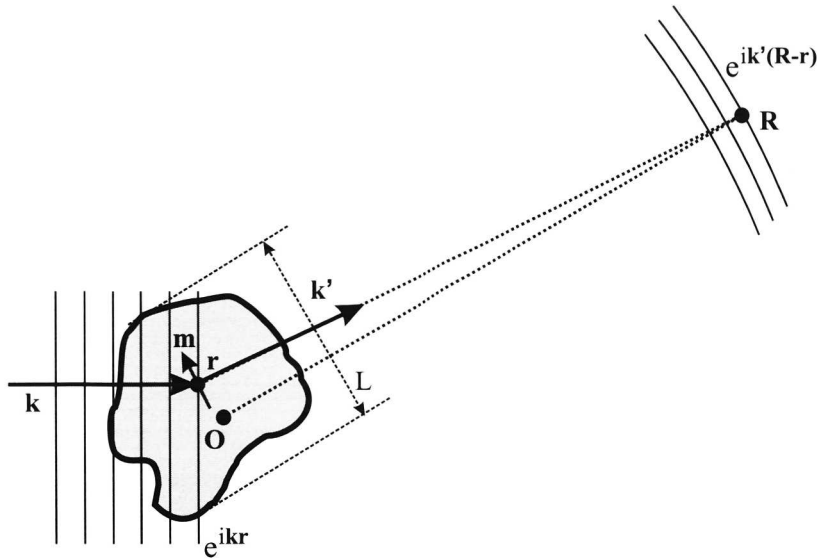


Figure 3.2: Single scattering approximation: The incident field with wavevector \mathbf{k} is scattered by an atom at \mathbf{r} into the direction \mathbf{k}' . In the far field the spherical scattered waves may be approximated by a plane wave if $R \gg L$ and the field at \mathbf{R} can be integrated over the scattering volume as explained in the text.

$\hat{\sigma} \rightarrow \hat{\pi}'$, $\hat{\pi} \rightarrow \hat{\pi}'$ and $\hat{\pi} \rightarrow \hat{\sigma}'$. Formally the transformation can be written as

$$f_{\lambda'\lambda} = \hat{\mathbf{e}}_{\lambda'}^{i*} \hat{\mathbf{e}}_{\lambda}^j f_{ij} \quad (3.46)$$

where the basis vectors $\hat{\mathbf{e}}_{\lambda}$ act as transformation matrices projecting the 3-dimensional physical space onto the 2-dimensional polarization space labelled by the indices λ and λ' [71].

In the limit of small-angle scattering we may approximate the scattering amplitude by that for forward scattering ($\mathbf{k} = \mathbf{k}'$). For the specific case of light incident along $\hat{\mathbf{z}}$ and taking for the polarization basis $\lambda = \lambda' = \{\mathbf{x}, \mathbf{y}\}$ the scattering matrix is given by

$$\mathbf{f}(\mathbf{r}) = \begin{pmatrix} 1 & 0 \\ 0 & 1 \end{pmatrix} (f^0 + F^{(0)}) + \begin{pmatrix} 0 & -im_z(\mathbf{r}) \\ im_z(\mathbf{r}) & 0 \end{pmatrix} F^{(1)} + \begin{pmatrix} m_x^2(\mathbf{r}) & m_x(\mathbf{r})m_y(\mathbf{r}) \\ m_x(\mathbf{r})m_y(\mathbf{r}) & m_y^2(\mathbf{r}) \end{pmatrix} F^{(2)}. \quad (3.47)$$

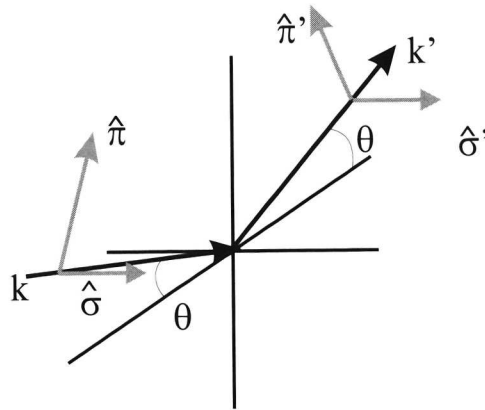


Figure 3.3: Scattering geometry, indicated are the incident, \mathbf{k} , and scattered \mathbf{k}' wavevectors and the corresponding linear polarization vectors parallel, $\hat{\pi}$ and $\hat{\pi}'$, and perpendicular, $\hat{\sigma}$ and $\hat{\sigma}'$, to the scattering plane.

This expression shows explicitly that the $F^{(1)}$ term is sensitive to the magnetization along \mathbf{k} whereas the $F^{(2)}$ term is sensitive to products of the magnetization components in the polarization plane.

DETERMINATION OF THE RESONANT MAGNETO-OPTICAL CONSTANTS AT THE Gd $M_{4,5}$ AND Fe $L_{2,3}$ EDGES

In the previous chapter it was shown that the resonant magnetic scattering amplitude consists of three terms. Each term is the product of an angular dependent factor describing the geometry and an atomic resonant factor $F^{(0)}$, $F^{(1)}$ or $F^{(2)}$, which depends on the radial distribution function of the core level electron and the valence electrons involved in the resonance. For the quantitative interpretation of resonant scattering experiments, knowledge of the $F^{(n)}$ is essential. Since these are complex numbers whose real and imaginary parts are connected by Kramers-Kronig transforms, it suffices to measure either one of these parts directly. The real part can be obtained by measuring the resonant diffraction or reflection angles of multilayers [78, 79] or thin films [80] or from measurements of the Faraday effect [81, 82, 83] (the rotation of the polarization angle in transmission). The latter requires multilayer polarizers which are not readily available.

As will be shown in this chapter, the imaginary part can be obtained in a conceptually more straightforward way from the polarization-dependent absorption spectra measured on thin films in transmission. A number of groups have tried this approach in the soft x-ray range [84, 85, 86, 87]. However it is compli-

cated by the high absorption cross sections, which require extremely thin samples and supports, with concomitant difficulties in knowing the thickness with sufficient precision and in producing sufficiently homogeneous samples. As we will show, the availability of modern high transmission supports now enables one to overcome these difficulties and we use this method to obtain high quality data for the optical constants of $\text{Gd}_{1-x}\text{Fe}_x$ thin films around the Gd $M_{4,5}$ and Fe $L_{2,3}$ edges.

The reliability of these optical constants will be demonstrated by comparison of the scattering cross section calculated from these absorption data with the measured scattered intensity of the magnetic stripe lattices in the same samples. In describing the scattered intensity two points of view can be taken: the macroscopic description in terms of a space modulated refractive index, or a description in terms of the atomic scattering amplitude. The usefulness of the first is limited, since as discussed in the previous chapter the refractive index is only defined for proper propagation modes in homogeneous regions and is difficult to apply to more complicated magnetic structures. We choose however to use this description in this chapter in order to clarify the role of dichroic attenuation and birefringence.

4.1 Experimental

Pure Gd and amorphous $\text{Gd}_x\text{Fe}_{1-x}$ magnetic thin films were grown and characterized as described in Chapter 2. Thicknesses were chosen to give approximately $1/e$ absorption using calculated cross sections from Thole [3]. As supports we used 100 nm thick commercially available Si_3N_4 TEM windows, which have a transmission of $\sim 95\%$ at the Gd $M_{4,5}$ and $\sim 85\%$ at the Fe $L_{2,3}$ energy. Typical window dimensions were $0.5 \times 0.5 \text{ mm}^2$. The *ex situ* prepared films were capped with a 2 nm Al protection layer in order to prevent oxidation.

Transmission experiments were performed during several runs at beamline ID08 [88] at the European Synchrotron Radiation Facility (ESRF). This beamline is equipped with two *Apple II* undulators, optimized for polarization dependent soft x-ray spectroscopies. The photon energy is tunable between 0.4 and 1.6 keV and the polarization can be controlled such that the x rays are either 100 % left/right circularly polarized or vertical/horizontal linearly polarized. The

'Dragon' type spherical grating monochromator has a best energy resolution close to $\frac{\Delta E}{E} = 5 \cdot 10^{-4}$ at 850 eV. For the present experiment at 1200 eV the experimental resolution was estimated to be 0.3 eV. A vertical re-focusing mirror, which is used for harmonic rejection, focuses the beam to a minimum vertical size of 40 μm at the sample position. The horizontal width is typically 600 μm , determined by a horizontal focusing mirror.

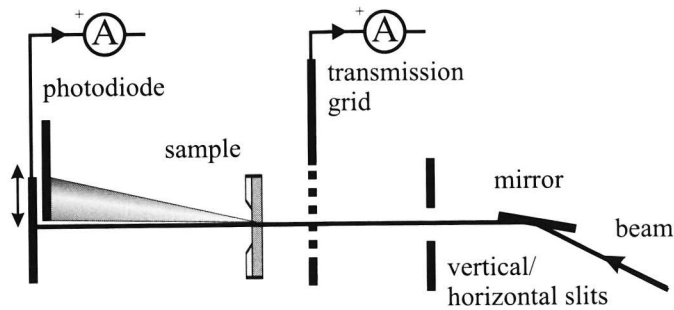


Figure 4.1: Schematic experimental layout for the transmission experiment. The photodiode can be translated and intercepts either the scattered intensity as shown or the transmitted intensity in the direct beam.

The experimental layout from the re-focusing mirror onward is sketched in Fig. 4.1. The intensity of the incident beam upstream of the sample, I_0 , was monitored by the photoelectron current from a fine gold-coated Cu grid. A photodiode was used to detect the transmitted intensity, I_t . Absolute transmission factors were determined by measuring the ratio of the two detector signals with and without the sample. A set of slits in front of the I_0 monitor was used to produce a beam size smaller than the Si_3N_4 window dimensions.

The samples were attached to a cold finger inserted between the poles of a horizontal 0.5 T in-vacuum electromagnet. The magnet field was sufficiently high to saturate all samples. For x-ray magnetic circular dichroism (XMCD) measurements the field direction was parallel to the beam. The magnetization was flipped at each data point to obtain the dichroism spectrum, and the measurements were performed for two helicity directions, which gave indistinguishable results. The x-ray magnetic linear dichroism (XMLD) was measured with the sample magnetized perpendicular to the beam, taking the difference of consecutive scans with horizontal or vertical linear polarization.

4.2 Absorption and magnetic dichroism cross sections

In transmission experiments the absorption coefficient $\mu = 2\beta k$ follows from the extinction of the incident beam by a homogeneous (*i.e.* non-scattering) film as described by Lambert-Beer's law:

$$\mu = -1/D \ln(I_t/I_0) \quad (4.1)$$

where I_t and I_0 are the transmitted and incident intensities and D the film thickness.

The total absorption coefficient μ_m measured for a proper circular (\pm) or linear ($\perp, //$) polarization mode is related to the forward scattering cross section through (3.42)

$$\mu_m = -\frac{f''_{r,m} 4\pi\rho_r r_0}{k} - \sum_n \frac{f''_n 4\pi\rho_n r_0}{k} \quad (4.2)$$

where $f''_{r,m}$ is the imaginary part of the forward resonant scattering amplitudes, and ρ_r is the corresponding atomic number density. The non-resonant second term f''_n describes the absorption by the Si_3N_4 support, the Al capping layer and the non-resonant Fe or Gd species. They contribute to a magnetization independent background absorption, which can be obtained from tabulated atomic absorption cross section calculations [89] using the known thickness and atomic number densities ρ_n .

The three measurable spectra are the non-magnetic XAS spectrum, the XMCD spectrum defined as $\mu_+ - \mu_-$ and the XMLD spectrum defined as $\mu_{//} - \mu_{\perp}$. After subtraction of the non-resonant background the XAS gives the imaginary part of the resonant charge scattering length $F^{(0)}(E)$ while the XMCD directly proportional to the imaginary part of $F^{(1)}(E)$ and the XMLD gives the imaginary part of $F^{(2)}(E)$, as follows from Table 3.1 and equations(3.34) and (4.2).

The transmission at room temperature of a non-magnetic 16 nm Gd sample is shown in Fig. 4.2. The raw signal shown in the inset has been corrected for the sloping transmission of the 100 nm Si_3N_4 support and the energy dependencies of the detectors. The non-resonant background calculated from the known thickness and tabulated cross sections[89] is also shown, and gives good agreement with the pre- and post edge regions. Using Lambert-Beer's law and the known atomic density and thickness, the absolute cross section per atom can be

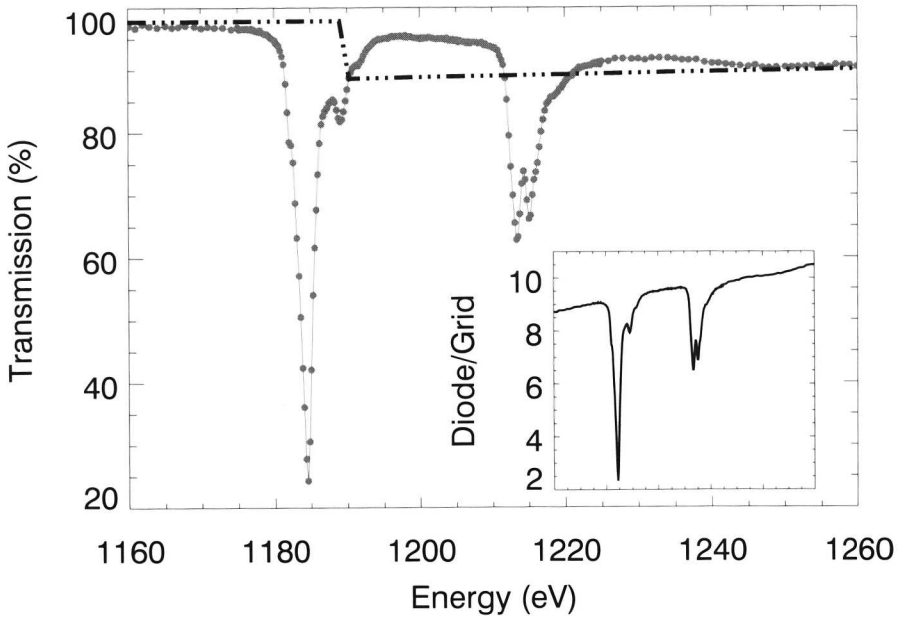


Figure 4.2: $M_{4,5}$ transmission spectrum of a 16 nm Gd thin film at room temperature (grey dots). Dash-dotted line: non-resonant contribution, see text. Inset: raw data.

calculated as shown in the top panel of Fig. 4.3.

Also shown in Fig. 4.3 are the Gd $M_{4,5}$ XMCD and XMLD spectra of $Gd_{1-x}Fe_x$ thin films ($x=72.5\%$ and 83.3%) taken during different experimental runs at room temperature and 20 K. The obtained values for the different compositions were well within the experimental error of 2%. The XMCD spectrum at 20 K has a maximum amplitude that is ca. 90 % of the maximum isotropic x-ray absorption, implying a fully saturated 4f moment [90]. The room temperature XMCD spectra have been scaled up to the 20 K spectra by a multiplication factor of 1.31. Since the XMCD is linearly proportional to the total Gd moment M_{Gd} , this implies that at room temperature M_{Gd} is reduced by a factor $1/1.31$ compared to the fully saturated 20 K moment. The 20 K XMCD data are much noisier and have a sloping background over the resonance, and for the calculations of the atomic scattering amplitudes we used the much better quality room-temperature data instead. The XMLD spectrum at room temperature has been scaled by a factor $1.31^2 = 1.72$. Since the XMLD is proportional to M_{Gd}^2 this is

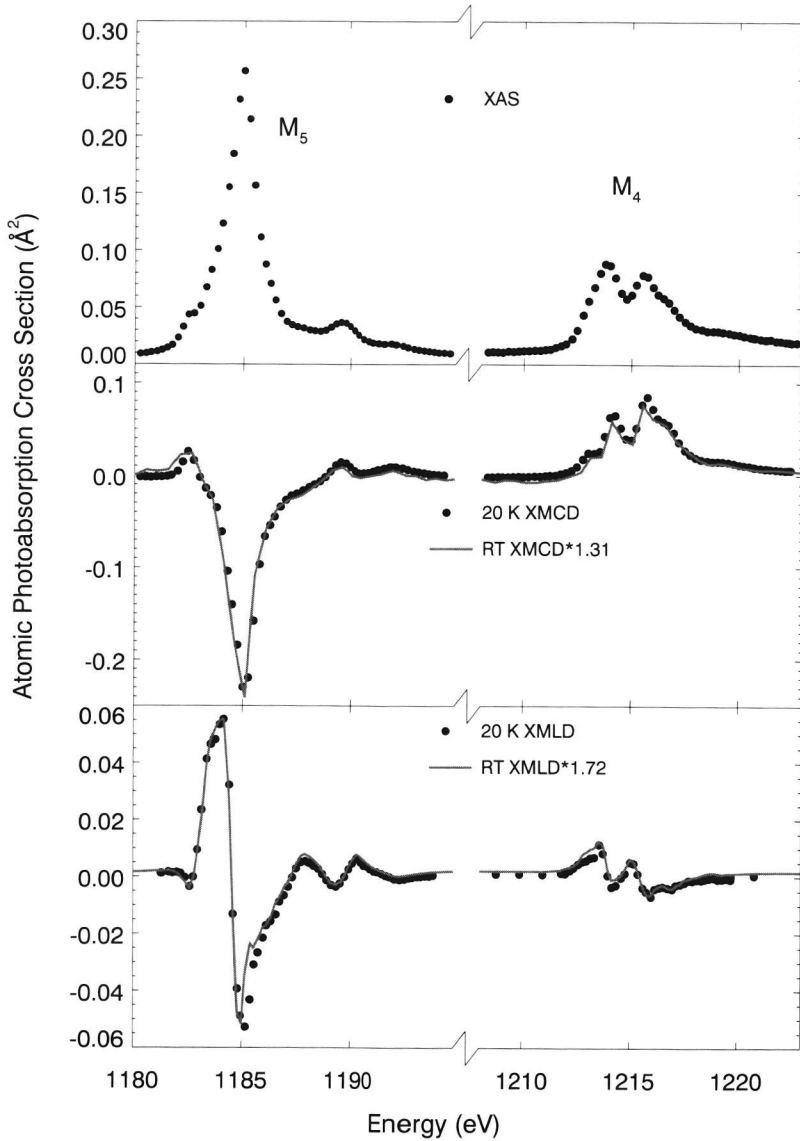


Figure 4.3: XAS, XMCD and XMLD spectra at 20K (symbols) and room-temperature (lines). The room temperature spectra are scaled by 1.31 for the XMCD and by 1.31² for the XMLD.

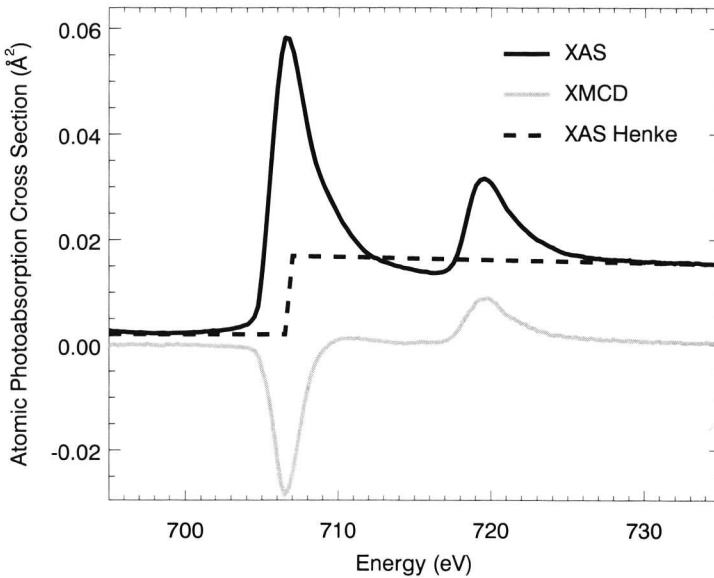


Figure 4.4: The Fe $L_{2,3}$ x-ray absorption and circular magnetic dichroism spectra of a 40 nm $Gd_{27.5}Fe_{72.5}$ thin film at room temperature. Dash-dotted line: non-resonant contributions from [89].

consistent with the reduction of M_{Gd} at room temperature found for the XMCD.

The Fe $L_{2,3}$ spectra for the $Gd_{27.5}Fe_{72.5}$ magnetic thin film are shown in Fig. 4.4. In comparison to the Gd $M_{4,5}$ the resonance is weaker. The linear dichroism at this edge was less than 1 % and we were unable to obtain reliable data with the small beam size imposed by the support window dimensions. The much smaller linear dichroism is due to the smaller spin-orbit interaction in the Fe $3d$ -shell in comparison with the Gd $4f$ -shell [91, 92].

4.3 Kramers-Kronig transformations

The dispersion relations (3.24), (3.27) and (3.29) allow us to calculate the x-ray dispersion and magnetic birefringence from the experimental absorption and magnetic dichroism spectra. The principal value integrals were approximated

numerically by calculating the Riemann sum over the spectra, leaving out the pole at $\omega = \omega'$. The XAS spectrum was combined with tabulated values [89] to take into account the absorption due to all other transitions from 10 eV to 30 keV. We enlarged the integration range until no changes in the resonant dispersion were found. For the XMCD and XMLD it suffices to integrate the experimental spectra, from 1150 eV to 1250 eV, since the magnetic dichroism is negligible away from the sharp $M_{4,5}$ resonance. Other dichroic edges such as the $L_{2,3}$ and $M_{2,3}$ transitions for Gd are far away in energy. Back-transformation of the calculated dispersion and birefringence curves reproduces the absorption and dichroism spectra with a maximum deviation of $\sim 2\%$ at the extremal values.

The results are presented in Fig. 4.5 which shows the complex charge $F^{(0)}$, circular magnetic $F^{(1)}$ and linear magnetic $F^{(2)}$ scattering amplitudes in units of the free electron scattering length $-r_0$. The imaginary parts obtained from the transmission experiments are shown at the top, the real parts obtained from the dispersion relation at the bottom. The resonant scattering amplitudes are substantially larger than the constant Thomson scattering amplitude f^0 of 64 electrons, indicated by the dash-dotted line. On the right axis, the atomic absorption cross section corresponding to the imaginary part of the scattering amplitudes is given, for a fixed energy of 1200 eV which results in a $\approx 5\%$ error over this energy range.

The curves in Fig. 4.5 represent the real and imaginary parts of the atomic scattering factors at the Gd $M_{4,5}$ resonance. Since they have a very large amplitude, they completely determine the magneto-optical properties of the medium. As an example we take the Faraday rotation and ellipticity angle for linear polarized light that would be obtained in a Gd thin film, for normal incidence and uniform perpendicular magnetization. In this case the linear polarized wave must be decomposed into the two allowed circular modes $\hat{\mathbf{e}}_{\pm}$, and the two propagating waves obtain an amplitude and phase difference, due to the circular dichroism respectively birefringence. The amplitude difference leads to an elliptic polarization, while the birefringence results in a rotation of the polarization angle. At optical frequencies these effects are known as the Faraday effect. The complex Faraday angle is given by [82, 93]

$$\epsilon_F = \theta_F + i\alpha_F = \frac{n_+ - n_-}{2}kD, \quad (4.3)$$

where α_F is the ellipticity and θ_F is the Faraday rotation angle, D is the thickness

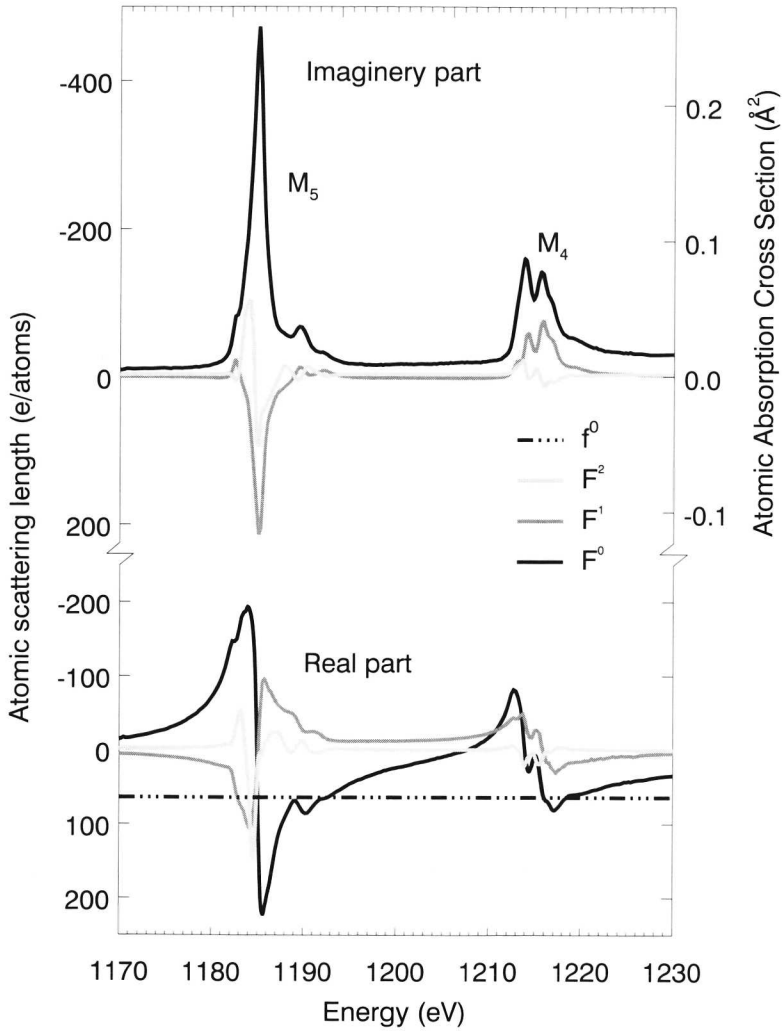


Figure 4.5: Resonant amplitudes at the Gd $M_{4,5}$ edges. Shown are the complex charge $F^{(0)}$, circular magnetic $F^{(1)}$, and linear magnetic $F^{(2)}$, atomic scattering factors as function of energy in units of r_0 . top: Imaginary parts, from the experimentally determined absorption cross section. bottom: Real part, Kramers-Kronig transform of the imaginary parts. Right axis: approximate atomic cross sections in \AA^2 using a fixed wavelength for $E = 1200$ eV. Dash-dotted line: high-energy limit of the atomic scattering amplitude $Z = 64$.

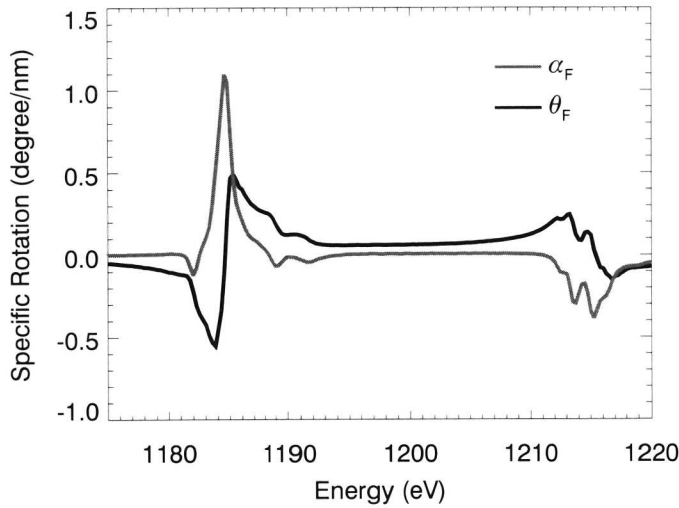


Figure 4.6: Gd $M_{4,5}$ resonant Faraday ellipticity α_F , and rotation angle θ_F for bulk Gd at 20 K.

of the film. The rotation and ellipticity angle are plotted in Fig. 4.6 as a function of the photon energy. At the M_5 resonance the maximum rotation angle is $0.6^\circ/\text{nm}$ and the maximum ellipticity is $1.2^\circ/\text{nm}$. The specific rotating power per unit length is twice that for pure Fe thin films [82], and is roughly an order of magnitude larger than the same effects at optical frequencies.

4.4 Optical constants versus scattered intensity

In order to test the validity of the optical constants as given in Fig. 4.5 we measured the energy dependence of the intensity scattered by an aligned magnetic stripe lattice. A natural way to describe both the absorption and scattering effects is to write the transmitted field in terms of the refractive index. Light incident on the stripe lattice sees either an up- or down-domain, or a domain wall and obtains a phase lag and absorption depending on the in-plane coordinate. The near field just after the sample is therefore modulated in phase and amplitude and can be written as an average field, that forms the transmitted beam plus a modulated field. The modulation produces interference patterns

in the far-field.

We will initially simplify the analysis by neglecting the in-plane domain wall and closure magnetization and assume a modulated magnetization profile, $m_z(y)$ that is periodic in y and constant in x . For a normally incident plane wave, $\mathbf{k} // \mathbf{m} // \hat{\mathbf{z}}$, the refractive index must then be described by the refractive indices $n_{\pm} = 1 - \delta_{\pm} + i\beta_{\pm}$ for the allowed circular polarization modes $\hat{\mathbf{e}}_{\pm}$.

For an incident circular polarized plane wave with helicity $\sigma = \pm$ the refractive index at a position y can be written as

$$n(y) = \bar{n} + \sigma m_z \Delta n \tag{4.4}$$

with

$$\bar{n} = \frac{n_+ + n_-}{2} = 1 - \bar{\delta} + i\bar{\beta}, \tag{4.5}$$

a constant helicity averaged part and

$$\Delta n = \frac{n_+ - n_-}{2} = -\Delta\delta + i\Delta\beta, \tag{4.6}$$

the magneto-optic part sensitive to the magnetization.

It follows that the transmitted electric field can be written as the product of an average part and a modulated part depending on $m_z(y)$

$$E(y) = E_0 e^{ikD\bar{n}} e^{ikD\sigma m_z(y)\Delta n} \tag{4.7}$$

where E_0 is the amplitude of the incident plane wave. The factor $e^{ikD\bar{n}}$ gives rise to an irrelevant phase shift $e^{ikD(1-\bar{\delta})}$ and an absorption $e^{-kD\bar{\beta}}$ equivalent to the helicity averaged attenuation for the uniformly magnetized sample.

The modulated phase and amplitude factor $e^{ikDm_z(y)\Delta n}$ will scatter light out of the incident direction. In the Fraunhofer approximation the far-field amplitude is the Fourier transform of (4.7)

$$E(q_y) = E_0 e^{-kD\bar{\beta}} \int e^{ikDm_z(y)\Delta n} e^{iq_y y} dy \tag{4.8}$$

where we have omitted the common phase factor $e^{ikD(1-\bar{\delta})}$ and ignored other prefactors of the Fourier integral that are not important here.

Provided $kD\Delta\delta$ and $kD\Delta\beta$ are small, we may expand the argument of the Fourier transform as

$$\begin{aligned}
 e^{-ikDm_z(y)\Delta\delta} e^{-kDm_z(y)\Delta\beta} &\approx (1 - ikDm_z(y)\Delta\delta)(1 - kDm_z(y)\Delta\beta) \\
 &\approx 1 - kDm_z(y)(i\Delta\delta + \Delta\beta) \\
 &\approx 1 + ikDm_z(y)\Delta n \\
 &\approx 1 + im_z(y)\epsilon_F
 \end{aligned} \tag{4.9}$$

and we obtain

$$E(q_y) = E_0 e^{-kD\bar{\beta}} \int [1 - m_z(y)kD(i\Delta\delta + \Delta\beta)] e^{iq_y y} dy, \tag{4.10}$$

where the first term is non-zero only at $q_y = 0$ and can be interpreted as the transmitted beam. The scattered field at $q_y \neq 0$ is proportional to the Fourier transform of the out-of-plane magnetic periodic structure times the frequency dependent magneto-optical constants damped by the helicity averaged absorption spectrum.

The far-field Fraunhofer diffraction pattern from the aligned stripe lattice consists of a series of diffraction maxima periodically spaced in reciprocal space. Here we are interested in the energy dependence of the total scattered intensity $I_s(E)$. Integrating $|E(q_y)|^2$ over q_y leaving out the direct beam at $q_y = 0$, the Fourier transform enters as a constant pre-factor in the energy dependence

$$I_s(E) \propto I_0 e^{-2kD\overline{\beta(E)}} k^2 D^2 [\Delta\delta(E)^2 + \Delta\beta(E)^2] \tag{4.11}$$

$$\propto I_0 e^{-2kD\overline{\beta(E)}} \left(\frac{2\pi r_0 D \rho}{k} \right)^2 |F^{(1)}(E)|^2, \tag{4.12}$$

where we have used the relation

$$\Delta n(E) = -\frac{2\pi r_0 \rho}{k^2} F^{(1)}(E) \tag{4.13}$$

that follows from (3.41).

The total scattered intensity $I_s(E)$ around the Gd $M_{4,5}$ and the Fe $L_{2,3}$ edges was measured by moving the diode to a position just out of the primary beam where it intercepts only the top half of the diffraction pattern (Fig. 4.1). To compare $I_s(E)$ with $\Delta\delta(E)^2 + \Delta\beta(E)^2$ we need to divide it by the average attenuation factor $e^{-2\overline{\beta(E)}kD}$ that appears in (4.12). A reasonable estimate can be obtained by

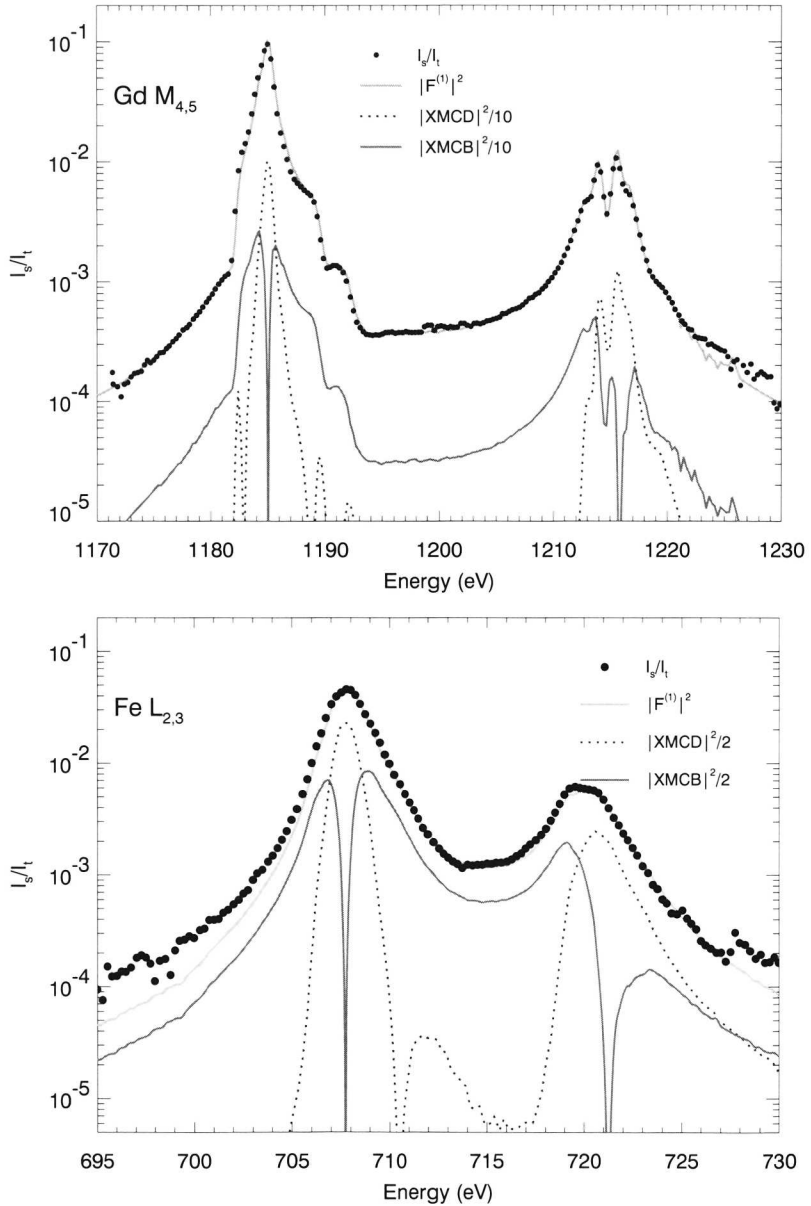


Figure 4.7: Magnetic scattering cross section I_s/I_t (dots) for an aligned stripe lattice compared with the scaled scattering cross section computed from $|F^{(1)}|^2$ (grey lines). Top: Gd $M_{4,5}$ resonance. Bottom: Fe $L_{2,3}$ resonance. The separate contributions from the circular dichroism and birefringence are shown divided by a factor 10 at top figure and a factor 2 at the bottom figure.

having the diode intercept both the transmitted and scattered radiation $I_t(E)$. The spectrum of $I_s(E)/I_t(E)$ is shown in Fig. 4.7, and is compared with the same curve for the resonant scattering factor $|F^{(1)}(E)|^2$ obtained from the absorption data and Kramers-Kronig transform, using equation 4.13 to express it in terms of $\Delta\delta$ and $\Delta\beta$. For the Gd $M_{4,5}$, shown at the top, a very satisfactory agreement is obtained over 4 orders of magnitude, which proves the validity of the Kramers-Kronig transform for the circular dichroic scattering factor $F^{(1)}$. It is worthwhile to point out that at the resonance the scattering contrast is completely absorptive, but elsewhere is mainly resulting from the dispersive part.

A similar analysis can be made for the Fe $L_{2,3}$ edges, with results given in the bottom graph of Fig. 4.7. Again a good match between measured intensities and calculated cross sections is obtained over several orders of magnitude. It should be noted that the Fe L-edge spectrum is much less peaked, and that the scattered intensity is lower than that found at the Gd M-edge.

In the above discussion we have assumed that the refractive index was dependent on $m_z(y)$ only, in other words we have neglected the possibility of scattering by domain walls or closure domains that have a linear dichroic and birefringent contrast. As will be discussed in Chapter 5 these magnetization components produce weak even order satellites with intensity proportional to $|F^{(2)}|^2$. In anticipation of this discussion we give in Fig. 4.8 the ratio of $|F^{(2)}|^2/|F^{(1)}|^2$ at the Gd M_5 edge. The most striking feature of this figure is that it shows that the linear dichroic contrast term $F^{(2)}$ is important at the low energy side of the main absorption peak at 1185 eV. The data points that are also shown in Fig. 4.8 give the ratio of the second to first order diffraction maxima as a function of energy, showing that this ratio follows $|F^{(2)}|^2/|F^{(1)}|^2$ reasonably well. This supports the correctness of the relative size of the circular and linear scattering terms $F^{(1)}$ and $F^{(2)}$ as obtained here, and in turn the correctness of the Kramers-Kronig transformation of the linear dichroism.

It is worthwhile to point out that at the M_5 edge a 1 eV broad plateau around 1184.5 eV exists where the two scattering terms are of similar amplitude and their ratio more or less constant, while away from this plateau $F^{(2)}$ is negligible. This gives the possibility to switch the linear magnetic scattering term on or off by changing the energy by only 1 eV. The latter can also be achieved by tuning to the Fe $L_{2,3}$ edge where magnetic linear dichroism is absent.

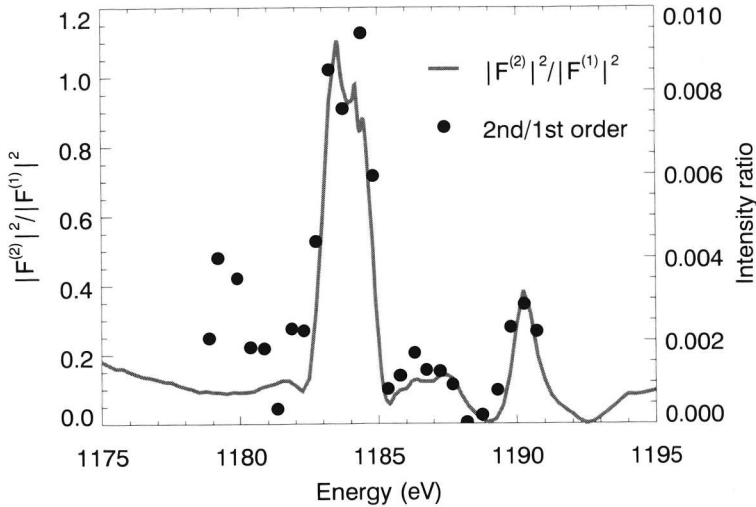


Figure 4.8: Full curve/left axis: the ratio of $|F^{(2)}|^2/|F^{(1)}|^2$. Dots/right axis: Ratio of the intensities of the second to first order Bragg maxima as a function of photon energy.

4.5 Conclusions

We have measured the polarization and spin dependent transmission spectra of thin $Gd_{1-x}Fe_x$ layers at the Gd $M_{4,5}$ and Fe $L_{2,3}$ absorption edges. Quantitative values for the atomic cross sections for x-ray absorption and magnetic circular- and linear dichroism were obtained. The values for the atomic absorption and dichroism cross sections found at the Gd $M_{4,5}$ edge are the same to within 2% for samples of different composition and thickness, showing that the experimental method is consistent and exemplifying the quality of the data. The local nature of the Gd 4f shell involved in this $3d \rightarrow 4f$ transition makes these spectra insensitive to the chemical surrounding and these scattering amplitudes are therefore of use for all Gd compounds.

The absorption cross sections form the imaginary part of the resonant scattering amplitude. The corresponding real part was calculated using the disper-

sion relations. We found that at the Gd $M_{4,5}$ the maximum resonant scattering amplitude is a factor 10 higher than the non-resonant Thomson scattering length, which is likely to be the largest resonant enhancements that can be found [11, 74, 94, 95]. The circular dichroism is huge, ca. 90% of the maximum resonant charge contrast and there is considerable linear dichroism, ca 30 % of the resonant enhancement. We have argued that the totally different energy dependence of the latter can be used to toggle the linear magnetic scattering contrast on and off at this edge.

The Fe resonant atomic scattering lengths are about a factor 10 lower in amplitude with a circular dichroism of 50 %. Linear dichroism could not be observed, simplifying the interpretation of scattering data considerably. Although the atomic scattering amplitudes are lower, the total amplitude for Fe $L_{2,3}$ can be comparable to that for Gd $M_{4,5}$ for Fe rich compositions.

A comparison of the circular magnetic scattering cross sections with the total scattered intensity from a magnetic stripe lattice normalized by the total transmitted intensity demonstrated that the scattering contrast is of a purely magnetic origin. We presented an analysis of this scattering data in terms of a space-modulated refractive index, showing that the scattered intensity can be written as the product of an average isotropic attenuation factor and an anisotropic magnetic scattering contrast. Although explicitly derived for the case of circular polarization it is easy to show that the same expression also holds for linear polarization. In that case the scattering contrast does not arise from a modulation in phase and amplitude, but from a difference in Faraday rotation and ellipticity is obtained for up- or down magnetized domains.

MAGNETIC RESONANT SCATTERING IN THE SMALL-ANGLE LIMIT

5.1 Introduction

In this chapter we describe the resonant magnetic scattering produced by a remanent quasi-periodic magnetic stripe system, in zero applied field. We discuss the phenomenology of the diffraction patterns taken at the Gd rare-earth $M_{4,5}$ and Fe transition metal $L_{2,3}$ edges using the atomic scattering description, now showing in detail how the polarization- and energy-dependence of the scattered intensities in combination with the measured optical constants from Chapter 4 are used to interpret the results. This understanding is used to formulate a theoretical description in terms of the forward scattering form of the resonant scattering cross section, and to separate the vector components of the three-dimensional magnetic structure. Finally we discuss the scattered intensity in terms of the conventional small-angle x-ray scattering form- and structure factors, which offers a natural explanation of the observed diffraction patterns including circular dichroic effects.

5.2 Beamline and setup

A typical small-angle scattering transmission geometry is sketched in Fig. 5.1. It was found that the conventional detector to monitor the incident intensity I_0 produced strong small-angle scattering and had to be moved out of the beam. Instead, the I_0 intensity was monitored by reading the drain current from the refocussing mirror. Scattered light from the beamline was blocked directly after the mirror by setting four blades as guards around the beam. 100 nm parylene or Al ultra-thin windows were used to separate the beamline vacuum of $\sim 10^{-9}$ mbar from the diffractometer vacuum of $\sim 10^{-7}$ mbar.

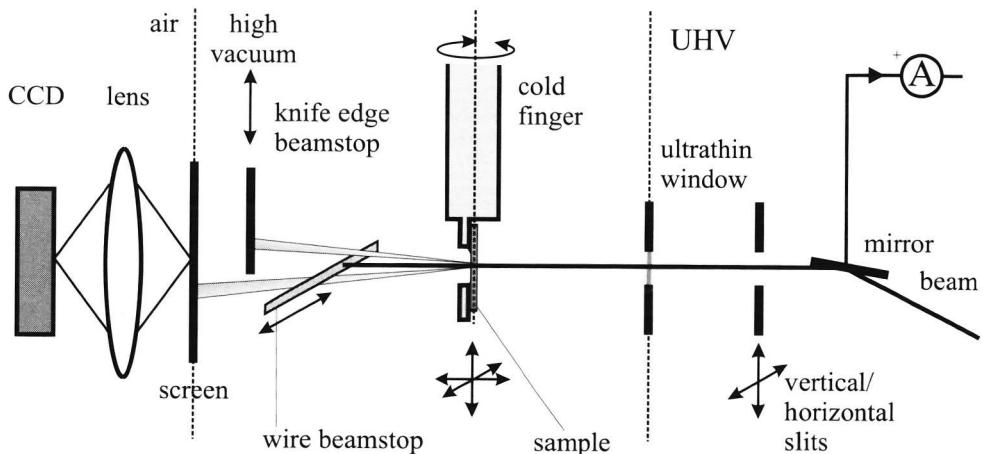


Figure 5.1: Experimental layout for the scattering experiments.

The sample, a 42 nm GdFe_5 thin film as described in Chapters 2 and 4, was positioned in the vertical focus of the last mirror and mounted onto a cold finger that could be rotated around its vertical axis using a differentially pumped rotatable feedthrough. The temperature could be varied between 20 and 350 K. The sample chamber was equipped with an in-vacuum 0.5 T magnet with its field direction parallel to the beam in the horizontal plane.

Small-angle scattering experiments are best performed with a 2-D detector. For soft x-rays back-thinned direct exposure CCD systems do exist, which give optimum sensitivity, but they are expensive, easily damaged by the direct beam, and have a relatively poor dynamic range. We used a simple system consisting

of a phosphor-coated vacuum window with a 12 bit CCD camera fitted with appropriate optics. The phosphor screens were made by sedimenting a 5 μm layer of powder of 1 μm grain size on glass windows. Two different phosphors were used, P43 and P20, where the latter had the best yield.

For the present experiments a TV lens combined with a 5 mm macro-ring was used, giving a field of view of ~ 15 mm and a 10 μm resolution. The detector to sample distance was varied between 300 to 450 mm. Beam stops were either a horizontal 1 mm Cu wire or a knife edge, mounted on motorized linear drives.

The advantages of this detector are a high dynamic range, sturdiness and flexibility: by changing the magnification of the optics one can readily trade \mathbf{q} -resolution with \mathbf{q} -range. Among the weak points of this detector is its low efficiency ~ 1.5 % counts/photon for P20 at the Gd edge and 2 % at the Fe edge. Also, multiple reflections in the glass window produce an artefact ring with a radius of 3 mm and an integrated intensity of ca. 1 %. As a result, for measurements of the low intensity features in the diffraction pattern, high intensity features have to be blocked out by a beam stop. In practice, it means that typically three exposures with different knife edge positions have to be taken in order to cover the 5 orders of intensity in the diffraction pattern.

5.3 Data integration and fitting

The top panels in Fig. 5.2 show typical examples of disordered and aligned stripe lattices as imaged by MFM. The middle panels of Fig. 5.2 show the corresponding diffraction patterns. For the disordered stripes the pattern consists of series of concentric rings, the first of which is visible here. Upon ordering the stripes with a magnetic field, the intensity concentrates in opposite points on these circles, as shown on the right. The most general data treatment therefore consists of performing angular and radial integrations. To this end, the data are converted to polar coordinates $(q_{//}, \gamma)$, where $q_{//}$ is the in-plane momentum transfer and γ is the azimuthal scattering angle, as shown in the bottom panels of Fig 5.2.

The radial integration of the diffraction patterns yields the *angular intensity distribution* $I(\gamma)$ that contains information on the degree of order in the stripe lattice. For disordered stripes, with a random orientation of stripe direction, this is

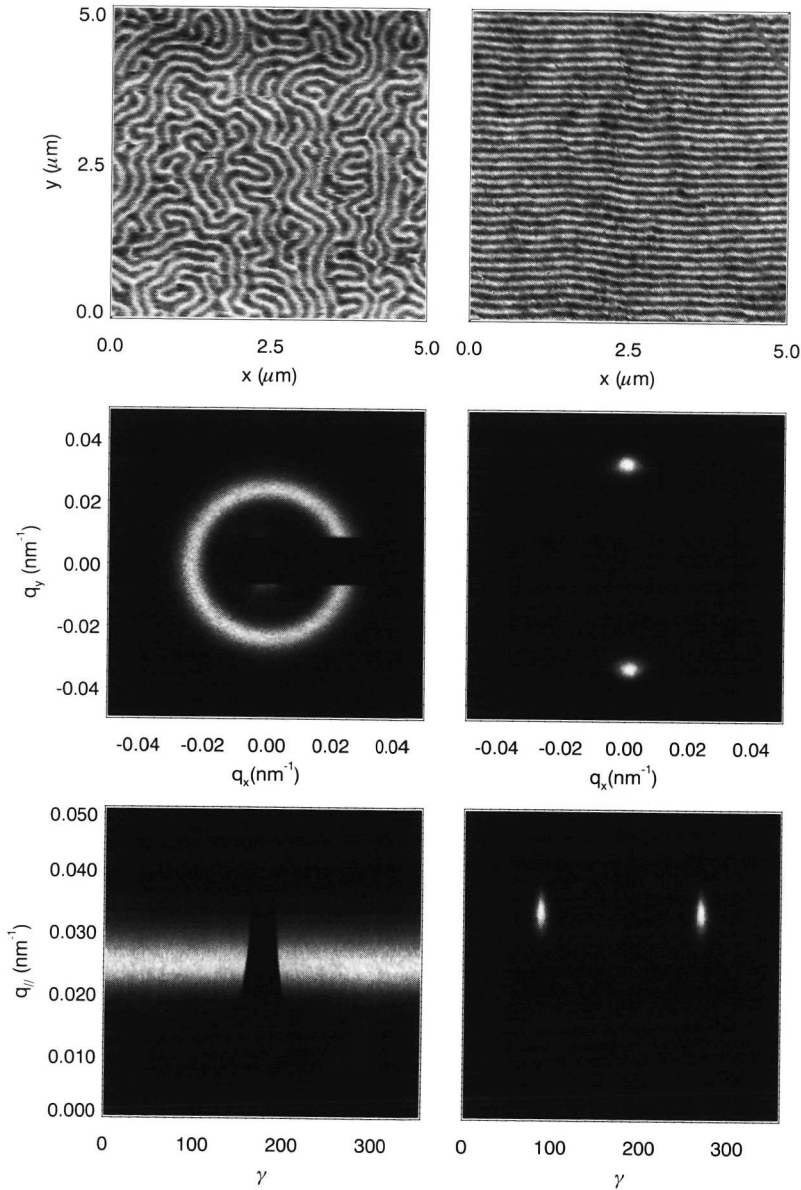


Figure 5.2: Scattered intensity for disordered (left) and aligned (right) stripes. From top to bottom: magnetic force microscopy image, scattered intensity on the 2-D detector, same plotted in 2-D polar coordinates.

clearly a flat distribution, while for aligned stripes it is sharply peaked around $\gamma = 90^\circ$ and $\gamma = 270^\circ$.

Integration over the angular coordinate gives the intensity distribution $I(q_{//})$ as a function of the in-plane momentum transfer $q_{//}$. A typical example, obtained from different exposures is shown in Fig. 5.3. We found that the best fit to these curves could be made using a squared Lorentzian line shape:

$$\left(\frac{w}{w^2 + q_{//}^2}\right)^2 \quad (5.1)$$

where the width w scales linearly with the diffraction order. The exact origin of the line shape is still unclear. However, due to disorder the correlation of the periodic structure is finite, which explains the broadening of the peaks [96]. Deviations of the fit from the data at either side of the first order are due to an imperfect merge between data of different exposure, intensity of the artefact arising from high intensity features and deformations due to the imaging optics.

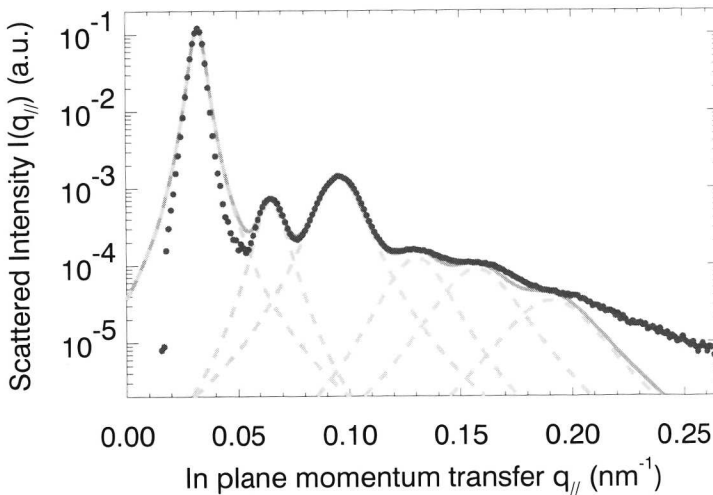


Figure 5.3: Example of azimuthally integrated diffraction patterns of remanent stripe domains. Full curve: result of fit with squared Lorentzian line shapes (dashed lines).

5.4 Phenomenology of stripe diffraction patterns

5.4.1 Linear polarization

Fig. 5.4 shows the integrated intensity as function of the in-plane momentum transfer $q_{//}$ for a horizontally aligned stripe system taken at normal incidence with the polarization vector either horizontal (x) or vertical (y), *i.e.* parallel or perpendicular to the stripe direction. The upper curves, taken at the Gd M_5 resonance ($\hbar\omega = 1185$ eV), show eight maxima with intensities ranging over more than 5 orders of magnitude, and are the result of four different exposures, with exposure time varying from 0.15 to 1000 s. The lower curves, taken at the Fe L_3 resonance ($\hbar\omega = 707$ eV), were taken using 2 exposures of 10 and 1000 s.

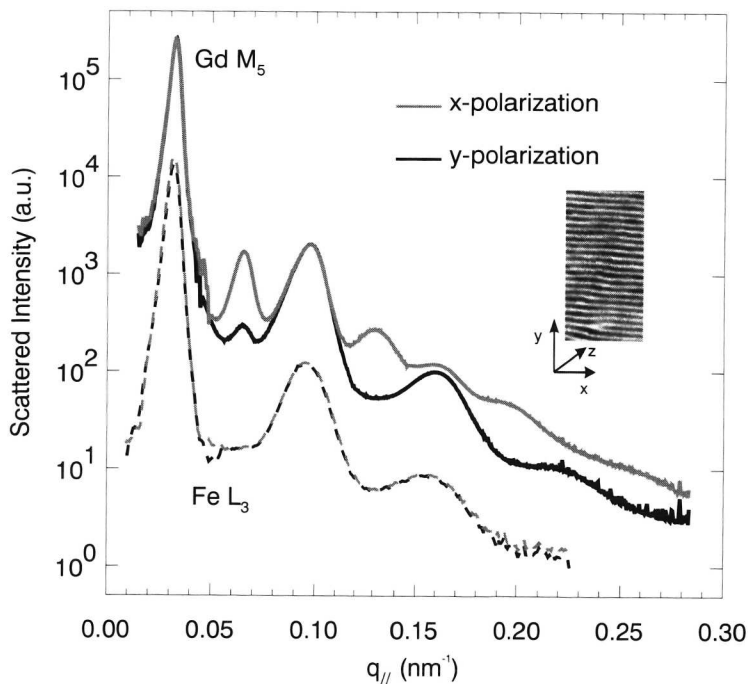


Figure 5.4: Angular integrated scattered intensity from remanent stripe domains, taken with x- and y-polarized beams. Top curves: Gd M_5 . Bottom curves: Fe L_3 edge.

At the Fe L_3 edge, both polarizations produce identical diffraction curves consisting of a series of odd order intensity maxima. In comparison, the curves taken at the Gd resonance show a much more complicated behavior: Again the odd order maxima are insensitive to the polarization. However, the x -polarized curve shows a full set of even harmonics, while the y -polarized curve only shows a weak second order and no higher even orders.

5.4.2 Circular polarization

Fig. 5.5 (top) shows the intensity of the first 5 orders as obtained with left- and right-circularly polarized light. Here a second order is present, with an intensity in between that of the x - and y - polarized cases. The fourth order peak may be present but is merged with the fifth order. Clearly, there is no difference between the two helicities. This situation is changed drastically by applying a 5 mT field perpendicular to the film, as shown in the bottom graph of Fig. 5.5. Now both even orders show a strong, helicity dependent, asymmetry.

5.4.3 Non-normal incidence

Apart from the energy and the polarization one may also change the scattering geometry. A simple experiment is to vary the angle of incidence in the xz -plane, but still detect the scattered intensity in transmission. Fig. 5.6 shows the second and third order diffraction maxima from the aligned stripes for incidence angles of 0° , 30° and 45° with respect to the sample normal. The light was polarized along x and the energy was tuned to the Fe L_3 edge, where the second order is absent at normal incidence. For the incidence angles away from the sample normal a second order appears that increases with the angle.

5.5 Interpretation of the stripe diffraction patterns in the small-angle limit

The aligned stripe domain structure as imaged with MFM forms a quasi-1-dimensional periodic lattice, which in order to interpret our results, we will treat initially as a perfect lattice with translational symmetry. In Fig. 5.7 we have drawn such a 1-D stripe structure with out-of-plane domains m_z sepa-

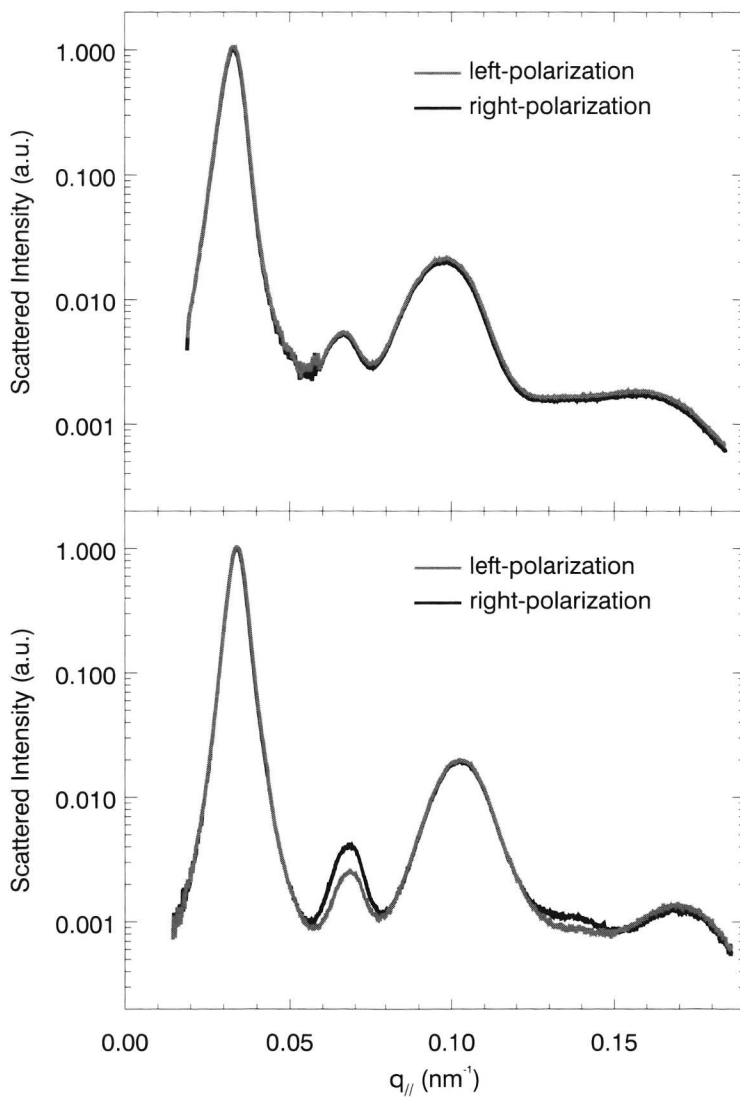


Figure 5.5: Resonant diffraction pattern from aligned stripe domains after saturation with an in-plane field for left (black curve) and right (grey curve) circularly polarized light. Bottom: Same as top with a 50 Oe field applied normally to the surface.

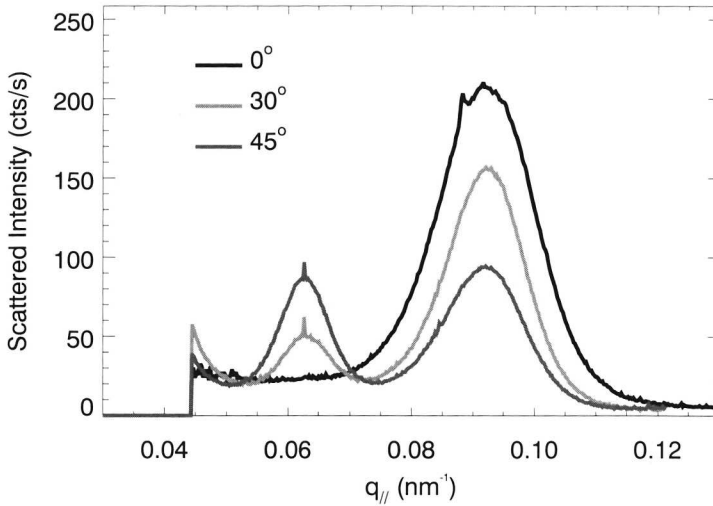


Figure 5.6: Scattered intensity for the second and third order maxima from a remanent aligned stripe structure as a function of the incidence angle. The energy was tuned to 707 eV and the light was incident in the xz -plane.

rated by Bloch walls, m_x , and including closure domains m_y in the top and bottom of the film. We will assume that all atoms have the same moment so that $\sum_i m_i^2 = 1$ everywhere in the sample and the coordinate axes are chosen such that the structure is independent of x and periodic in y .

Bragg's law states that the sine of the scattering angle is proportional to the ratio of the wavelength λ and the length scale that is probed. The typical sizes of magnetic domains are measured in tens of nanometer, while the soft x-ray wavelength is ~ 1 nm. This implies that the scattering angles are a few degrees at most, and we can apply the small-angle approximation.

In this approximation we can use the refractive index formalism of section 4.4 to obtain an intuitive understanding of the propagation of the incident plane wave through the film, where each ray sees either an up- or down-domain or a domain wall. Each ray therefore obtains a phase lag, absorption and change in polarization, corresponding to the y -coordinate. However, the magnetization

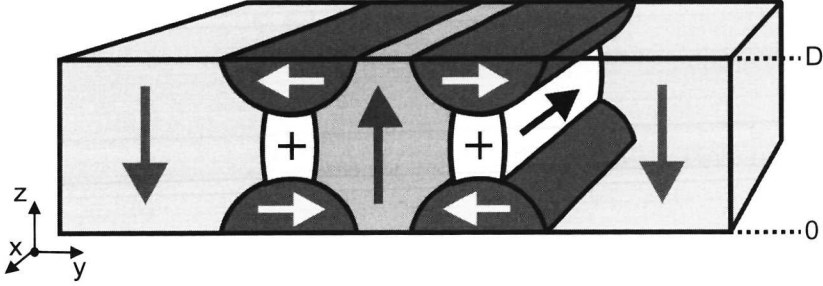


Figure 5.7: Schematic representation of the magnetization distribution in a stripe domain, showing out-of-plane stripes ($\uparrow\downarrow$), separated by Bloch walls ($+$) and closure domains (\rightarrow, \leftarrow).

vector \mathbf{m} changes continuously, and so do the solution of the wave equation and the corresponding polarization modes and refractive indices. The transmitted field can still be described exactly, but this requires elaborate beam propagation methods. We therefore fall back to the single scattering description as introduced in section 3.3.3, which is allowed if the modulation in phase and amplitude of the propagated wave is small compared to its average phase and amplitude.

We start with the resonant scattering tensor $\mathbf{f}(\mathbf{r}, \mathbf{m})$ as defined by (3.37) and (3.46) for the case of normal incidence. For the \mathbf{q} range of interest the scattering angles are small and the scattering tensor \mathbf{f} can be approximated by that for forward scattering $\mathbf{k}' = \mathbf{k}/\hat{z}$. Choosing as the polarization basis $\lambda = \lambda' = \{x, y\}$ the scattering tensor in matrix form is given by (3.47):

$$\mathbf{f}(\mathbf{r}) = \begin{pmatrix} 1 & 0 \\ 0 & 1 \end{pmatrix} (f^0 + F^{(0)}) + \begin{pmatrix} 0 & -im_z(\mathbf{r}) \\ im_z(\mathbf{r}) & 0 \end{pmatrix} F^{(1)} + \begin{pmatrix} m_x^2(\mathbf{r}) & m_x(\mathbf{r})m_y(\mathbf{r}) \\ m_x(\mathbf{r})m_y(\mathbf{r}) & m_y^2(\mathbf{r}) \end{pmatrix} F^{(2)}. \quad (5.2)$$

The matrix elements give the probability of scattering the component E_0^λ into $E_s^{\lambda'}$. Since the film and substrate are flat within 1 nm and hence do not have any noticeable *charge* structure, the first, magnetization independent, term will only contribute to the overall helicity averaged attenuation of the signal via absorption as discussed in Chapter 4. The second term, proportional to $F^{(1)}$, contains the up-down modulated magnetization m_z . The last term, proportional to $F^{(2)}$,

contains the in-plane magnetization components m_x and m_y that represent the domain walls and closure domains, respectively.

As discussed in Chapter 3 the far-field scattered intensity is the absolute squared Fourier transform of the atomic density ρ_a of the scattering atomic species times its scattering amplitude (see (3.45)). Since the structure is assumed to be invariant in the x direction, the Fourier integral over the x coordinate yields a $\delta(q_x)$, implying that there is no scattering in the x direction. Furthermore, for the small scattering angles involved, $q_z = 0$ and the Fourier integral over the z coordinate reverts to a simple integral of the scattering cross section over the film thickness d and the scattered field is dependent on q_y only. Introducing the equivalent contrast functions $g_i = \int_0^D m_i(y, z) dz$, and $g_{ij} = \int_0^D m_i(y, z) m_j(y, z) dz$ we may write

$$\begin{aligned} \mathbf{E}_s(q_y) = \rho_a \delta(q_x) \int_{-\infty}^{\infty} dy & \left[\begin{pmatrix} 0 & -ig_z(y) \\ ig_z(y) & 0 \end{pmatrix} F^{(1)} + \right. \\ & \left. \begin{pmatrix} g_{xx}(y) & g_{xy}(y) \\ g_{yx}(y) & g_{yy}(y) \end{pmatrix} F^{(2)} \right] \mathbf{E}_0 e^{-iq_y y} \end{aligned} \quad (5.3)$$

where we have omitted a factor $-r_0/R$. This expression can be simplified somewhat by using a symmetry argument: If closure domains are present, their magnetization $m_y(z)$ is anti-symmetric in z with respect to the xy -plane at $z = 1/2D$, where D is the film thickness, whereas $m_x(z)$ is symmetric hence $m_x(z)m_y(z) = -m_x(D-z)m_y(D-z)$. Thus $g_{xy}(y) = \int_0^D m_x(y, z)m_y(y, z) dz = 0$ for all y . It then follows that

$$\begin{aligned} \mathbf{E}_s(q_y) &= \rho_a \left[\begin{pmatrix} 0 & G_z(q_y) \\ -G_z(q_y) & 0 \end{pmatrix} F^{(1)} + \begin{pmatrix} G_{xx}(q_y) & 0 \\ 0 & G_{yy}(q_y) \end{pmatrix} F^{(2)} \right] \mathbf{E}_0 \\ &= \mathbf{F} \mathbf{E}_0 \end{aligned} \quad (5.4)$$

where $G_z(q_y)$, $G_{xx}(q_y)$ and $G_{yy}(q_y)$ are the Fourier transforms of g_z , g_{xx} and g_{yy} . In Table 5.1 the scattered intensity $I(q_y)$ is explicitly written out for linearly or circularly polarized incident light. It shows that the Fourier transform of the stripe magnetization, m_z , appears with the same amplitude for all polarizations. The difference in intensity between x and y polarization is now seen to be due to the $F^{(2)}$ contrast: x -polarized incident light scatters from the m_x magnetization in the Bloch walls, and y -polarized light scatters only from the m_y magnetization in the closure domains.

Table 5.1: Intensity for x -, y -, or circular polarization in the forward scattering approximation.

Polarization vector	Scattered Intensity
\hat{x}	$ F^{(1)}G_z ^2 + F^{(2)}G_{xx} ^2$
\hat{y}	$ F^{(1)}G_z ^2 + F^{(2)}G_{yy} ^2$
$\frac{1}{\sqrt{2}}(\hat{x} \pm i\hat{y})$	$ F^{(1)}G_z ^2 + \frac{1}{2}(F^{(2)}G_{xx} ^2 + F^{(2)}G_{yy} ^2)$ $\pm \text{Re}[(F^{(1)}G_z)^* F^{(2)}(G_{xx} + G_{yy})]$

The interpretation of the data in Fig. 5.4 is now straightforward: The odd orders are due to the up-down m_z magnetization, and are independent of the state of polarization at both edges. At the Gd M_5 -edge the even orders observed with x -polarized light are caused by the structure of the domain walls, m_x , and the second order observed with y -polarized light is coming from the closure domains, m_y . The absence of these even orders at the Fe L_3 edge is due to the much lower linear magnetic scattering amplitude $F^{(2)} \ll F^{(1)}$ at this resonance.

The different origin of the odd and even diffraction orders can be proven in an elegant way by considering the energy dependence of the diffracted intensities. We find that the ratios of the higher order odd- to first order intensities stay strictly the same over the edge, while the even order to first order intensity ratios vary strongly over the Gd M_5 edge. In order to quantify this behavior the first four diffraction maxima of the x -polarized curves were fitted with squared Lorentzian line shapes using the procedure described in section 5.3. To correct for the average attenuation of the film and substrate, these intensities were normalized to the energy-dependent total transmission of the sample, see eq. (4.12). The results are shown in fig. 5.8, together with the $|F^{(1)}|^2$ and $|F^{(2)}|^2$ curves obtained from the absorption measurements as described in Chapter 4. In this figure all curves have been peak-normalized in order to bring out the salient point: the first and third order intensities almost perfectly match the spectrum of $|F^{(1)}|^2$, while the second and fourth order intensities follow somewhat less precisely the spectrum of $|F^{(2)}|^2$. We ascribe the deviations to imperfections in the fitting procedure due to which the out-of-plane odd order scattering is not completely subtracted.

We conclude that the diffraction pattern of the aligned stripes in remanence consists of a series of odd order peaks due to $F^{(1)}$ scattering by the out-of-plane

magnetic structure and even order peaks that originate from $F^{(2)}$ scatter by in-plane magnetization components, either Bloch walls or closure domains.

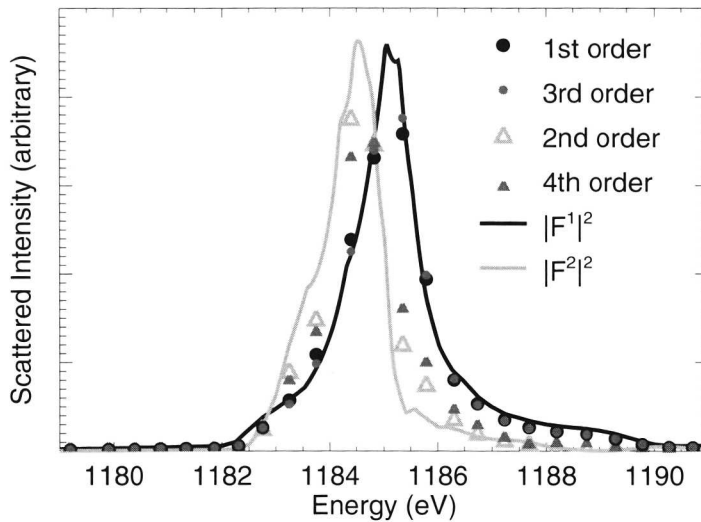


Figure 5.8: Normalized intensity for odd (dots) and even (triangles) orders as a function of the x-ray energy. Solid lines: energy dependence of the circular, $|F^{(1)}|^2$, and linear magnetic scattering terms, $|F^{(2)}|^2$.

For circular polarized light, Table 5.1 shows that the scattered intensity is the average of the linearly polarized intensities *plus* an interference term between out-of-plane and in-plane scattering contributions. The sign of this interference term is helicity dependent and therefore can lead to a circular asymmetry in the scattered intensity. Figure 5.5 showed that one has to apply a finite magnetic field for this to happen. We will explain this, and the related occurrence of forbidden reflections, by describing the scattered intensities in terms of a single domain form factor and the structure factor describing the periodicity of the lattice.

5.5.1 The form factor of a single reverse domain

Since small-angle x-ray scattering is generally used to study the structure of a collection of identical objects, it is customary to write the scattered intensity as the product of a squared form factor $\mathcal{F}(q)$, which is the Fourier transform of the shape of the individual entity, and a structure factor $S(q)$, which is a sum over the coordinate positions of all objects: $I(q) = \mathcal{F}(q)^2 S(q) I_0$ (see e.g. [76, 97]), with I_0 the incident intensity. For a single object $I(q) = \mathcal{F}(q)^2 I_0$.

First we consider the diffraction of a single 'reverse' domain consisting of a region of 'up' magnetization in a *sea* of 'down' magnetization or *vice versa*. This reverse domain is dressed with Bloch walls, and possibly closure domains as drawn in Fig. 5.7. Example contrast functions for this structure are drawn in the Fig. 5.9-A and -B. The contrast function $g_z(y)$ of the 'up' domain of width W is close to that of a slit with diffuse borders, and hence its Fourier transform gives a Airy-like diffraction pattern as depicted in Fig. 5.9, panel C. The contrast function for Bloch walls g_{xx} and, if present, closure domains g_{yy} , consist of two peaks centered at $\pm 1/2W$ (panel B) and its Fourier transform is given in panel D.

Taking into account the tensor nature of the magnetic scattering the intensity scattered by this object is

$$I(q) = |\mathbf{F}(q_y) \hat{\mathbf{e}}_0|^2 I_0, \quad (5.5)$$

where $\mathbf{F}(q_y)$ is the scattering tensor as defined by 5.4, for the Fourier transforms $G_z(y)$, $G_{xx}(y)$ and $G_{yy}(y)$ of the single domain and $\hat{\mathbf{e}}_0$ is the polarization vector of the incident wave. As an illustration we show in panel E the single domain intensities I_x , I_+ and I_- for linearly and circularly polarized light using the optical constants at 1184 eV. The interference term in I_{\pm} , produces an asymmetry in the scattered intensity $(I_+ - I_-)/(I_+ + I_-)$, which as shown in panel F, varies stronger around integer-even values of $q_y W/\pi$.

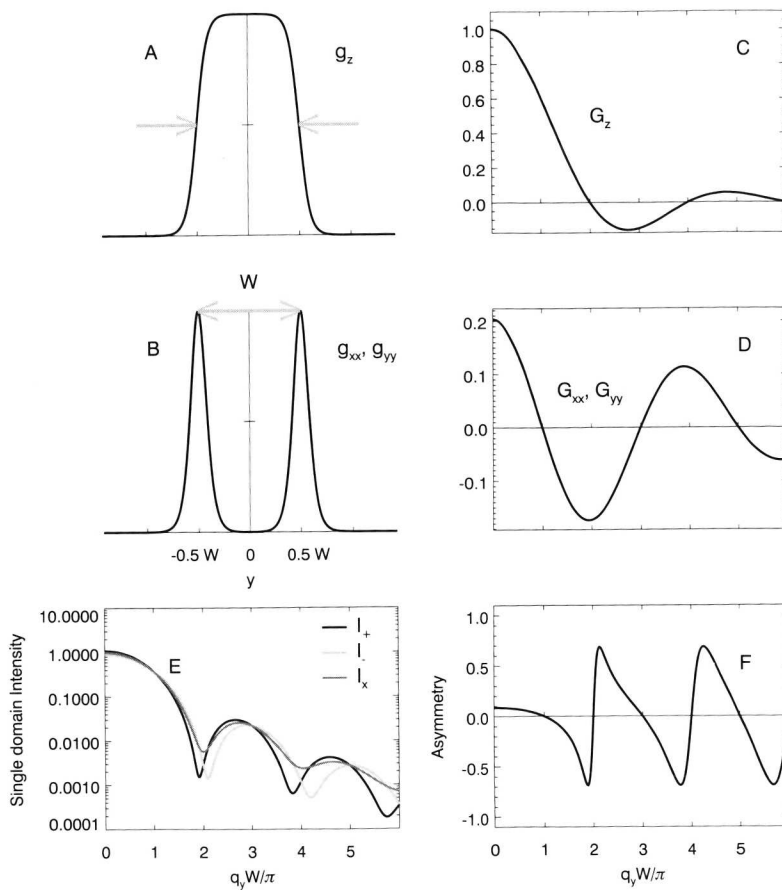


Figure 5.9: Generic real space scattering contrast functions for a single up domain (A) and its in-plane Bloch or closure magnetization (C) and their Fourier transforms (B) and (D). Corresponding single domain intensities for circular and linear polarized light at 1184 eV are shown in (E) and the asymmetry $\frac{I_+ - I_-}{I_+ + I_-}$ in (F).

5.5.2 Structure factor

The far-field diffracted intensity by an ensemble of N reverse domains at positions y_l can now be written as

$$I(q_y) \propto I_0 \sum_{k,l=1}^N \hat{\mathbf{e}}_0^* \mathbf{F}_k^*(q_y) \mathbf{F}_l(q_y) \hat{\mathbf{e}}_0 e^{iq_y(y_k - y_l)}. \quad (5.6)$$

If all domains are identical in shape, $\mathbf{F}_k = \mathbf{F}_l$, this can be written as

$$I^A(q_y) \propto |\mathbf{F}(q_y) \hat{\mathbf{e}}_0|^2 S(q_y),$$

where $S(q_y) = \sum_{k,l=1}^N e^{iq_y(y_k - y_l)}$ is the so-called structure factor. In the limit of large N and for a perfect periodic lattice of period P it is easily derived that

$$S(q_y) = N\tau \sum_{n=-\infty}^{\infty} \delta(q_y + n\tau), \quad (5.7)$$

where $\tau = 2\pi/P$ is the inverse period. In this case the structure factor samples the form factors at integer values of τ .

For the specific case of a remanent sample after in-plane saturation we have the particular situation that up and down domains are of equal width and $\tau = \pi/W$. This explains directly the absence of even orders at the Fe L_3 diffraction pattern in Fig. 5.4 which is purely $F^{(1)}$: from Fig. 5.9 we see that G_z has zeros at even values of $q_y W/\pi = q_y/\tau$. Similarly G_{xx} and G_{yy} have zeros at odd values of $q_y W/\pi = q_y/\tau$, and the $F^{(2)}$ term gives even order diffraction maxima only.

On the other hand, if some field is applied in the out-of-plane direction, the 'reverse' domains that have their magnetization opposed to the field direction (see Fig. 5.7) shrink with respect to the domains that have their magnetization along the field direction. The width of the reverse domains W becomes smaller than $P/2$. As a result the zeros of the functions $G(q_y)$ no longer coincide with the peak positions $n\tau = 2n\pi/P$ of the structure factor. The even order peaks obtain some amplitude from $F^{(1)}G_z$ and the odd orders from $F^{(2)}G_{xx}$, $F^{(2)}G_{yy}$. For circular polarized light the $F^{(1)}$ and $F^{(2)}$ terms interfere as given by table 5.1, producing helicity-dependent scattering as shown in Fig. 5.9-E. The resulting asymmetry (Fig. 5.9-F) can be quite large around even values of $q_y W/\pi$ but stays much smaller around odd values. This explains the dichroism observed

on the even order peaks for very small out-of-plane fields (Fig. 5.5). It might be mentioned here that for very high perpendicular fields the long range order between the reverse domains is lost completely and the scattered intensity obtains shapes as shown in Fig. 5.9-E [98].

Note that in the discussion of the single domain form factor we have left open whether the Bloch walls on either side of the domain have parallel or anti-parallel magnetization, since g_{xx} involves m_x^2 . However, the non-normal incidence data of Fig. 5.6 give information on this point. For light incident in the xz -plane but with a finite angle θ with respect to the z -axis the off-diagonal elements for the $F^{(1)}$ term in equation (5.2) become proportional to $\cos(\theta)m_z + \sin(\theta)m_x$. The m_z term still gives odd order diffraction maxima, but with an intensity falling off as $\cos^2(\theta)$. Anti-parallel domain walls would produce a contrast function $g_x(y)$ with the same period as $m_z(y)$ and would produce odd diffraction orders with intensity $\propto \sin^2(\theta)$. The fact that even orders appear proves that the majority of Bloch wall are parallel, since in that case $m_x(y)$ has half the period of $m_z(y)$. Grazing incidence x-ray microscopy indeed allows one to distinguish the magnetization in individual domain walls [99], albeit with a much lower spatial resolution than in our case.

5.6 Conclusions

In this chapter we have presented resonant magnetic small-angle scattering from remanent aligned stripes which showed a strong dependence on the energy and polarization state of the incident x rays. We have explained the strikingly different results at the Gd M_5 and Fe L_3 edges on a basis of single scattering theory and in the limit of forward scattering. A separation of the scattering properties of a single domain and the stripe lattice, introducing form and structure factor, qualitatively explains the occurrence of forbidden reflections and asymmetries occurring for samples with a net out-of-plane magnetic moment. In the latter case the observed beating in the scattered intensity for the two helicities is a sensitive measure of the stripe width [98]. This analysis forms a framework for the interpretation of the field dependent diffraction data in the next chapter.

We have demonstrated that at the Gd M_5 edge it is possible to separate the

scattering from the three components of the magnetization in an aligned stripe domain system. This could be done for the specific case where the period of the stripes is exactly twice the stripe width: then the odd order maxima are exclusively due to the out-of plane bulk magnetic contrast function times $|F^{(1)}|^2$ and the even orders are due to structure of the in-plane magnetization components times the linear magnetic scattering cross section, $|F^{(2)}|^2$. Incident polarization parallel to the stripe direction illuminates the Bloch walls, while perpendicular polarization brings out the much weaker contribution from closure domains.

From (5.3) it follows that for linear polarized light the out-of-plane (in-plane) contrast is diagonal (off-diagonal). A polarization analysis of the scattered light, using e.g. a multilayer mirror would enable a complete separation of the three scattering terms, even for up- and down domains of unequal width. This should be considered for future experiments.

In principle, by illuminating the object from different angles, the complete 3-D vectorial magnetic structure can be extracted. However a detailed analysis is extremely difficult due to the complicated absorptive and refractive effects as the rays traverse the medium. Especially for the treatment of reflection data a full dynamic theory seems necessary [100] and a 3-D -characterization of the stripe structure becomes a daunting task. A first step was taken by changing the angle of incidence and it could be proven that at remanence, after in-plane magnetization the Bloch walls in the bulk of the film have a parallel alignment.

It should be stressed that so far we have assumed a perfect lattice in our analysis. However, the aligned stripe system is quasi-periodic and does not have long-range order. For the similar case of a periodic multilayer Fullerton *et al.* [96] have shown that the scattered intensity can be analyzed in terms of a fluctuating object size. This analysis explains the broadening of higher order satellites as observed here, but also shows that the relative intensities of the diffraction maxima are altered by the disorder. A full treatment along these lines may be useful but falls out of the scope of thesis.

EVOLUTION OF STRIPE DOMAINS IN IN-PLANE MAGNETIC FIELDS

In this chapter we extend the qualitative description of the features found in polarization dependent scattering from a stripe lattice at remanence and follow the evolution of such a stripe lattice over the magnetization loop for in-plane applied fields. We will discuss measurements at 20 K and room temperature for two different samples: a 42 nm GdFe₅ film and 44 nm GdFe₉ film. We observe the nucleation of a weak and largely disordered out-of-plane oscillation close to the in-plane saturation field. Upon decreasing the field the amplitude of the out-of-plane oscillation increases and a well ordered aligned stripe state develops. From the diffraction data the lateral structure of these magnetic vector components can be reconstructed in great detail. We will discuss the differences between the two samples in terms of their macroscopic magnetic properties such as the anisotropy factor Q and the exchange constant A , determined from the nucleation field and period using the stripe nucleation theory presented in Chapter 2.

6.1 Macroscopic magnetization loops

The GdFe₅ and GdFe₉ thin films were grown on Si₃N₄ support windows and characterized by MOKE and MFM. Room-temperature MOKE magnetization

loops for in-plane applied field along the x -direction are shown in the top panels of Fig. 6.1. The vertical dashed lines indicate the coercive field H_c where $M_x = 0$ for the 'up'-branch of the hysteresis loops. Both curves show a large hysteresis between $\pm H_c$. Beyond H_c the magnetization gradually increases to the saturation value.

In order to get an estimation for the volume fractions V_{xx} and V_{yy} of the squared magnetization along the x - and y - direction, we also measured the field dependent x-ray transmission of the samples with the photon energy tuned such that the Gd M_5 edge linear dichroism was large. The volume fractions are defined as

$$V_{xx}(H) = \frac{1}{V} \int_V m_x^2(\mathbf{r}) d\mathbf{r} \cong \frac{1}{P} \int_0^P g_{xx}(y) dy \quad (6.1)$$

where g_{xx} are the 1-dimensional contrast functions as introduced in Chapter 5 Eq. 5.3. In an inhomogeneous magnetic film with a continuously varying magnetic vector the exact transmission can only be expressed in terms of a model dependent structure using beam propagation periods. However, in the approximation that these volume fractions are evenly distributed over the film the field-dependent transmitted intensity for x -polarized light can be written as

$$I_t(H) = I_0 e^{-(\mu_{\perp} + [\mu_{//} - \mu_{\perp}] V_{xx}) D}, \quad (6.2)$$

where $\mu_{//}$ and μ_{\perp} are the absorption coefficients for the magnetization vector parallel respectively perpendicular to the polarization vector. At saturation $V_{xx} = 1$ and we obtain the exact result that

$$I_t(H_s) = I_0 e^{-\mu_{//} D}. \quad (6.3)$$

Hence

$$\ln \frac{I_t(H)}{I_t(H_s)} = (1 - V_{xx})(\mu_{//} - \mu_{\perp}) D, \quad (6.4)$$

from which V_{xx} can be determined for a known linear dichroism $(\mu_{//} - \mu_{\perp}) D$. Similarly for y -polarized light V_{yy} can be obtained.

The fractions V_{xx} and V_{yy} corresponding to the room-temperature magnetization loops for the two samples are shown in the center panels of Fig. 6.1. Comparing with the MOKE loops we arrive at the important conclusion that at H_c where $M_x = 0$, V_{xx} can remain large. There are no reliable magnetization data of the samples at 20 K but we did measure V_{xx} and V_{yy} , see the bottom panels.

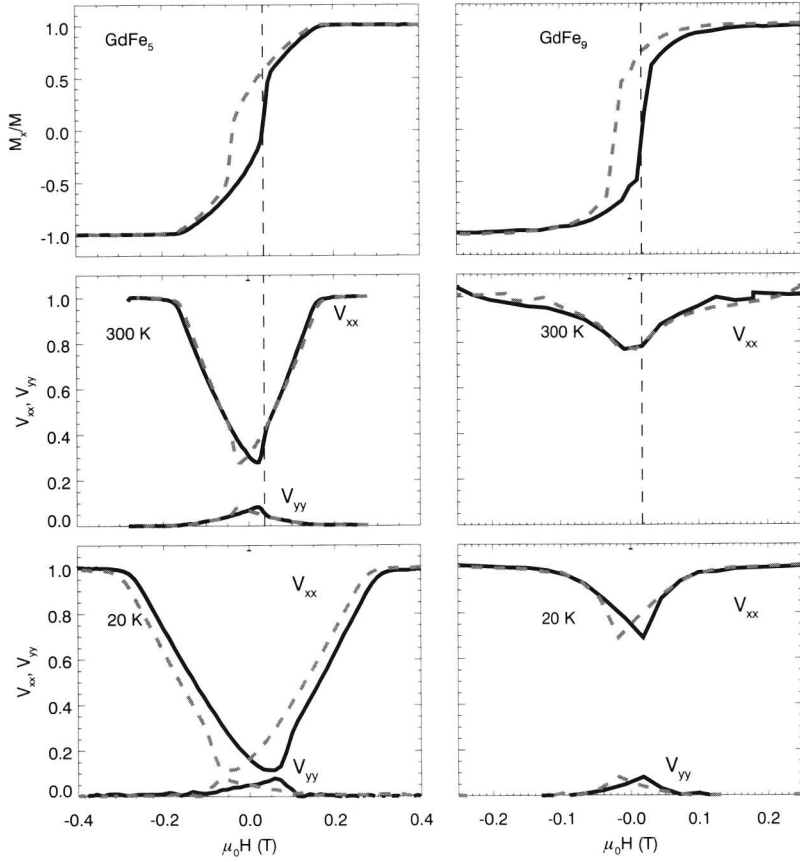


Figure 6.1: Room-temperature MOKE magnetization loops (top row) for and corresponding transmission linear dichroism curves (center row) for in-plane applied fields along the x -direction. Bottom row: transmission linear dichroism curves at 20 K. The full lines indicate the positive up-branch of the hysteresis curve, the broken lines the negative down-branch. The dashed vertical line marks H_c for the up-branch. Left: 42 nm GdFe_5 . Right: 44 nm GdFe_9 .

6.2 Field dependent diffraction data

Most data shown here were taken using a linearly polarized beam that was tuned to the Gd M_5 resonance at 1184 eV in order to obtain sensitivity to the in-plane magnetization components. The $GdFe_5$ sample was also studied at the Fe L_3 resonance ($\hbar\omega = 706.6$ eV). The magnetic field was along the x -direction and the x -ray beam was incident along the sample normal z . The data were integrated and fitted as described in section 5.3.

6.2.1 $GdFe_5$, overall behavior

A subset of the diffraction patterns taken along the in-plane magnetization loop for $GdFe_5$ at 20 K and room temperature are shown in Fig. 6.2. On the left axis the normalized intensities are given on a log scale. The curves are shifted vertically according to the applied field indicated along on the right axis. Due to the different saturation fields for the two temperatures the field scales are different. The data shown here are a combination of two CCD exposures to separately capture the first and higher orders giving rise to the discontinuities around $q_y = 0.06 \text{ nm}^{-1}$ in the room-temperature data.

The evolution of the diffracted intensity is followed from negative (top) to positive (bottom) saturation. First a single diffraction peak is observed. Upon decreasing the field its intensity rapidly increases and higher order maxima appear, while at the same time the peaks move to smaller q_y , implying that the period increases. Going through remanence and further raising the field the process reverses: the period starts to decrease again and the higher order maxima fade away until a single broad diffraction maximum is observed.

The data were fitted using the procedures discussed in the previous chapter and the results are summarized in Fig. 6.3. In the top panels the filled and open symbols denote the period for the up- respectively down branch of the magnetization loop. This shows that there is a large hysteresis in the period in the field range $|\mu_0 H_x| < \pm 0.25 \text{ T}$ ($|\mu_0 H_x| < \pm 0.12 \text{ T}$) at 20 K (300 K). We have indicated these fields in all panels by vertical lines and will refer to them as H_{hys} . The dashed lines indicate the position of H_c .

The second panels show the total scattered intensities normalized to the inci-

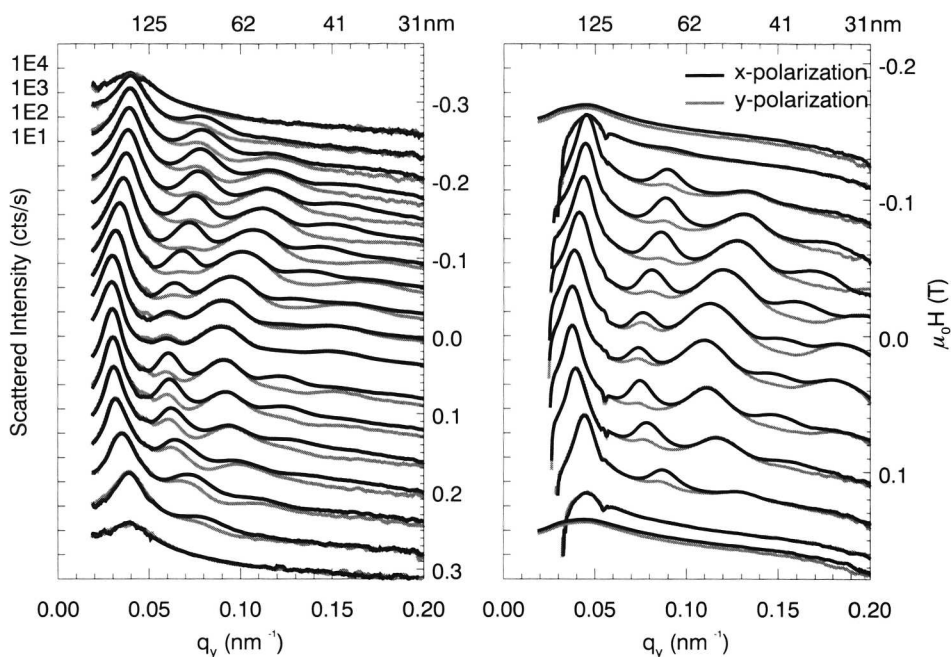


Figure 6.2: Evolution of parallel stripes in 40 nm GdFe₅ for a range of in-plane applied field at 20 K (left) and room temperature (right). Normal incidence diffraction with linear polarization vector along (black lines) or perpendicular (grey lines) to the field. The approximate field values belonging to the different curves are the intersection points of the curves with the right-hand axis.

dent intensity on absolute logarithmic scale (left axis, symbols) and an arbitrary linear scale (right axis, lines). At room-temperature the intensity is more than a factor 2 lower than at 20 K. The log scale curve reveals that the intensity is still gradually decaying where in the macroscopic magnetization data saturation seems reached. The filled respectively open symbols and the dark respectively light lines indicate the up- and down-branches of the hysteresis loop. Clearly there is hysteresis, but with a different field dependence than that of the period.

The third panels shows the full-width half maximum Δq of the radial first order peak normalized by its position τ . At high fields the peak shape is asymmetric leading to values of $\Delta q/\tau > 1$. Over the hysteretic region the radial peak width

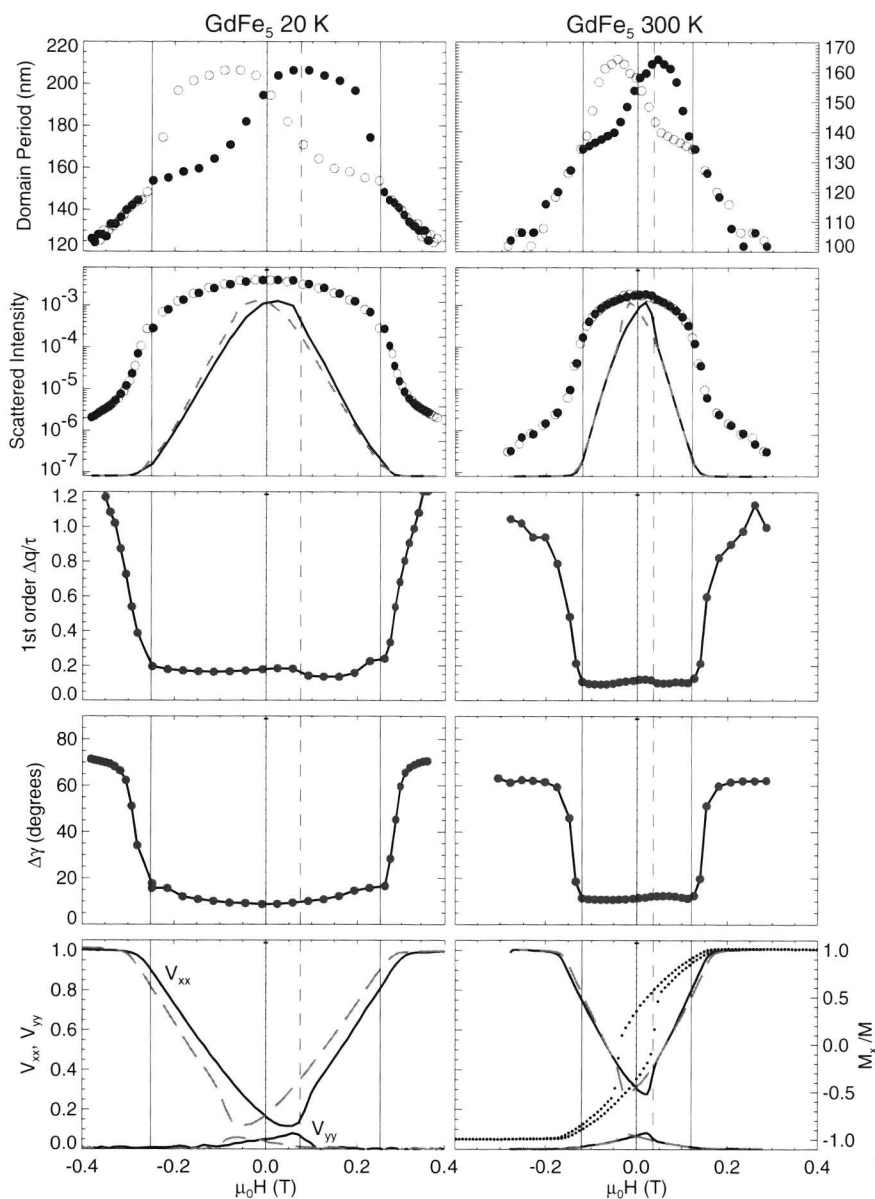


Figure 6.3: In-plane field dependence of the period, total intensity, relative radial peak width and angular peak width extracted from the diffraction data for 40 nm GdFe₅ at 20 K (left) and room-temperature (right). The filled respectively open symbols and the dark respectively broken lines indicate the up- and down-branches of the hysteresis loop. The bottom panel shows the total fractions V_{xx} and V_{yy} together with the longitudinal MOKE magnetization loop (small dots) for room temperature.

is nearly constant. Note however the small but distinctive reduction of the first order radial peak-width visible just beyond H_c .

The angular half width $\Delta\gamma$, is plotted in the fourth panels. The beamstop, blocking the central part of the diffraction pattern, limited the useful angular range to 75° at 20 K and to 65° at room temperature. Inspection of the 2-D CCD images shows that at high fields the diffraction pattern becomes a truly isotropic ring.

For comparison the macroscopic room-temperature MOKE and XMLD magnetization loops M_x/M , V_{xx} and V_{yy} of Fig. 6.1 are shown in the bottom panels.

6.2.2 GdFe₅: evolution of diffraction orders

The integrated intensities of the first six diffraction orders are shown in Figs. 6.4 and 6.5. The dot and square symbols are for x and y incident polarization respectively and the intensities have been normalized to the first order maximum for vertical polarization. Again the full vertical lines at ± 0.25 T (± 0.12 T) for the 20 K (300 K) data mark the hysteretic field region and the dashed lines indicate H_c . Overall, the 300 K data in Fig. 6.5 show similar behavior as the 20 K data in Fig. 6.4, but the effects are less pronounced. Also a sixth order could not be observed. We will concentrate our discussion therefore on the low temperature data.

The *odd*-order intensities as function of field form a single peak with a maximum between remanence and H_c . The third and fifth order are visible only between the hysteresis boundaries. The intensity of the third and fifth order relative to the first order intensity increases towards H_c and subsequently collapses. For horizontal polarization the lineshape is the same but the intensities are a little lower, probably caused by a small difference in the calibration factor of the I_0 monitor for x - and y - polarized light.

The *even* order maxima display a much more complicated behavior with notably different results for the two polarizations. We will focus first on the second order at 20 K reproduced for clarity in Fig. 6.6, which also shows the corresponding intensities at the Fe L₃ edge. For x -polarized photons at the Gd M₅ edge two intensity maxima around ± 0.1 T are observed with a local minimum and a sharp jump at H_c . For y -polarized light the second order has lower inten-

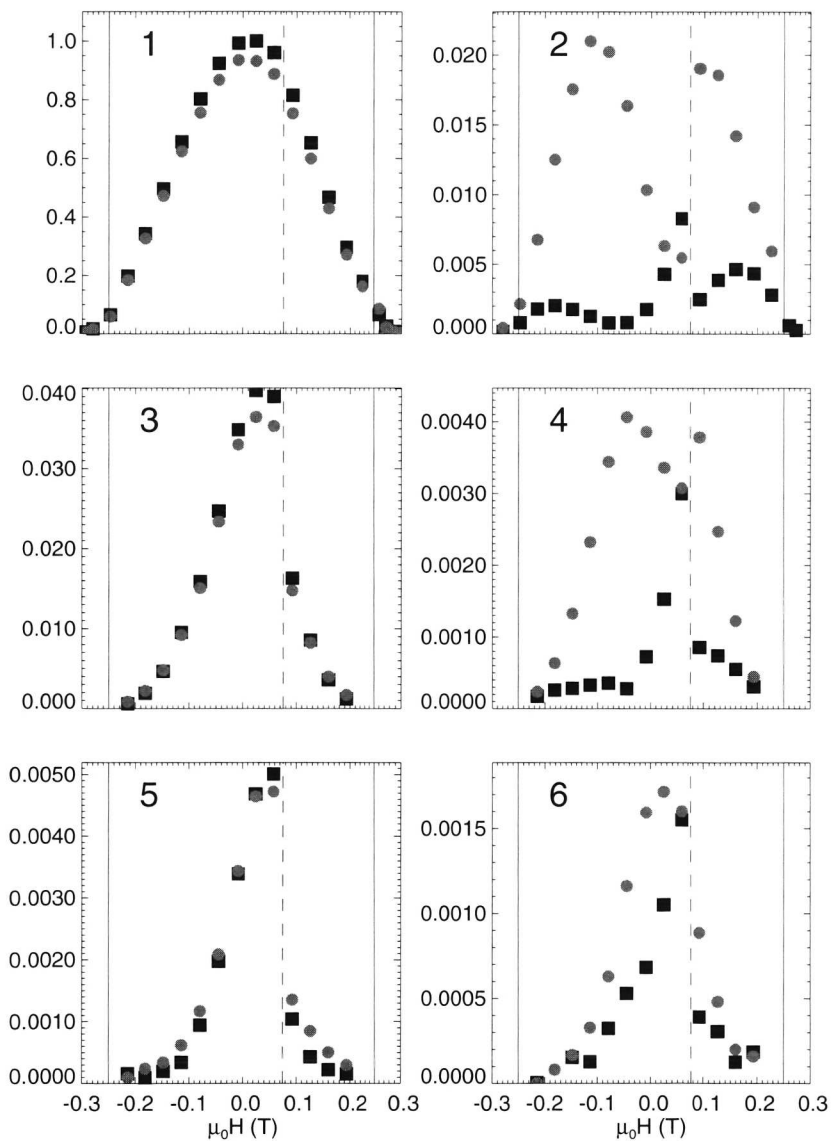


Figure 6.4: Intensity of the integrated diffraction peaks as a function of in-plane field at 20 K for x - (circles) or y - (squares) linear polarization vector. The dashed vertical lines indicate H_c , the full vertical lines mark the boundaries of the period hysteresis.

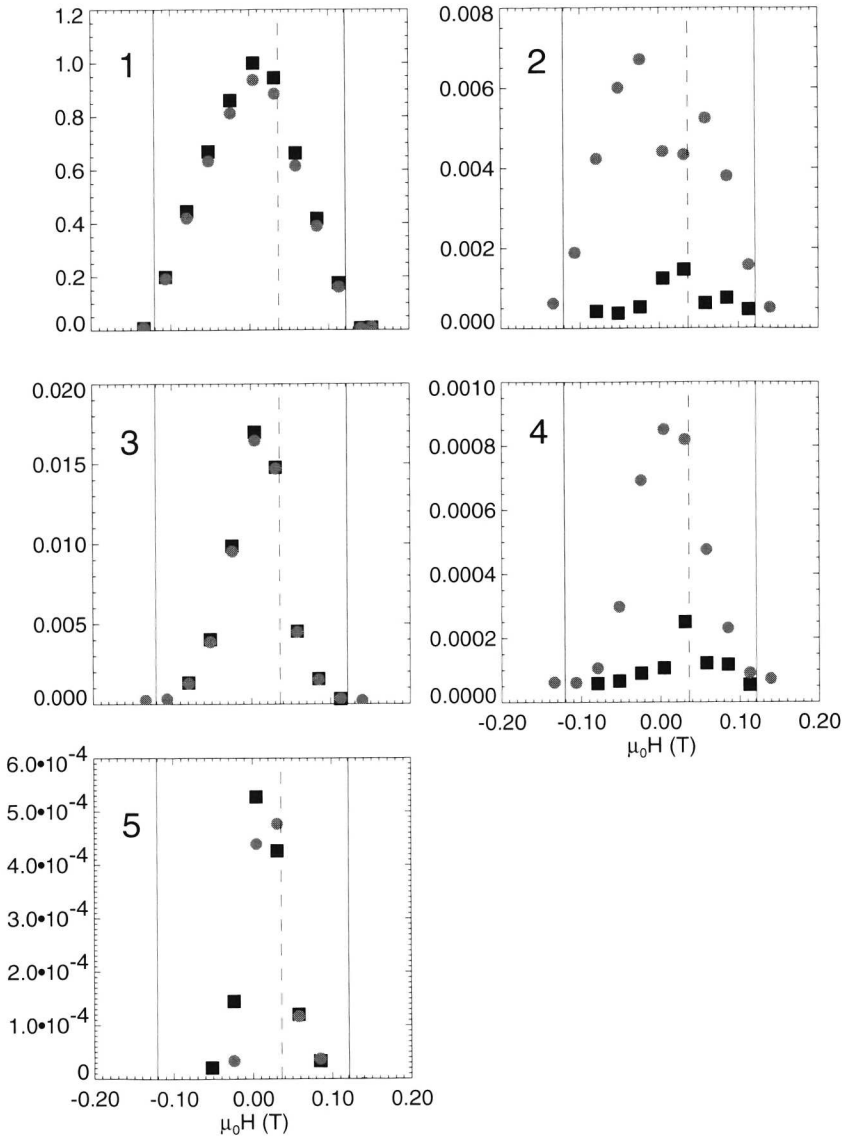


Figure 6.5: Intensity of the integrated diffraction peaks as a function of field at 300 K for x - (circles) or y - polarized light (squares). The dashed vertical lines indicate H_c , the full vertical lines mark the boundaries of the period hysteresis.

sity, displaying two broad shoulders which are found also at the Fe L_3 edge for both polarizations. However the y -polarized Gd M_5 data show an additional sharp peak coinciding with the local minimum for x -polarization.

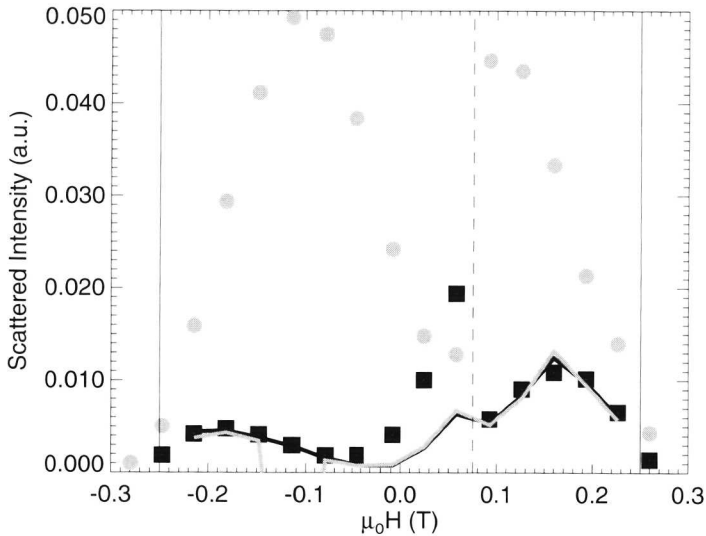


Figure 6.6: A comparison of the field-dependent scattered intensities on the second order for x - (circles) and y - polarized (squares) light at 20 K at the Gd M_5 edges. Solid lines: at the Fe L_3 edge. The dashed vertical lines indicate H_c , the full vertical lines mark the boundaries of the period hysteresis.

Returning to Fig. 6.4 we find the curves for the 4th and 6th order to sharpen up with respect to the second order, as the 3rd and 5th order do with respect to the first order. The fourth order, on the center right, still has a dip for x -polarization and a peak for y -polarization at the same field as those of the second order, but the sixth order is reduced to a single peak for both polarizations. However in all cases there is a distinctive jump in intensity on passing H_c .

6.2.3 GdFe₉

Fig. 6.7 shows the room-temperature diffraction pattern for remanent aligned stripes in the GdFe₉ film. Even at remanence a second and third order max-

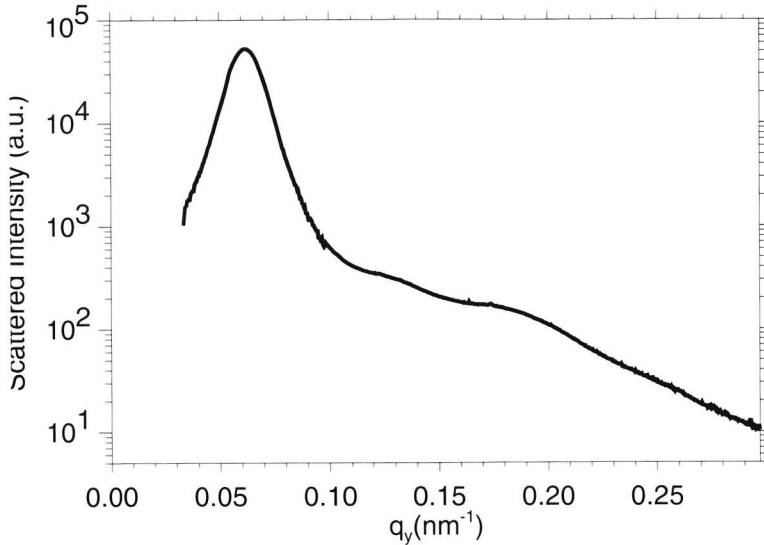


Figure 6.7: Diffraction pattern from remanent aligned stripes in a 42 nm GdFe₉ sample at the Gd M₅ resonance and for *x*-polarized x rays.

imum are barely visible and they vanish very rapidly with applied field. We therefore could only follow the evolution of the first order diffraction peak. The results at 20 K and room-temperature are shown in Fig. 6.8, which is equivalent to Fig. 6.3. The general behavior is very similar, however in comparison with the GdFe₅ sample, the periods are nearly a factor 2 smaller, the total scattered intensities are much lower and the disorder in the system is larger. The linear dichroism curves in the bottom panel show that the sample stays mainly in-plane magnetized along *x*, even at remanence. At 20 K a closure component could be detected from these data, but for room temperature the transmission result was too poor to give conclusive evidence for closure.

6.3 Modelling the diffracted intensities

We will analyze the diffracted intensities using the 1-dimensional model discussed in Chapter 2.3. In this model $m_x^2 + m_z^2 = 1$ and $m_z = \sin \theta_0 s(y)$ where $s(y)$ is a periodic function and θ_0 is the maximum out-of-plane angle. We will

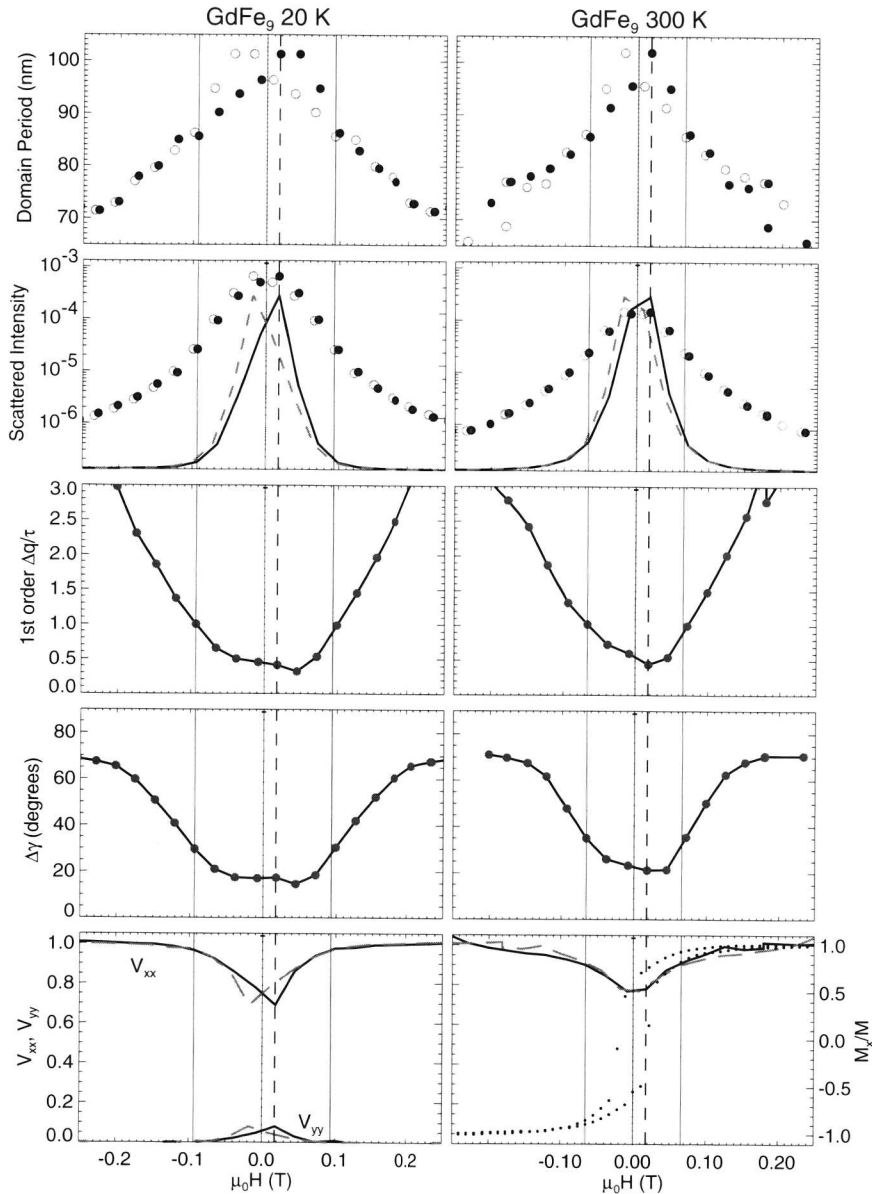


Figure 6.8: In-plane field dependence of the period, total intensity, radial peak width and angular peak width extracted from the diffraction data for 40 nm GdFe₉ at 20 K (left) and room-temperature (right). The filled respectively open symbols and the dark respectively broken lines indicate the up- and down-branches of the hysteresis loop. The bottom panel shows the total fractions V_{xx} and V_{yy} together with the longitudinal MOKE magnetization loop (small dots) for room temperature.

now assume that m_x and m_z are uniform over the film thickness. The contrast functions as defined in Chapter 5 can then be written as:

$$g_z(y) = \sin \theta_0 s(y) \quad (6.5)$$

$$g_{xx}(y) = \cos^2 \theta_0 + \sin^2 \theta_0 [1 - s(y)^2] \quad (6.6)$$

where we have written g_{xx} explicitly as a constant $\cos^2 \theta_0$ part and a variable part $\sin^2 \theta_0 (1 - s(y)^2)$.

To include closure magnetization we extend the model by allowing the domain wall magnetization to *twist* from the x to the y -direction as depicted in Fig. 2.1 F. The amplitude of m_y is determined by the canting angle and a twist angle $\phi(z)$:

$$m_y^2(y, z) = \sin^2 \theta_0 \sin^2 \phi(z) [1 - s(y)^2]. \quad (6.7)$$

Since in the transmission experiment we are insensitive to the z -direction we define a thickness averaged twist amplitude $t = \overline{\sin^2(\phi)}$. With the requirement that $\sum_i m_i^2 = 1$ and m_z is constant as a function of z the contrast functions are given by

$$g_{xx}(y) = \cos^2 \theta_0 + (1 - t) \sin^2 \theta_0 [1 - s(y)^2] \quad (6.8)$$

$$g_{yy}(y) = t \sin^2 \theta_0 [1 - s(y)^2] \quad (6.9)$$

$$g_z(y) = \sin \theta_0 s(y). \quad (6.10)$$

Reformulating the combined equations (5.7) and (5.7), we find for the intensity of the n -th diffraction order

$$I_n^{x-x'} \propto [(1 - t) \sin^2 \theta_0]^2 |F^{(2)} \frac{N}{P} \int_{-\frac{1}{2}P}^{\frac{1}{2}P} s(y)^2 e^{in\tau y} dy|^2 \quad (6.11)$$

$$I_n^{y-y'} \propto [t \sin^2 \theta_0]^2 |F^{(2)} \frac{N}{P} \int_{-\frac{1}{2}P}^{\frac{1}{2}P} s(y)^2 e^{in\tau y} dy|^2 \quad (6.12)$$

$$I_n^{x-y', y-x'} \propto \sin^2 \theta_0 |F^{(1)} \frac{N}{P} \int_{-\frac{1}{2}P}^{\frac{1}{2}P} s(y) e^{in\tau y} dy|^2, \quad (6.13)$$

where we have explicitly given all the separate scattering channels for x - and y - polarized light. These expressions show that the intensity of the diffraction orders correspond to the squared Fourier coefficients of $s(y)^2$ and $s(y)$. The advantage of this model is that a single periodic function describes both the in-plane and out-of-plane magnetic contrast.

6.4 Domain nucleation

In all magnetization curves we can recognize a reversible part and an irreversible part where the stripe period has hysteresis. In the high-field reversible part of the magnetization curves only a single diffraction maximum could be observed with a linear increasing period and a gradual increase in intensity. The theory of nucleation introduced in section 2.4 predicts that, at nucleation, the infinitesimal out-of-plane oscillation of the magnetization has a sinusoidal profile. Taking $s(y) = \cos(\tau y)$ and neglecting the closure component m_y ($\phi(z) = 0$), it follows that for x -polarized light

$$I_{\pm 1} \propto \frac{1}{4} \sin^2 \theta_0^2 |F^{(1)}|^2 \quad (6.14)$$

$$I_{\pm 2} \propto \frac{1}{16} \sin^4 \theta_0 |F^{(2)}|^2, \quad (6.15)$$

hence near nucleation two diffraction maxima should be observed at the Gd M_5 edge. However, close to saturation the canting angle is small, so $I_{\pm 1} \gg I_{\pm 2}$. Also the stripe orientation and correlation are rather poor leading to a considerable broadening of the diffraction peaks. As a result the second order peak is washed out on the shoulder of the primary peak and we only start to observe it just before H_{hys} , where the canting angle and the stripe order have become large enough.

Another interesting phenomenon in the reversible stage is that the slow rise in intensity is accompanied by a rapidly improving parallel orientation and better correlation of the stripes (Fig. 6.3 and Fig. 6.8 third and fourth rows). The emerging intuitive picture is that when the out-of-plane amplitude increases the dipolar interaction develops and the stripe-stripe interaction leads to an ordering of the system. It is important to note that at nucleation the diffraction pattern forms a ring indicating that either the 'domain walls' meander, or a bubble rather than a stripe state has nucleated.

At H_{hys} the dipolar interaction becomes so strong that an energy penalty is involved in the creation/annihilation of a domain or domain wall. As a result the period is no longer reversible. Also the ordering of the stripes seems completed and for GdFe₅ higher diffraction order maxima become visible at this field. The latter indicates that the magnetization profile is no longer sinusoidal. We therefore interpret this as a transition from a nucleation phase to a fully developed

domain state with up- and down stripe domains separated by a well defined domain wall.

6.5 Evolution of the domain state

For an in-plane applied field there is no net out-of-plane magnetization, hence the up- and down domains are of equal width $W = P/2$. As shown in the previous chapter, in that case $s(y)$ gives only odd Fourier coefficients that according to (6.13) produce odd order diffraction maxima with the same intensity for both polarizations. Their intensities are proportional to the canting angle, which is maximum around remanence.

In the same model the even orders are either due to the in-plane magnetic contrast of the Bloch walls Eq. (6.11) for x -polarized light or the closure domains Eq. (6.12) for y -polarized light. In the high field region, the closure magnetization Eq. (6.9) can be neglected ($t = 0$), the in-plane scattering is dominated by the Bloch walls. According to (6.11) for x -polarized light the second order intensities are proportional to $\sin^4 \theta_0$ and therefore the second order intensity initially rises fast. However, as the period increases, the number of domain walls decreases and the second order intensity starts to decrease, simultaneously the closure magnetization component starts to develop, visible as the sharp peak found on the second order for y -polarized light.

As already remarked, for y -polarized light we also found two broad shoulders at high fields. Fig. 6.6 showed that these shoulders are also observed at the Fe L_3 edge, for both polarizations. Since at the Fe edge $F^{(2)}$ is negligibly small, all features are due to g_z as given by Eq. (6.13). The observation of even order scattering can only be explained by a magnetization profile that has even order Fourier terms, which implies that the 'up' domains are bigger than the down domains or vice versa. This in turn implies a net out-of-plane magnetization which can be produced only by a perpendicular component in the applied field, most likely caused by a small misalignment of the magnetic field with respect to the sample plane.

We therefore conclude that only the sharp peak observed at the Gd M_5 edge for y -polarized light in the field region $[0, H_c]$ can be attributed to closure domain scattering. This interpretation is confirmed by the field dependence of the total

closure domain fraction V_{yy} . Apart from this small region we may describe the transition from up- to down magnetization by a pure Bloch wall extending over the thickness of the film and the magnetization profile is truly 1-dimensional. In the following we have subtracted out the Fe data from the even order intensities at the Gd edge and neglect the up- down asymmetry. This is allowed provided the asymmetry is small.

6.6 Quantification of domain wall width over the magnetization loop

The stripe structure is relatively simple, consisting of an up- and a down domain separated by a domain wall. For this type of structure the low order Fourier coefficients are to first order determined by the domain wall width. By comparing Eq. (6.11)-(6.13) for a model $s(y)$ with the diffracted intensities we may in principle hope to retrieve the domain wall width.

The diffracted intensities for a model unit cell, as given in Fig. 6.9, were calculated taking for the domain-wall the standard Bloch-wall profile $\tanh(\pi y/\delta)$ [31] of width δ and at a position $1/2W$, where $W = 1/2P$ is the domain width. The function $s(y)$ was normalized to 1 at $y = 0$. The only parameter that is varied is the relative domain wall width δ/W .

The first approach that can be taken is to compare the intensity ratios of the odd order peaks to (6.13) and that of the even order peaks to (6.11)-(6.12). The advantage is that these ratios are independent of the resonant amplitudes $F^{(1)}$ and $F^{(2)}$ and of the canting angle and twist factor t . The results for x -polarized light are shown in Fig. 6.10, indicated by the open symbols. There are differences in the domain wall widths obtained from the different orders but the overall behavior is very similar, showing a minimum of about 40 nm at the coercive field. The exception is the field range where the closure domain scattering is observed for the sample at 20 K; there the even orders seem to indicate a wall width of 20 nm. This smaller width suggests that the domain wall profile in the center of the film, where the domain walls are of the Bloch type, is sharper than that at the surfaces, where the domain walls are of the closure type. Another possible explanation is that at this field a surface domain wall has nucleated in between

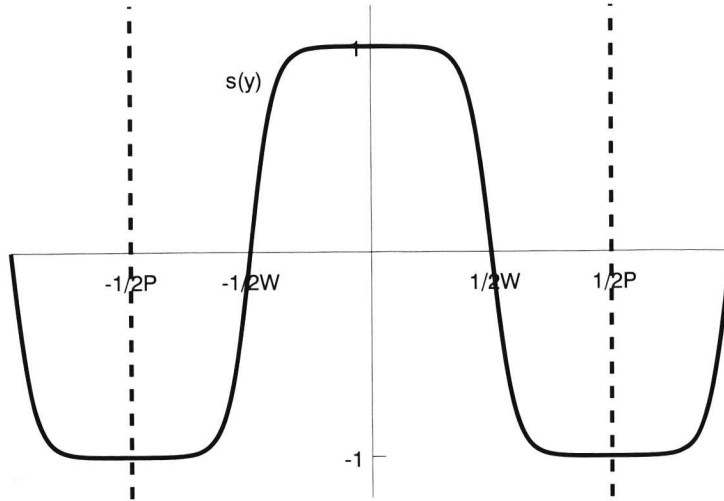


Figure 6.9: Model domain function $s(y)$ for domain of width $W = 1/2P$ and $\delta = 0.3W$. The dashed lines indicate the integration range for the unit cell.

the domain walls, as indicated in Fig. 6.12-D. For such a magnetization profile the in-plane scattering cross sections not only has maxima at $y = \pm 1/2W$ but also at $y = 0, \pm W$, which enhances the fourth order diffracted intensity, leading to an underestimation of the domain wall width in the 1-dimensional model. We will discuss this structure in more detail in the last section.

So far the effect of the disorder was not taken into account. In reality the domain width varies by $\sim 10\%$ of its width and this leads to cumulative disorder: the position of the n^{th} domain with respect to the k^{th} domain is the sum of the widths of the domains in between n and k . In that case expression (5.7) separating the scattering properties of the domains and the lattice is no longer valid. If the width fluctuates statistically independent, the scattered intensity can still be expressed analytically, as shown by Fullerton [96] for multilayer reflections. Preliminary results along these lines show that this type of disorder leads to a broadening of the diffraction peaks that increases with their order, as found in our data. Furthermore the intensity of the higher order peaks decreases. There-

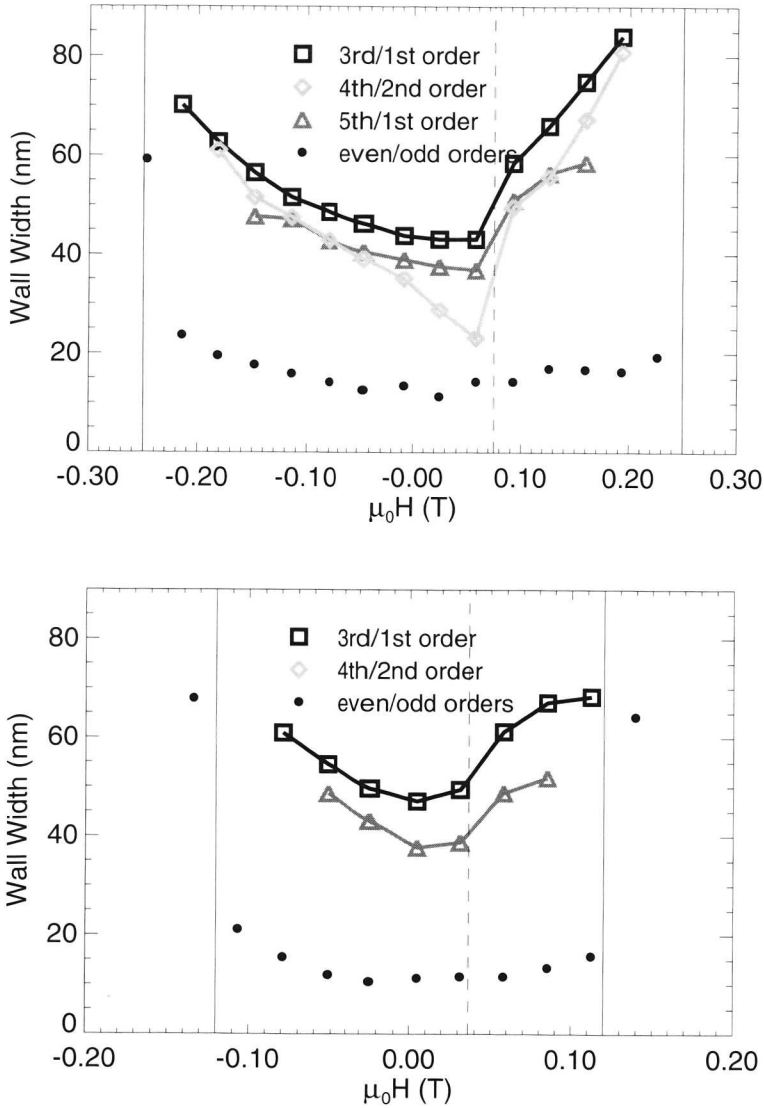


Figure 6.10: Domain wall width as function of field for a 40 nm $GdFe_5$ thin film. Top: at 20 K. Bottom: at room temperature.

fore the results in Fig. 6.10 represent an upper limit of the domain wall width.

From the disorder model we also find that the *total* out-of-plane and in-plane scattered intensities are not altered by the disorder: by energy conservation the intensity scattered out of the diffraction peaks by the disorder is scattered to smaller q values. The total scattered intensities correspond to the total scattering volume of the domains and domain walls, which in our model depend on the domain wall width only. We may therefore obtain the latter by comparing the total even order to the total odd order intensity. As can be seen from equations (6.11)-(6.13), this requires knowledge of the ratio $|F^{(2)}|/|F^{(1)}|^2$, the twist factor t and the canting angle θ_0 . The first can be obtained from the known optical constants for a given energy. According to Eq. (6.11) and Eq. (6.12) the twist factor can be calculated by taking the ratio of the even order scattered intensity for y - and x -polarized light. The canting angle can be determined by working out Eq. (6.1) for the model $s(y)$ and wall width δ

$$V_{xx} = \cos^2 \theta_0 + \sin^2 \theta_0 (1 - t) \frac{1}{P} \int_{-1/2P}^{1/2P} (1 - s(y)^2) dy, \quad (6.16)$$

and comparing this to the experimentally measured V_{xx} as given in (Fig. 6.1).

The wall widths obtained in this manner, shown in Fig. 6.10 as the filled dots, are appreciably smaller. However, before the disorder-order transition the wall width is of the order of half the period, signifying a sinusoidal oscillation. We estimate the error on these wall width values to be on the order of 5 nm due to uncertainties in the exact energy calibration and V_{xx} . Within this error the minimum wall width of approximately 12 nm is the same for the sample at 20 K and at room-temperature.

6.7 Determination of the anisotropy and exchange constants from the nucleation field and period

In the experiment we followed the stripe period up to saturation and hence we obtain precise values for the critical field and period H_{cr} and P_{cr} (see Table 6.1), where the stripes nucleate/disappear. The theory of nucleation [31] relates the reduced nucleation field h_{cr} and reduced inverse domain width w_{cr}^{-1} to the quality factor Q , as shown in Fig. 6.11, right panel, which is the same as Fig.

Table 6.1: Macroscopic magnetic properties obtained from the nucleation field and period. H_{cr} and P_{cr} were determined from the magnetization and diffraction data, M from the XMCD data and x_c . h_{cr} , Q and K_u are determined from H_{cr} , P_{cr} and M . d is determined from Q and h_{cr} , A and δ_b follow from K_u and d . I: GdFe₅ 20 K, II: GdFe₅ 300 K, III: GdFe₉ 20 K, IV:GdFe₉ 300 K

sample	$\mu_0 H_{cr}$ T	P_{cr} nm	M 10^5 A/m	h_{cr}	Q	K_u 10^5 Jm ⁻³	d	A 10^{-12} J/m	δ_b nm
I	0.4	120	4.4	0.56	1.2	1.5	1	6.1	21
II	0.18	105	3.6	0.49	0.8	0.65	1.1	2.9	20
III	0.2	75	9.0	0.46	0.4	2.0	1.2	4.4	18
IV	0.15	78	7.0	0.43	0.4	1.2	1.3	2.7	17

2.7 and shows the critical lines for stripe nucleation for different values of h_{cr} . The reduced width $w_{cr}^{-1} = D/W_{cr} = 2D/P_{cr}$ is easily obtained from the film thickness D and nucleation period P_{cr} . The reduced nucleation field defined as

$$h_{cr} = \frac{\mu_0 M H_{cr}}{2K_u} = \frac{H_{cr}}{MQ} \quad (6.17)$$

is a function of Q and the saturation magnetization M . For known M and H_{cr} , $w_{cr}^{-1}(h_{cr}, Q)$ is a function of Q only (see Fig. 6.11), and one can deduce Q from the reduced nucleation field and period. With Q and M known the anisotropy constant K_u is found from the relation $Q = K_u / \frac{1}{2} \mu_0 M^2$. The nucleation theory also relates the reduced critical thickness $d_{cr}(h_{cr}, Q)$ to the nucleation field h_{cr} and anisotropy factor Q , as shown in the left panel of Fig. 6.11. Hence from the values of h_{cr} and Q we find the reduced thickness $d = d_{cr}$ of the samples at 20 K and room temperature. Since the reduced thickness $d = D / (2\pi \sqrt{A/K_u})$, where D is the film thickness, this allows us to extract the exchange constant A from d , h_{cr} , and K_u .

A reasonably accurate estimation for M was obtained from the moments of Fe and Gd at 20 K and room-temperature determined from the XMCD experiment in Chapter 4 and the compensation composition x_c at these temperatures. The obtained h_{cr} , Q , K_u , d , and A values together with the values of M are given in Table 6.1. These values compare reasonable well to the literature values [49, 50, 51, 52]. The bulk Bloch wall widths $\delta_b = \pi \sqrt{A/K_u}$ and reduced thickness are also given in the table.

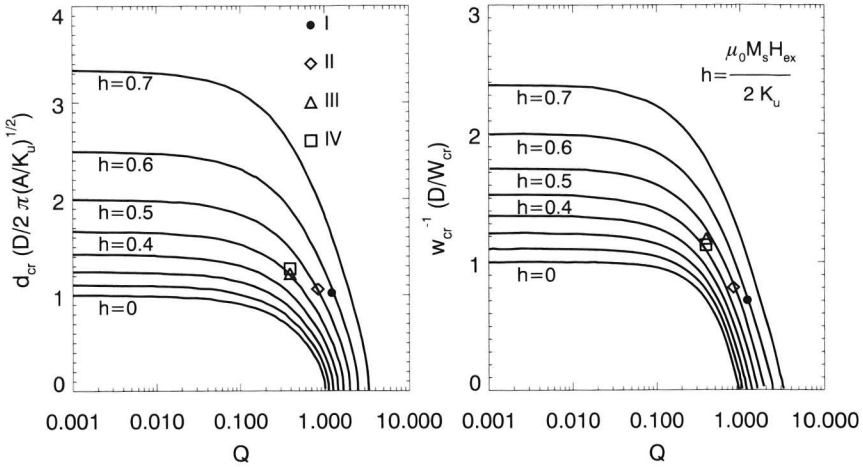


Figure 6.11: The critical thickness d_{cr} for stripe formation (left) and the corresponding inverse critical stripe width w_{cr}^{-1} (right) as a function of Q for different applied in-plane fields h along the stripe direction. The symbols indicate the values found for I: GdFe₅ 20 K, II: GdFe₅ 300 K, III: GdFe₉ 20 K, IV: GdFe₉ 300 K

6.8 Comparison of the microscopic diffraction data and the macroscopic magnetic properties

As discussed in Chapter 2, important factors determining the stripe state are the anisotropy factor Q and the reduced thickness d . Q and d for the two samples and temperatures have been plotted in the left panel of Fig. 6.11. This shows that going from I (GdFe₅ 20K) to IV (GdFe₉ 300 K) the samples get closer to the critical line for $h = 0$ for a given Q value. Going towards this line, either by decreasing d or Q , has the same effect as increasing h , hence the period and canting angle should be reduced.

Indeed at 300 K the period is smaller than at 20 K for GdFe₅. For GdFe₉ the periods are even further reduced. The behavior of the canting angle follows from the in-plane fraction V_{xx} , which according to Eq. (6.1) is in large part determined by $\cos^2 \theta_0$. For GdFe₅ at 300 K V_{xx} is larger than at 20 K, hence the canting angle is smaller. For GdFe₉ we found the sample stays mainly in-plane over the

whole magnetization loop, implying small canting angles even at remanence. The smaller canting angles also explain the much lower total scattered intensity for GdFe_9 compared to GdFe_5 .

Due to the small out-of-plane undulation of the GdFe_9 sample also the dipolar interaction between the stripes is weak. As a result the hysteresis in the period is much smaller whereas the disorder is larger. Even at the coercive field the correlation length is of the order of the stripe period. Furthermore a sharp transition in $\Delta q/\tau$ and $\Delta\gamma$ as observed for GdFe_5 is not found. This leads to the important conclusion that the GdFe_9 sample is so close to the critical thickness that the stripe domain state does not fully develop. Although the bulk Bloch wall width $\delta_b = \pi\sqrt{A/K_u}$ of 17 nm is small compared to the domain period, this width is never reached as higher order diffraction maxima are not observed.

For GdFe_5 the values of A and K_u yield a bulk Bloch wall width of 20 nm. This compares reasonably well with the wall width obtained from the diffraction maxima, although the latter is on the low side. In this respect it is important to note that we obtained this wall width from the total intensities in the even and odd order diffraction *peaks* and did not take into account the intensity that is scattered to low q by the disorder. With this method we may have underestimated the even order intensity compared with the odd order intensity and hence have underestimated the domain wall width. A polarization analysis would facilitate a complete separation of the in-plane and out-of-plane scattered intensities and in this way the method could be improved.

6.9 Overview of in-plane reversal loop

In this chapter we have analyzed the diffraction data for the GdFe_5 sample in terms of a simple 1-dimensional magnetic structure. Here we summarize the salient points of our analysis and give a qualitative reconstruction of the internal magnetic structure at various parts of the magnetization curve, see Fig. 6.12, going from negative (top) towards positive saturation field (bottom).

At nucleation (panel A) we only see a single diffraction maximum, indicative of the out-of-plane magnetic contrast. As the amplitude of the undulation increases a second order diffraction peak appears for x -polarized light, but not for y -polarized light. This signifies that the 'domain wall' for the sinusoidal

undulation is of the Bloch type and that at this stage there is hardly a closure component in the film. These observations compare well with the nucleation state for a system with $Q = 1$ and a reduced nucleation field $h_n = 0.6$ as shown in Fig. 2.6-d. This state is depicted schematically in panel A, where we have indicated that towards the surface the film is more in-plane magnetized than at the core.

In the next stage of the magnetization loop, $H < |H_{lys}|$ the domain wall has fully developed and higher order diffraction maxima appear (panel B). The absence of closure scattering proves that in this stage the magnetization profile is still purely 1-dimensional with a Bloch wall that runs from the top to the bottom surface of the film.

A closure component, as indicated in panel C, starts only to develop near remanence, where the external field $H_x = 0$. Towards the coercive field the closure domains grow rapidly and the structure becomes vortex-like. The Bloch wall $-m_x$ magnetization is trapped by a circulating magnetization, m_z, m_y . Upon passing H_c the closure scattering disappears almost completely and the system is better ordered, visible as the reduction of $\Delta q/\tau$ upon passing H_c . The release of energy at reversal apparently anneals the structure, leading to a better alignment.

The question is how the cores of these vortices, which have their magnetization now opposed to the in-plane field direction, reverse. At the coercive field the net magnetization $m_x = 0$, but at the same time a net m_x^2 is found from the field dependent linear dichroism experiment. Apparently the sample still has magnetization in the x -direction but part of it along the negative and part of it along the positive direction.

A possible solution is that the in-plane m_x reversal starts at the surfaces, as drawn in panel D, and as calculated for weak stripe domains in thin films with a canted easy axis [56]. Towards the coercive field the x -component of the magnetization at the surfaces becomes more extended, possibly pushing the closure magnetization inward creating a 360° domain wall from the top to the bottom of the film, as indicated schematically in panel E. The vortex cores become highly frustrated and collapse catastrophically at the magnetization reversal. After reversal the closure magnetization is absent and again a 1-dimensional Bloch state

is obtained, see panel F, which is similar panel B.

Alternatively a reverse domain wall may nucleate by going directly from the situation in panel C (or D) to panel F. At H_c the sample is then partly in state C (D) and partly in state F, such that the net magnetization along x is zero. Such nucleation occurs probably at the sides of the sample and this state then sweeps through the sample almost instantaneously.

Qualitatively, the behavior of the GdFe_9 sample is quite different. The values of Q and h_{cr} found here compare well with $h_{cr} = 0.3$ and $Q = 0.4$ for which the nucleation state is drawn in Fig. 2.6-C. A vortex-like structure with a considerable closure component exists already at nucleation. This state could be compared with Fig. 6.12-C, which only indicates the variation of the m_y and m_z , not the large constant in-plane magnetization m_x . At 20 K we found that the closure fraction V_{yy} at remanence is comparable to that for GdFe_5 , which is relatively large since the canting angles are much smaller. Probably the magnetic structure for GdFe_9 stays close to that of panel C over the magnetization loop. A mechanism where the reversal starts at the surfaces, like in panel D seems unlikely here since even at H_c , much of the sample is in-plane magnetized along x and the sample is most likely partly reversed (panel C with the dots replaced by crosses). Such a reversal would happen by the nucleation of reverse in-plane 'domains' in a first order transition.

CONCLUDING REMARKS AND OUTLOOK

This thesis encompasses an exploration of resonant soft x-ray magnetic scattering as a probe of magnetic structure on the nanometer length scale. We extensively investigated the energy- and polarization dependence at the Gd $M_{4,5}$ and Fe $L_{2,3}$ edges of the resonantly scattered intensity from aligned stripe domains in a $GdFe_5$ thin film. The power of the method was demonstrated in a detailed study of the nucleation and evolution of the internal magnetic structure of nanoscale stripe domains in in-plane applied fields.

With the photon energy tuned to the Gd M_5 edge we have shown that XRMS can be used as a microscopic 3-dimensional magnetometry: using linear polarized light we could separate the scattering from the in-plane linear magnetic $F^{(2)}$ contrast of Bloch walls and surface closure domains from the out-of-plane circular magnetic contrast $F^{(1)}$ of the bulk stripes. The large linear dichroism compared to the transition-metal $L_{2,3}$ resonances that have been exploited in soft x-ray scattering experiments so far is a unique feature of this experiment.

The maximum momentum transfer in our experiments corresponds to a length scale of ~ 30 nm, comparable to the single domain size and clearly too large to resolve its exact profile: however we have shown that for the relatively simple domain structure the low order Fourier coefficients are primarily determined by the width of the domain wall. In order to obtain quantitative results, we need a careful analysis of the disorder on the diffracted intensities. With a polarization

analysis of the diffracted intensity, using multilayer mirrors, it should be possible to determine the domain wall width with 5 nm precision.

We presented field dependent XRMS experiments for the in-plane magnetization curve at 20 K and room temperature for a GdFe₅ and a GdFe₉ thin film. We could measure the diffracted intensity up to the critical field, exemplifying the sensitivity of the method and allowing the determination of the macroscopic magnetic properties of these samples. The corresponding theoretical nucleation states for the macroscopic parameters compare well with our diffraction data results.

For the GdFe₅ sample we found an intriguing microscopic reversal of the stripes upon passing H_c , involving a complex vortex state. We have proposed a speculative model where the reversal occurs via the formation of reversed domain walls at the surface and a collective collapse of the vortex cores. In the normal incidence transmission geometry used here we are sensitive to the internal magnetic structure integrated over the film thickness. It is therefore difficult to unambiguously prove this 2-dimensional reversal model. However highly surface sensitive and depth dependence measurement are possible using a reflection geometry as shown by Dürr *et al.* for stripes in FePd [18].

As an example we show in Fig. 7.1 the in-plane diffraction pattern for grazing incidence reflection from the remanent aligned stripe lattice in the GdFe₅ thin film. Here we see the first two diffraction orders on the sides of the specular reflected intensity at $q_y = 0$. Remarkably the second order diffracted intensity is much larger than the first order scattered intensity and all diffraction orders have a large left/right asymmetry. In this geometry the circular magnetic contrast is sensitive mainly to the parallel $m_x(y)$ structure of the Bloch walls whereas the linear magnetic contrast is sensitive to $m_y^2(y)$ and $m_z^2(y)$. All these terms scatter to even orders only. It can be shown that the large left-right asymmetry that is observed is due to an interference between a $m_z m_y F^{(2)}$ term and a $m_x F^{(1)}$ term.

We have investigated the energy dependence of this diffraction pattern, finding a rather complex behavior compared to the transmission results. The detailed analysis is much more complicated and falls out of the scope of this thesis. However these data prove that at remanence a Bloch component extends up-to-the

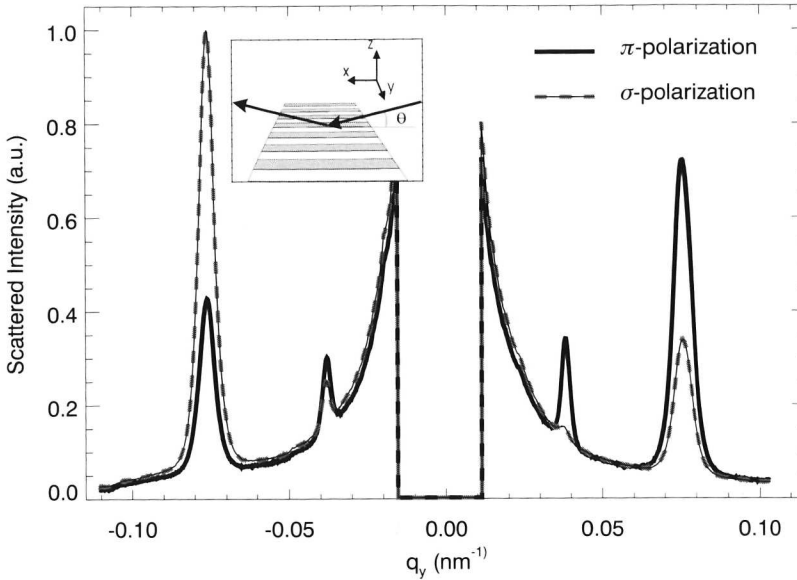


Figure 7.1: Scattered intensity as a function of the in-plane momentum transfer q_y from a remanent aligned stripe lattice in a reflectivity geometry. The beam was incident at a 3.5° grazing angle in the xz -plane of the sample, as indicated in the inset. The photon energy was tuned to the Gd M_5 resonance, curves for linear polarized light perpendicular σ and parallel π to the xz -plane are shown.

surface but a closure component is also existent. No in-plane field-dependent reflectivity data for this structure are available to date but such data would directly test the reversal model proposed here.

Reciprocal space techniques can be extremely powerful for studies of dynamic systems, as has been shown both at optical and hard x-ray wavelengths. In this respect it's worth mentioning that there is room for improvement of the sensitivity of the 2-D detector which should make it possible to measure at video rates. The use of magnetic pump- x-ray probe techniques, utilizing the time structure of the synchrotron beam, offers promise to study dynamical phenomena at the nanometer length scale and in the nanosecond regime.

We have also started to explore the use of coherent x rays for the study of criti-

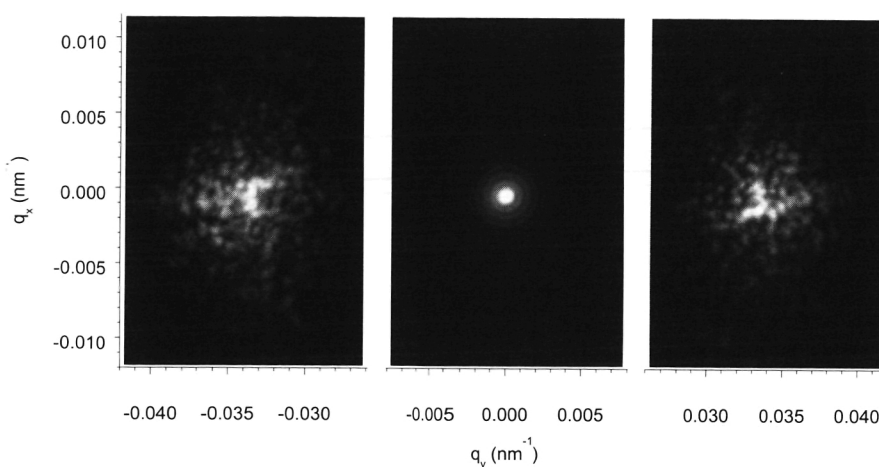


Figure 7.2: Soft x-ray magnetic speckle from an aligned stripe lattice illuminated by a $10 \mu\text{m}$ coherent beam. Central part: Fraunhofer diffraction from the pinhole on the transmitted beam. Sides: Speckle on the first order diffraction maxima.

cal scattering experiments. A preliminary account has been presented [23] that shows that important steps in beamline stability and detector technology are required. High quality *static* magnetic speckle patterns for the first order diffraction maxima can be obtained by illuminating the stripe lattice with a $10 \mu\text{m}$ coherent beam. This result is encouraging for the pursuit of dynamic studies of critical magnetic phenomena.

LIST OF SYMBOLS

Table 1: List of symbols and abbreviations, continues on next page

Symbol	Definition
μ_0	vacuum magnetic permeability
ϵ_0	vacuum dielectric constant
E	Electric Field
D	Electric Displacement
H	Magnetic Field
B	Magnetic Induction
χ	Electric susceptibility tensor
κ	Relative dielectric tensor
M	Magnetization vector
M	Saturation magnetization
$\mathbf{m} = \mathbf{M}/M$	Unit magnetization vector
$0 < x < 1$	Fe fraction in $\text{Gd}_{1-x}\text{Fe}_x$ thin films
x_c	Compensation composition for which $M = 0$
H_c	Coercive field
H_{hys}	Hysteresis field of stripe period
K_u	Uniaxial magnetic anisotropy
$K_s = \frac{1}{2}\mu_0 M_s^2$	Thin film shape anisotropy
$Q = K_u/K_s$	Quality factor or reduced anisotropy
D	Film thickness
A	Exchange stiffness
$h = \frac{\mu_0 H M_s}{K_u}$	Reduced field
$d = \frac{D}{2\pi\sqrt{A/K_u}}$	Reduced thickness
$\delta_b = \pi\sqrt{A/K_u}$	Bloch wall width

Table 2: List of symbols and abbreviations

Symbol	Definition
\mathbf{k}	Wavevector
\mathbf{q}	Momentum transfer
$\hat{\mathbf{e}}$	Polarization vector
n	Complex refractive index
μ	Attenuation coefficient
$-r_0$	Free electron scattering length
\mathbf{f}	Atomic scattering tensor
f	Atomic scattering amplitude
f^0	Thomson atomic scattering amplitude
$F^{(0)}$	Charge resonant scattering amplitude
$F^{(1)}$	Circular magnetic resonant scattering amplitude
$F^{(2)}$	Linear magnetic resonant scattering amplitude
$+, -$	Labels for left/right circular polarization
$//$	Label for linear polarization parallel to \mathbf{m}
\perp	Label for linear polarization perpendicular to \mathbf{m}
$\mu_+ - \mu_-$	Circular magnetic dichroism
$\mu_{//} - \mu_{\perp}$	Linear magnetic dichroism
I_0	Incident intensity
I_t	Total transmitted intensity
I_s	Total scattered intensity
$g_i = \int_0^D m_i(y, z) dz$	Magnetic contrast function circular term
$g_{ij} = \int_0^D m_i m_j(y, z) dz$	Magnetic contrast function linear term
G_i, G_{ij}	Fourier transforms of g_i and g_{ij}
\mathcal{F}	Form factor
S	Structure factor
P	Period of stripe lattice
$\tau = 2\pi/P$	Reciprocal period
W	Single domain width
$w = W/D$	Reduced stripe width
$s(y)$	Shape function
θ_0	Canting angle
ϕ	Twist angle
t	Twist factor

REFERENCES

- [1] A. J. COX, J. G. LOUDERBACK, and L. A. BLOOMFIELD, *Experimental observation of magnetism in rhodium clusters*, Phys. Rev. Lett. **71**, 923 (1993).
- [2] S. PADOVANI, I. CHADO, F. SCHEURER, and J. P. BUCHER, *Transition from zero-dimensional superparamagnetism to two-dimensional ferromagnetism of Co clusters on Au(111)*, Phys. Rev. B **59**, 11887 (1999).
- [3] B. T. THOLE, G. VAN-DER LAAN, and G. A. SAWATZKY, *Strong magnetic dichroism predicted in the $M_{4,5}$ X-ray absorption spectra of magnetic rare-earth materials*, Phys. Rev. Lett. **55**, 2086 (1985).
- [4] G. VAN DER LAAN, B. T. THOLE, G. A. SAWATZKY, J. B. GOEDKOOP, J. C. FUGGLE, J. M. ESTVA, R. KARNATAK, J. P. REMEIKA, and H. A. DABKOWSKA, *Experimental proof of magnetic x-ray dichroism*, Phys. Rev. B **34**, 6529 (1986).
- [5] G. SCHÜTZ, W. WAGNER, W. WILHELM, P. KIENLE, R. ZELLER, R. FRAHM, and G. MATERLIK, *Absorption of Circularly Polarized X rays in Iron*, Phys. Rev. Lett. **58**, 737 (1987).
- [6] G. SCHÜTZ, M. KNULLE, R. WIENKE, W. WILHELM, W. WAGNER, P. KIENLE, and R. FRAHM, *Spin-dependent photoabsorption at the L-edges of ferromagnetic Gd and Tb metal*, Z. Phys. B **73**, 67 (1988).
- [7] J. STÖHR, *Exploring the microscopic origin of magnetic anisotropies with X-ray magnetic circular dichroism (XMCD) spectroscopy*, J. Magn. Magn. Mater. **200**, 470 (1999).
- [8] J. B. KORTRIGHT, D. D. AWSCHALOM, J. STÖHR, S. D. BADER, Y. U. IDZERDA, S. S. P. PARKIN, I. K. SCHULLER, and H. C. SIEGMANN, *Research frontiers in magnetic materials at soft X-ray synchrotron radiation facilities*, J. Magn. Magn. Mater. **207**, 7 (1999).

- [9] N. SMITH, *Science with soft x rays*, Phys. Today **54**, 29 (2001).
- [10] D. GIBBS, D. R. HARSHMAN, E. D. ISAACS, D. B. MCWHAN, D. MILLS, and C. VETTIER, *Polarization and Resonance Properties of Magnetic-X-Ray Scattering in Holmium*, Phys. Rev. Lett. **61**, 1241 (1988).
- [11] J.P. HANNON, G.T. TRAMMELL, M. BLUME, and DOON GIBBS, *X-ray Resonance Exchange Scattering*, Phys. Rev. Lett. **61**, 1245 (1988).
- [12] P. FISCHER, G. SCHUETZ, G. SCHMAHL, P. GUTTMANN, and D. RAASCH, *Imaging of magnetic domains with the X-ray microscope at BESSY using X-ray magnetic circular dichroism*, Z. Phys. B **101**, 313 (1996).
- [13] P. FISCHER, G. DENBEAUX, F. NOLTING, D. GOLL, T. EIMÜLLER, C. QUITMANN, and G. SCHÜTZ, *Imaging magnetic microstructures with soft X-ray microscopies*, Transactions of the Magnetism Society of Japan **2**, 234 (2002).
- [14] C. KAO, J. B. HASTINGS, E. D. JOHNSON, D. P. SIDONS, G. C. SMITH, and G. A. PRINZ, *Magnetic-Resonance Exchange Scattering at the Iron L_2 and L_3 Edges*, Phys. Rev. Lett. **65**, 373 (1990).
- [15] C. C. KAO, C. T. CHEN, E. D. JOHNSON, J. B. HASTINGS, H. J. LIN, G. H. HO, G. MEIGS, J. M. BROT, S. L. HULBERT, Y. U. IDZERDA, and C. VETTIER, *Dichroic Interference Effects in Circularly-Polarized Soft-X-Ray Resonant Magnetic Scattering*, Phys. Rev. B **50**, 9599 (1994).
- [16] J. M. TONNERRE, L. SEVE, D. RAOUX, B. RODMACQ, M. DESANTIS, P. TROUSSEL, J. M. BROT, V. CHAKARIAN, C. C. KAO, E. D. JOHNSON, and C. T. CHEN, *X-Ray Resonant Magnetic Scattering At L-Edges of 3d Transition- Metals in Multilayers*, Nucl. Instr. Meth. Phys. Res. B **97**, 444 (1995).
- [17] V. CHAKARIAN, Y. U. IDZERDA, C. C. KAO, and C. T. CHEN, *Circular polarized soft X-ray resonant magnetic scattering studies of FeCo/Mn/FeCo multilayers*, J. Magn. Magn. Mater. **165**, 52 (1997).
- [18] H. A. DÜRR, E. DUDZIK, S. S. DHESI, J. B. GOEDKOOP, G. VAN-DER-LAAN, M. BELAKHOVSKY, C. MOCUTA, A. MARTY, and Y. SAMSON, *Chiral magnetic domain structures in ultrathin FePd films*, Science **284**, 2166 (1999).
- [19] E. DUDZIK, S. S. DHESI, H. A. DÜRR, S. P. COLLINS, M. D. ROPER, G. VAN DER LAAN, K. CHESNEL, M. BELAKHOVSKY, A. MARTY, and

- Y. SAMSON, *Influence of perpendicular magnetic anisotropy on closure domains studied with x-ray resonant magnetic scattering*, Phys. Rev. B **62**, 5779 (2000).
- [20] J. B. KORTRIGHT, S. K. KIM, H. OHLDAG, G. MEIGS, and A. WARWICK, *Magnetization imaging using scanning transmission X-ray microscopy*, AIP Conference Proceedings **507**, 49 (2000).
- [21] J. B. KORTRIGHT, O. HELLWIG, D. T. MARGULIES, and E. E. FULLERTON, *Resolving magnetic and chemical correlations in CoPtCr films using soft X-ray resonant scattering*, J. Magn. Magn. Mater. **240**, 325 (2002).
- [22] O. HELLWIG, D. T. MARGULIES, B. LENGFIELD, E. E. FULLERTON, and J. B. KORTRIGHT, *Role of boron on grain sizes and magnetic correlation lengths in recording media as determined by soft x-ray scattering*, Appl. Phys. Lett. **80**, 1234 (2002).
- [23] J. F. PETERS, M. A. DE VRIES, J. MIGUEL, O. TOULEMONDE, and J. B. GOEDKOOP, *Magnetic speckles with soft X-rays*, ESRF Newsletter **34**, 15 (2000).
- [24] B. HU, L. B. SORENSEN, and S. D. KEVAN *et. al.*, Synchr. Rad. News **14**, 11 (2001).
- [25] O. HELLWIG, S. MAAT, J. B. KORTRIGHT, and E. E. FULLERTON, *Magnetic reversal of perpendicularly-biased Co/Pt multilayers*, Phys. Rev. B. **65**, 1 (2002).
- [26] M. BONFIM, K. MACKAY, S. PIZZINI, M.-L. ARNOU, A. FONATINE, G. GHIRINGHELLI, S. PASCARELLI, and T. NEISIUS, *Nanosecond resolved techniques for dynamical magnetization reversal measurements*, J. Appl. Phys. **87**, 5974 (2000).
- [27] S. B. DIERKER, R. PINDAK, R. M. FLEMING, I. K. ROBINSON, and L. BERMAN, *X-ray photon correlation spectroscopy study of Brownian motion of gold colloids in glycerol*, Phys. Rev. Lett. **75**, 449 (1995).
- [28] G. GRÜBEL and D. L. ABERNATHY, *Diffraction and correlation spectroscopy with coherent X-rays*, Proceedings of the SPIE The International Society for Optical Engineering **3154**, 103 (1997).
- [29] A. C. PRICE, L. B. SORENSEN, S. D. KEVAN, J. TONER, A. PONIEWIERSKI, and R. HOLYST, *Coherent soft-X-ray dynamic light scattering from smectic-A films*, Phys. Rev. Lett. **82**, 755 (1999).
- [30] D. O. RIESE, W. L. VOS, G. H. WEGDAM, F. J. POELWIJK, D. L. ABER-

- NATHY, and G. GRÜBEL, *Photon correlation spectroscopy: X-rays versus visible light*, Physical Review E Statistical Physics, Plasmas, Fluids, and Related Interdisciplinary Topics. Feb. **61**, 1676 (2000).
- [31] A. HUBERT and R. SCHAEFER, *Magnetic Domains: The analysis of magnetic microstructures*, Springer Verlag, Berlin Heidelberg (1998).
- [32] P. WEISS, *L'Hypothèse du champ moléculaire et la propriété ferromagnétique*, J. de Phys. Rad. **6**, 661 (1907).
- [33] W. HEISENBERG, *Zur Theorie des Ferromagnetismus*, Z. Phys. **49**, 619 (1928).
- [34] Here $(\mathbf{grad} \mathbf{m})^2 = \sum_{i,j} (\partial m_i / \partial r_j)^2$.
- [35] L.D. LANDAU and E. M. LIFSHITZ, *On the theory of dispersion of magnetic permeability in ferromagnetic bodies*, Phys. Z. Sowjetunion **8**, 153 (1935).
- [36] B.A. LILLEY, *Energy and widths of domain boundaries in ferromagnetics*, Phil. Mag. **41**, 792 (1950).
- [37] W.F. BROWN JR., *Micromagnetics*, Wiley, New York (1963).
- [38] C. KITTEL, *Theory of the Structure of Ferromagnetic Domains in Films and Small Particles*, Phys. Rev. **70**, 965 (1946).
- [39] A. H. ESCHENFELDER, *Crystalline films for bubbles*, Ferromagnetic materials. A handbook on the properties of magnetically ordered substances 297-343 (1980).
- [40] C. KOOY and U. ENZ, *Experimental and theoretical study of the domain configuration in thin layers of BaFe12O19*, Philips Res. Repts. **15**, 7 (1960).
- [41] G. BOCHI, H. J. HUG, D. I. PAUL, B. STIEFEL, A. MOSER, I. PARASHIKOV, H. J. GUNTHERODT, and R. C. OHANDLEY, *Magnetic Domain-Structure in Ultrathin Films*, Phys. Rev. Lett. **75**, 1839 (1995).
- [42] M. HEHN, S. PADOVANI, K. OUNADJELA, and J. P. BUCHER, *Nanoscale magnetic domain structures in epitaxial cobalt films*, Phys. Rev. B **54**, 3428 (1996).
- [43] M. BODE, O. PIETZSCH, A. KUBETZKA, and R. WIESENDANGER, *Imaging magnetic nanostructures by spin-polarized scanning tunneling spectroscopy*, Journ. of Electron Spectroscopy and Related Phenomena **116**, 1055 (2001).
- [44] M. BODE, O. PIETZSCH, A. KUBETZKA, R. RAVLIC, and R. WIESENDANGER, *Imaging magnetic domains with sub-nanometer resolution using spin-*

- polarized STM*, Intermag Europe (2002).
- [45] R. ALLENSPACH, *Spin polarized scanning electron microscopy*, IBM Journal of Research and Development. July **44**, 553 (2000).
- [46] C. M. SCHNEIDER, R. FROMTER, C. ZIETHEN, W. SWIECH, N. B. BROOKES, G. SCHONHENSE, and J. KIRSCHNER, *Magnetic domain imaging with a photoemission microscope*, Magnetic Ultrathin Films, Multilayers and Surfaces 381–92 (1997).
- [47] J. N. CHAPMAN and M. R. SCHEINFELD, *Transmission electron microscopies of magnetic microstructures*, J. Magn. Magn. Mater. **200**, 729 (1999).
- [48] P. R. AITCHISON, J. N. CHAPMAN, V. GEHANNO, I. S. WEIR, M. R. SCHEINFELD, S. MCVITIE, and A. MARTY, *High resolution measurement and modelling of magnetic domain structures in epitaxial FePd(001) L1₀ films with perpendicular magnetisation*, J. Magn. Magn. Mater. **223**, 138 (2001).
- [49] J. OREHOTSKY and K. SCHRÖDER, *Magnetic properties of amorphous Fe_xGd_y alloy thin films*, J. Appl. Phys. **453**, 2413 (1972).
- [50] P. HANSEN, C. CLAUSEN, G. MUCH, M. ROSENKRANZ, and K. WITTER, *Magnetic and Magneto-Optical Properties of Rare-Earth Transition-Metal Alloys Containing Gd, Tb, Fe, Co*, J. Appl. Phys. **66**, 756 (1989).
- [51] Y. MIMURA, N. IMAMURA, and T. KOBAYASHI, *Preparation and some magnetic properties of amorphous Gd_xFe_{1-x} alloy thin films*, J. Appl. Phys. **47**, 368 (1976).
- [52] R. C. TAYLOR, *Magnetic properties of amorphous Gd-Fe films prepared by evaporation*, J. Appl. Phys. **47**, 1164 (1976).
- [53] A. G. DIRKS and H. J. LEAMY, *Microstructure and magnetism in amorphous rare earth-transition metal thin films*, J. Appl. Phys. **49**, 1735 (1978).
- [54] F. HELLMAN, P. W. ROONEY, and E. M. GYORGY, *Macroscopic magnetic anisotropy and the vapor deposition process in amorphous RE-TM alloys*, J. Appl. Phys. **73**, 5793 (1993).
- [55] D. MERGEL, H. HEITMANN, and P. HANSEN, *Pseudocrystalline Model of the Magnetic-Anisotropy in Amorphous Rare-Earth Transition-Metal Thin-Films*, Phys. Rev. B **47**, 882 (1993).
- [56] M. LABRUNE and J. MILTAT, *Strong stripes as a paradigm of quasi-topological hysteresis*, J. Appl. Phys. **75**, 2156 (1994).

- [57] J.A. CAPE and G.W. LEHMAN, *J. Appl. Phys.* **42**, 5732 (1971).
- [58] W. F. DRUYVESTeyN, J. W. F. DORLEIJN, and P. J. RIJNIESE, *Analysis of a method for measuring the magnetocrystalline anisotropy of bubble materials*, *J. Appl. Phys.* **44**, 2397 (1973).
- [59] A. HUBERT, *The calculation of periodic domains in uniaxial layers by a micromagnetic domain model*, in *IEEE Trans. on Magnetics*, volume MAG-21, 1604–1606 (1985).
- [60] A. MARTY, Y. SAMSON, B. GILLES, M. BELAKHOVSKY, E. DUDZIK, H. DÜRR, S. S. DHESI, G. VAN DER LAAN, and J. B. GOEDKOOP, *Weak-stripe magnetic domain evolution with an in-plane field in epitaxial FePd thin films: Model versus experimental results*, *J. Appl. Phys.* **87**, 5472 (2000).
- [61] J. KACZER, M. ZELENY, and P. SUDA, *Czech. J. Phys. B* **13**, 579 (1963).
- [62] A. L. SUKSTANSKII and K. I. PRIMAK, *Domain structure in an ultrathin ferromagnetic film*, *J. Magn. Magn. Mater.* **169**, 31 (1997).
- [63] [Http://functions.wolfram.com/EllipticFunctions/JacobiSN/](http://functions.wolfram.com/EllipticFunctions/JacobiSN/) (2002).
- [64] A. HUBERT and W. RAVE, *How well-defined are closure domains?*, *J. Magn. Magn. Mater.* **197**, 325 (1999).
- [65] M.W. MULLER, *Distribution of the magnetization in a ferromagnet*, *Phys. Rev.* **122**, 1485 (1961).
- [66] J.D. JACKSON, *Classical Electrodynamics*, Wiley, New York, 3rd ed. edition (1998).
- [67] L.D. LANDAU, E. M. LIFSHITZ, and L. P. PITAEVSKII, *Electrodynamics of Continuous Media*, Pergamon Press, New York etc., 2 edition (1984).
- [68] D. Y. SMITH, *Dispersion relations and sum rules for magnetorefectivity*, *J. Opt. Soc. Am.* **66**, 547 (1976).
- [69] D. Y. SMITH, *Superconvergence and sum rules for the optical constants: natural and magneto-optical activity*, *Phys. Rev. B* **13**, 5303 (1976).
- [70] D. Y. SMITH, *Theoretical aspects and new developments in magneto-optics*, in J-T DEVREESE, editor, *Nato Advanced Institute on Theoretical Aspects and New Developments in Magneto-Optics*, Plenum Press, Antwerpen (1979).
- [71] M. BLUME, *Magnetic effects in anomalous dispersion*, in G. MATERLIK, C.J. SPARKS, and K. FISCHER, editors, *Resonant anomalous X-ray scattering The-*

- ory and Applications, 495, Elsevier Science B.V., Amsterdam (1994).
- [72] R. KRONIG and H. A. KRAMERS, *Absorption and dispersion in X-ray Spectra*, Z. Phys. **48**, 174 (1928).
- [73] H.M. NUSSENZVEIG, *Causality and dispersion relations*, volume 95 of *Mathematics in science and engineering*, Academic Press, New York (1972).
- [74] J. B. GOEDKOOP, *X-ray dichroism of rare earth materials*, Ph.D. thesis, Katholieke Universiteit Nijmegen (1989).
- [75] J. STÖHR and R. NAKAJIMA, *X-ray magnetic circular dichroism spectroscopy of transition metal multilayers*, Journal De Physique Iv **7**, 47 (1997).
- [76] L. A. FEIGIN, D.I. SVERGUN, and G. W. TAYLOR, *Structure analysis by small-angle x-ray and neutron scattering*, Plenum, New York (1987).
- [77] J. P. HILL and D. F. MCMORROW, *X-ray resonant exchange scattering: polarization dependence and correlation functions*, Acta Cryst. A **A52**, 236 (1996).
- [78] L. SEVE, J. M. TONNERRE, and D. RAOUX, *Determination of the anomalous scattering factors in the soft-X-ray range using diffraction from a multilayer*, J. Appl. Cryst. **5**, 700 (1998).
- [79] M. SACCHI, C. F. HAGUE, L. PASQUALI, A. MIRONE, J. M. MARIOT, P. ISBERG, E. M. GULLIKSON, and J. H. UNDERWOOD, *Optical constants of ferromagnetic iron via 2p resonant magnetic scattering*, Phys. Rev. Lett. **81**, 1521 (1998).
- [80] R. L. BLAKE, J. C. DAVIS, D. E. GRAESSLE, T. H. BURBINE, and E. M. GULLIKSON, *Optical constants and scattering factors from reflectivity measurements: 50 eV to 5 keV*, in G. MATERLIK, C.J. SPARKS, and K. FISCHER, editors, *Resonant Anomalous X-ray Scattering, Theory and Applications*, 79–90, Elsevier, New-York (1994).
- [81] J. B. KORTRIGHT and M. RICE, *Soft X-ray optical rotation as element-specific magneto-optical probe*, Magnetic Ultrathin Films, Multilayers and Surfaces. Symposium. 461–6 (1995).
- [82] J. B. KORTRIGHT and KIM SANG KOOG, *Resonant magneto-optical properties of Fe near its 2p levels: Measurement and applications*, Phys. Rev. B **62**, 12216 (2000).
- [83] H. C. MERTINS, O. ZAHARKO, A. GAUPP, F. SCHAFERS, D. ABRAMSOHN, and H. GRIMMER, *Soft X-ray magneto-optical constants at the Fe 2p*

- edge determined by Bragg scattering and Faraday effect*, *J. Magn. Magn. Mater.* **240**, 451 (2002).
- [84] C. T. CHEN, Y. U. IDZERDA, H. J. LIN, N. V. SMITH, G. MEIGS, E. CHABAN, G. H. HO, E. PELLEGRIN, and F. SETTE, *Experimental confirmation of the X-ray magnetic circular dichroism sum rules for iron and cobalt*, *Phys. Rev. Lett.* **75**, 152 (1995).
- [85] F. YUBERO, S. TURCHINI, F. C. VICENTIN, J. VOGEL, and M. SACCHI, *Magnetic Circular-Dichroism in Transmission Mode at the Ni 2p Edges*, *Sol. St. Comm.* **93**, 25 (1995).
- [86] F. C. VICENTIN, S. TURCHINI, F. YUBERO, J. VOGEL, and M. SACCHI, *Absorption cross sections at the $M_{4,5}$ edges of rare earths: A soft X-ray transmission experiment*, *J. Electron Spectrosc. Relat. Phenom.* **74**, 187 (1995).
- [87] V. CHAKARIAN, Y. U. IDZERDA, and C. T. CHEN, *Absolute helicity-dependent photoabsorption cross sections of Fe thin films and quantitative evaluation of magnetic-moment determination*, *Phys. Rev. B* **57**, 5312 (1998).
- [88] [Http://www.esrf.fr/exp_facilities/ID8/ID8.html](http://www.esrf.fr/exp_facilities/ID8/ID8.html).
- [89] B. L. HENKE, E. M. GULLIKSON, and J. C. DAVIS, *X-ray interactions: photoabsorption, scattering, transmission, and reflection at $E=50-30000$ eV, $Z=1-92$* , *Atomic Data and Nuclear Data Tables.* **54**, 181 (1993).
- [90] J. B. GOEDKOOP, J. C. FUGGLE, B. T. THOLE, G. VAN-DER LAAN, and G. A. SAWATZKY, *Magnetic X-ray dichroism of rare-earth materials*, *J. Appl. Phys.* **64**, 5595 (1988).
- [91] M. M. SCHWICKERT, G. Y. GUO, M. A. TOMAZ, W. L. O'BRIEN, and G. R. HARP, *X-ray magnetic linear dichroism in absorption at the L edge of metallic Co, Fe, Cr, and V*, *Phys. Rev. B* **58**, R4289 (1998).
- [92] S. S. DHESI, G. VAN DER LAAN, and E. DUDZIK, *Determining element-specific magnetocrystalline anisotropies using x-ray magnetic linear dichroism*, *Appl. Phys. Lett.* **80**, 1613 (2002).
- [93] M. J. FREISER, *A survey of Magneto optic effects*, *IEEE Trans. Magn.* **4**, 152 (1968).
- [94] E. D. ISAACS, D. B. MCWHAN, C. PETERS, G. E. ICE, D. P. SIDDONS, J. B. HASTINGS, C. VETTER, and O. VOGT, *X-ray resonance exchange scattering in UAs*, *Phys. Rev. Lett.* **62**, 1671 (1989).

- [95] C. C. TANG, W. G. STIRLING, G. H. LANDER, D. GIBBS, W. HERZOG, P. CARRA, B. T. THOLE, K. MATTENBERGER, and O. VOGT, *Resonant magnetic X-ray scattering in a series of uranium compounds*, Phys. Rev. B **46**, 5287 (1992).
- [96] E. E. FULLERTON, I. K. SCHULLER, H. VANDERSTRAETEN, and Y. BRUYNSERAEDE, *Structural refinement of superlattices from X-ray diffraction*, Phys. Rev. B **45**, 9292 (1992).
- [97] J. BRUNNER-POPELA and O. GLATTER, *Small-Angle Scattering of Interacting Particles. I Basic Principles of a Global Evaluation Technique.*, J. Appl. Cryst **30**, 431 (1997).
- [98] J. MIGUEL, J. F. PETERS, M. A. DE VRIES, O. TOULEMONDE, and J. B. GOEDKOOP, *in preparation* (2003).
- [99] KIM SANG KOOG, J. B. KORTRIGHT, and SHIN SUNG CHUL, *Vector magnetization imaging in ferromagnetic thin films using soft X-rays*, Appl. Phys. Lett. **78**, 2742 (2001).
- [100] J. F. PETERS, J. MIGUEL, M. A. DE VRIES, O. TOULEMONDE, and J. B. GOEDKOOP, *in preparation* (2003).

SUMMARY

This thesis describes experiments in which the internal 3-D magnetic *vector* structure of magnetic domains with a typical width of 50 to 100 nm is reconstructed from resonant soft x-ray scattering data taken in a transmission geometry. The specific systems that we have studied are 40 nm GdFe₅ and GdFe₉ magnetic thin films that exhibit so-called stripe domains: a quasi-periodic 1-dimensional lattice of alternating up- down magnetized domains. For photon energies around the Gd M_{4,5} (3d → 4f) and Fe L_{2,3} (2p → 3d) resonances large magneto-optical effects occur: the absorption and dispersion of an electromagnetic wave propagating in a magnetic medium depends on the direction of the magnetization vector \mathbf{m} and the polarization of the wave.

In the first experimental part of this thesis we study the x-ray magneto-optic effect itself. We present measurements of the x-ray absorption (XAS), magnetic circular dichroism (XMCD) and magnetic linear dichroism (XMLD) around the Gd M_{4,5} and Fe L_{2,3} resonances. The imaginary part of the resonant scattering length is directly obtained from these measurements while the real part follows from the Kramers-Kronig transformation of the absorption and dichroism data. The energy dependent resonant circular magnetic scattering amplitude obtained from this analysis is found to be in remarkable agreement with data for the total scattered intensity from a stripe domain lattice.

We find that at the Gd M_{4,5} edge both the circular $F^{(1)}$ and the linear magnetic resonant scattering amplitude $F^{(2)}$ are huge, while on the Fe L_{2,3} edge only a $F^{(1)}$ contribution could be detected. We show we that we can separate the structure of the three cartesian components of \mathbf{m} in a single experiment, by varying the polarization of the incident light. Comparing the diffraction data with a micromagnetic model for the complex vortex-like internal structure for the stripe

domains, we can recognize scattering contributions from bulk domains, domain walls and surface closure domains.

Having established this interpretation of the scattering data we study the magnetic structure of the thin films under the influence of a magnetic field applied in the film plane. The evolution of the magnetic structure over the magnetization curve shows an unexpected and rich behavior, involving a disorder-order transition at the domain nucleation field, a strong dependence of the stripe period on field, the creation and growth of a Bloch wall structure and the appearance of closure domains. Between remanence and the coercive field, the Bloch wall structure is found to evolve in a Néel type wall structure which at the coercive field jumps back into a Bloch wall structure with the opposite field direction. The great detail with which the stripe evolution could be studied shows that x-ray resonant magnetic scattering is a powerful probe for the study of the spatial structure in ordered nanomagnetic systems.

SAMENVATTING

In dit proefschrift worden experimenten beschreven waarin de interne 3-D magnetische *vectorstructuur* van magnetische domeinen met een typische breedte van 50 tot 100 nm wordt gereconstrueerd uit resonante zachte Röntgenverstrooiingsdata gemeten in een transmissie geometrie. Specifiek hebben we 40 nm dikke GdFe_5 en GdFe_9 magnetische dunne lagen bestudeerd waarin zogenaamde streepdomeinen voorkomen: een quasi periodiek 1-dimensionaal rooster van afwisselend op- neer gemagnetiseerde domeinen. Als de fotonenergie in de buurt van de Gd $M_{4,5}$ ($3d \rightarrow 4f$) en de Fe $L_{2,3}$ ($2p \rightarrow 3d$) resonanties ligt treden er grote magneto-optische effecten op: de absorptie en dispersie van een zich in een magnetisch materiaal voortplantende electromagnetische golf worden sterk afhankelijk van de richting van de magnetisatievector \mathbf{m} en de polarisatie van het licht.

In het eerste experimentele deel van dit proefschrift wordt het Röntgen magneto-optische effect zelf bestudeerd. We presenteren metingen van de Röntgenabsorptie, het magnetisch circulair dichroïsme en het magnetisch lineair dichroïsme rond de Gd $M_{4,5}$ en Fe $L_{2,3}$ resonanties. Het imaginaire deel van de resonante verstrooiingsamplitude volgt direct uit deze metingen terwijl het reële deel gevonden wordt door Kramers-Kronig transformatie van de absorptie en dichroïsme data. De overeenkomst tussen de met deze analyse gevonden energieafhankelijke circulair magnetische verstrooiingsamplitude en de totaal verstrooide intensiteit gemeten voor verstrooiing aan een streepdomein rooster is opmerkelijk.

We vinden dat voor de Gd $M_{4,5}$ absorptie lijn zowel de circulaire $F^{(1)}$ als de lineaire $F^{(2)}$ resonante verstrooiingsamplitudes groot zijn, terwijl voor de Fe $L_{2,3}$ lijn alleen een $F^{(1)}$ bijdrage gevonden wordt. We laten zien dat in één experi-

ment de structuur van de drie cartesische componenten van \mathbf{m} gescheiden kan worden, gebruikmakend van de polarisatieafhankelijkheid van de verstrooiing. Door de diffractiedata te vergelijken met een micromagnetisch model van de complexe vortexachtige interne structuur van de streepdomeinen kunnen we de verstrooiingsbijdragen onderscheiden van bulk domeinen, domeinwanden en oppervlakte fluxsluitings domeinen.

Gebruikmakend van deze interpretatie bestuderen we vervolgens de magnetische structuur van de dunne lagen onder de invloed van een magnetisch veld aangelegd in het vlak van de film. De ontwikkeling van de magnetische structuur over de magnetisatie curve is onverwacht rijk en complex, met een wanordeorde overgang bij het domein nucleatieveld, een periode die sterk veldafhankelijk is, het ontstaan en de groei van een Blochwandstructuur en het verschijnen van oppervlakte sluitingsdomeinen. Tussen remanentie en het coercieve veld gaat de Blochwandstructuur over in een meer Néel achtige domeinwandstructuur, bij het coercieve veld springt deze laatste terug in een Blochwandstructuur van tegengestelde magnetisatierichting. Het grote detail waarin we de domeinontwikkeling kunnen volgen laat zien dat Röntgen resonante magnetische verstrooiing een krachtige methode is om de spatiele structuur van geordende nanomagnetische systemen te bestuderen.

DANKWOORD

Experimenteel onderzoek gaat niet anders dan samen met anderen, dat is voor mij essentieel. Het schrijven van een proefschrift, op zich een bij tijd en wijle zeer eenzame bezigheid, is de moeite waard door het leven en werk daaromheen, met vrienden, familie en collega's. Mijn dank gaat dan ook uit naar iedereen die op de één of andere wijze bij de totstandkoming van dit proefschrift betrokken is geweest, of hier belangstelling voor getoond heeft.

Met Jeroen Goedkoop en Friso van der Veen heb ik twee excellente begeleiders getroffen, met een geheel eigen stijl en persoonlijkheid en een totaal van elkaar verschillende werkwijze.

Jeroen: tovenaars van de bundellijn, meester van de zachte Röntgen, passie voor onderzoek, experimentator én romanticus in hart en nieren, brouwer van doordenderende zinnen en weidse vergezichten (..), het is af over uit, bedankt.

Friso: altijd gedreven en intens, of het nu om wetenschap of muziek gaat, exact, precies, veeleisend, altijd daar op het juiste moment.

The other synchrotron rats, dreamteam I: Michel and Jeroen, dreamteam II: Mark, Olivier and last but not least Jorge, many nightshifts together can be a nerve wrecking, but in the end satisfying experience, I am grateful to you all.

Met Huib heb ik de MBE 'ontdekt' en aan de gang gehouden, met ondersteuning van Piet en Johan. Met de laatste en Otto heb ik in Grenoble 'kleine Bertha I' opgebouwd, voor mij was die week een absoluut hoogtepunt in de afgelopen jaren.

Het dagelijkse kopje-koffie-na-de-lunch en het wekelijkse biertje in Kriterion zijn belangrijke rituelen en dragen bij tot de goede sfeer op het lab, daarvoor bedankt Dennis, Leonid, Mark, Ekkes, Tegus, Yuri, Liang Zhang, Thang, Duong, Xiao, Li, Frank, Manuel, Mark, Nacio, Maciek, Tom, Tom, Tracy, Sarah, Jaime, Femius, Lydia, Boris, Pedro, Rob, Ronald, Gerard, Jacques, Bas, Erik-Paul en Heidi. Zonder techniek geen resultaat, bedankt, Harrie, Joost, Erik, Ron, Diederik, Floris, Wim, Jeffrey, Hans, Bert en Eddy, Theo, Edwin, Ben, Alof, Johan, Bert en Willem. Hugo en Ton staan altijd klaar, van boogsmeltwerk tot posterprinten. Ineke, Roos, Mariet, Rita en Dick bedankt voor hulp bij het papierwerk en andere rompslomp. I would like to thank the ESRF staff, the beamlines were always up and running thanks to Nick, Sarnjeet, Kenneth, and Carsten.

Frans en Mieke, jullie hebben mij altijd met veel liefde gesteund in wat ik doe. Door jullie heb ik zorgeloos kunnen studeren, misschien wel daarom dat het een beetje doorgeschoten is. Barbara en Lars, ik houd van jullie.

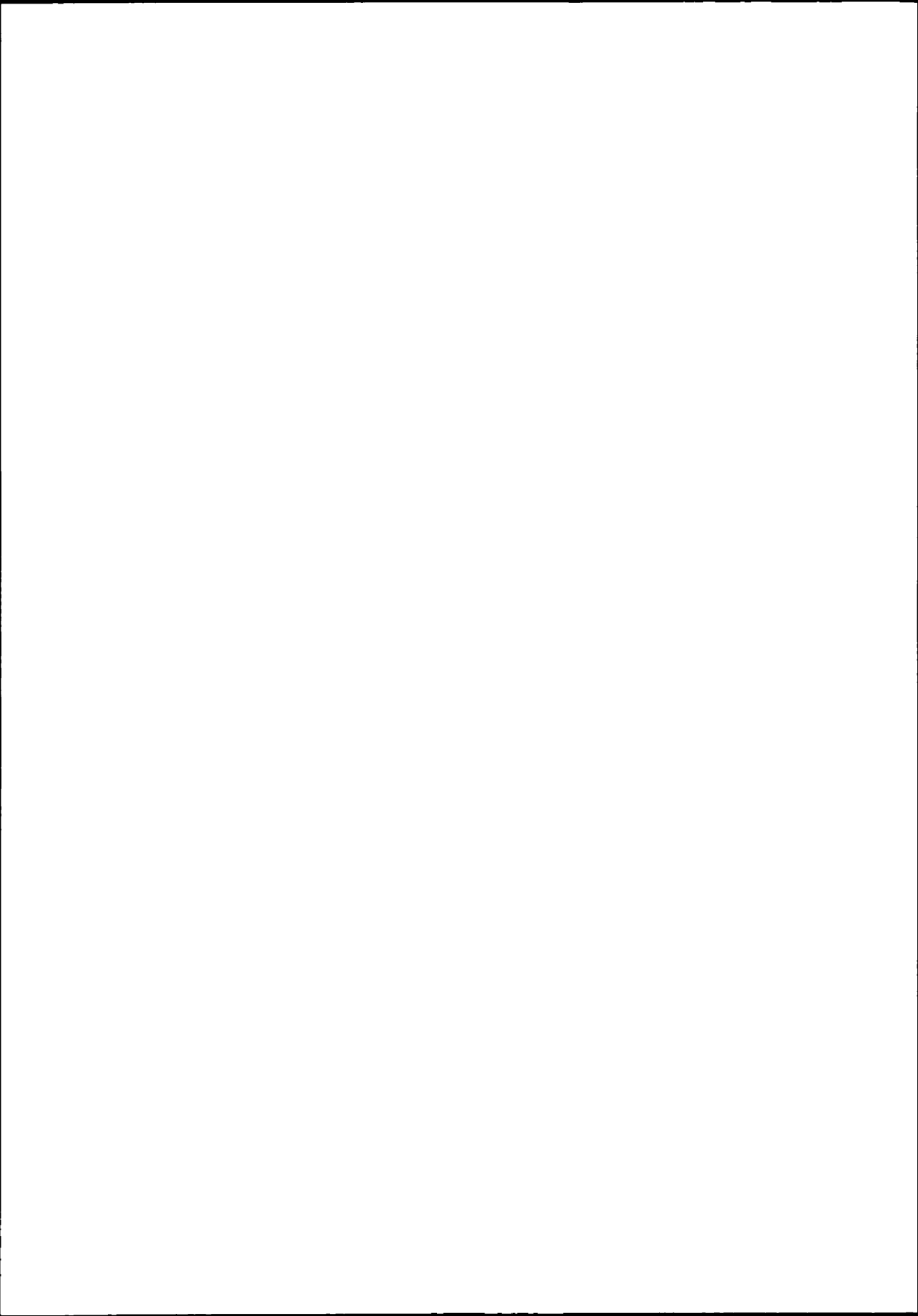
Marjan, tegelijkertijd een proefschrift schrijven, 'mag dat?'. We hebben de ups en downs van het promovendusschap met elkaar beleefd en zijn daarbij langzaam aan steeds dichterbij elkaar gekomen. Er breken andere tijden aan, ik hoop dat jij net zo benieuwd naar onze toekomst als ik.

CURRICULUM VITAE

Op 24 Oktober 1973 ben ik te Amsterdam geboren. Op mijn vijfde verhuizen we naar Grootebroek alwaar ik in 1992 mijn schoolopleiding afsluit met het behalen van het Atheneum diploma aan het Marcuscollege.

Dat jaar begint ook mijn studie natuurkunde aan de universiteit van Amsterdam. In 1997 behaal ik het doctoraalexamen in de experimentele natuurkunde na een afstudeerstage op het Amolf in de groep van Prof. dr. Friso van der Veen. Hier hield ik mij onder andere bezig met het uitwerken van middelbare energie ionen verstrooiings metingen aan het met Gallium bedekte diamant(111) oppervlak en het mede-ontwikkelen van een vacuümopstelling voor onderzoek naar de vaste stof-vloeistof overgang met harde Röntgenstraling.

Na mijn studie begin ik aan mijn promotieonderzoek, opnieuw aan de universiteit van Amsterdam. Ik zal mij gaan bezighouden met het van groeien en onderzoeken van magnetische (multi-)lagen met behulp moleculaire bundelepitaxie. Het onderzoek vindt plaats in de groep van dr. Ekkes Brück en mijn promotor is Prof. Dr. Friso van der Veen. Na een jaar komt dr. Jeroen Goedkoop van de Europese Synchrotron in Grenoble (ESRF) naar Amsterdam. Er ontstaat een samenwerking waarbij de nadruk van mijn onderzoek verschuift naar de ontwikkeling van zachte Röntgen verstrooiingsmethoden voor het onderzoek van magnetische dunne lagen. Met dr. Jeroen Goedkoop en de andere leden van onze groep doen we vele experimenten op de bundellijnen ID12B en ID08 van de ESRF. De neerslag van dit werk is te vinden in dit proefschrift.



ISBN 905776105X